Building Blocks for Majorana Zero Modes – New Insight to Induced Topological Superconductors and Dirac Semimetal Josephson Junctions

（マヨラナゼロモードの探索：誘起されたトポロジカル超伝導とディラック半金属ジョセフソン接合）

Jan Erik Reinhard Wichmann

Institut for Materials Research, Tohoku University

August 17, 2022

Contents

1 Introduction

Ever since their discovery topological materials have caught researchers interest due to their unique properties reaching from the integer quantum Hall effect to spin filtered edge transport and beyond [1–3]. The high interest in topological systems is not only due to their interesting physical properties, but also because of their applications in engineering settings. For example the integer quantum Hall effect can be used to create a high precision reference resistance which can be used to calibrate highly accurate measurement devices. Another, so far only potential, application is the use of topological systems to create robust qubits and quantum computers [4–6]. Such topological qubits could be constructed from Majorana zero modes, which are predicted to arise in numerous topological systems. In the present work we will have a look at two systems proposed to host Majorana zero modes, the topological insulator (TI) – superconductor (SC) heterostructure and a Dirac semimetal (DSM) Josephson junction and will gain new insight about these systems.

1.1 Majorana Zero Modes in Topological Materials

Majorana zero modes have been an active topic of research for quite a while in both the theoretical and the experimental world. Much of this interest stems from the fact that Majorana zero modes would allow for the creation of robust topological quantum computers. These topological quantum computers have the advantage of being rather robust against external perturbations, which is a major pain point for contemporary qubits based on other designs such as ion traps. Another point of interest about Majorana zero modes are their physical properties such as being their own anti-particle. So far no elemental Majorana particles have been found (though the neutrino is still a viable candidate), but their realization as a quasi particle in solid state physics would be highly interesting.
In solid state systems Majorana zero modes can manifest themselves in various situations. One system are topological superconductors. In spinless topological superconducting one dimensional wires MZMs would manifest themselves at the ends of the wire [7, 8]. The major difficulty with topological superconductors is that, to the best of our knowledge, no such

material has yet been found. A very promising and long discussed approach has been to artificially construct topological superconductors by inducing superconductivity into regular topological matter via the superconducting proximity effect [2, 9]. For example it has been proposed that the interface of a three dimensional strong topological insulator can be turned into a two dimensional induced topological superconductor via superconducting proximity effect from a conventional s-wave superconductor placed on top of the topological insulator [9]. This is due to the Cooper pairs from the s-wave superconductor tunneling into the surface states of the topological insulator. There they will induce a superconducting gap in the surface states of the topological insulator, which in turn can be described by a $p_x + ip_y$ superconductor. Majorana zero modes can then emerge when the system is brought into contact with a ferromagnet. The ferromagnet, too, will induce a gap in the surface states of the topological insulator, albeit topologically distinct from the superconductivity induced gap. At the one dimensional boundary of the regions, one gapped via superconductor, the other via ferromagnet, Majorana zero modes will emerge, see Figure 1.1a. A more sophisticated version with the same underlying mechanism would instead be a system in an external magnetic field where the Majorana zero modes would be located at the ends of the vortices in the regular s-wave superconductor, see Figure 1.1b. The advantage of the latter setup is that the Majorana zero modes can be moved freely across the two dimensional topological superconductor by simply moving the vortices of the superconductor. This means that multiple Majorana zero modes can be moved around each other and exchange position without ever getting close to each other. Obviously, such movement is not possible with Majorana zero modes being located on a one dimensional line, so there other tricks are required, such as constructing junctions.
However, despite the relative ease with with Majorana zero modes can be shifted around, a major challenge remains their localization at the interface between topological insulator and superconductor. This makes them inaccessible for direct measurements from either surface via surface sensitive methods such as angle-resolved photoemission spectroscopy (ARPES) or scanning tunneling microscopy (STM). Bulk sensitive measurements such as neutron scattering on the other hand will be sensitive to all bulk states, such that the two dimensional induced topological insulator will hardly be covered and drowned by the bulk signals of both, the s-wave superconductor and the topological insulator.
Despite these obstacles experimentalists have succeeded to use ARPES to observe surface states of topological insulators through thin films of both normal metal (NM) and superconductor, opening new pathways to the experimental investigation of induced topological superconductors [10, 11]. The observation of the surface states of the topological insulator through the adjacent material was attributed to the states extending from the surface into the bulk of the adjacent material.

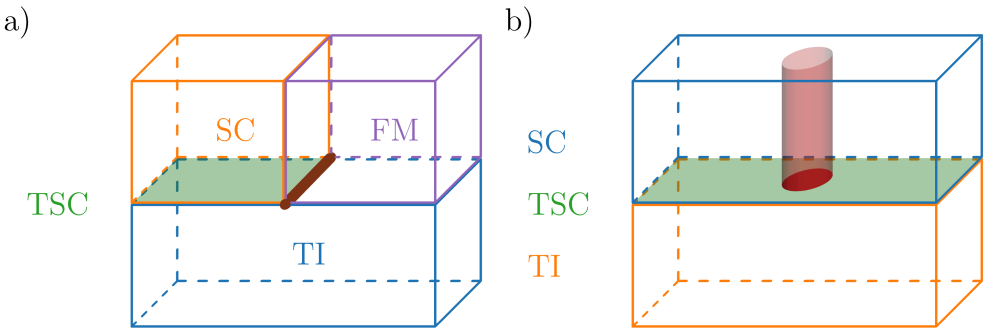

Figure 1.1: (a) Three dimensional topological insulator (blue), partially covered by a s-wave superconductor (orange) and a ferromagnet (purple). At the interface between topological insulator and superconductor a two dimensional topological superconductor is formed (green). Majorana zero modes form at the one dimensional edge where superconductor, ferromagnet and topological insulator coincide (brown). (b) Majorana zero modes can also form at the bottom of vortices in a topological insulator–superconductor heterostructure (red dot at the bottom of the tube).

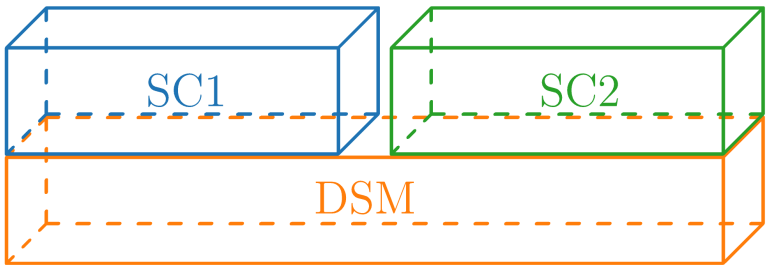

Figure 1.2: Dirac semimetal Josephson junction consisting of Dirac semimetal (DSM, orange), and two superconductors (SC1, blue; SC2, green).

Another interesting proposal to create Majorana zero modes is by using a Josephson junction over a Dirac semimetal, see Figure 1.2 [12, 13]. This system is notably different from the previous one as it uses a gapless topological material, a Dirac semimetal. Being a gapless topological state of matter, Dirac semimetals have attracted lots of attention in both theory and experiment [14–24]. Similar to topological insulators Dirac semimetals also have very interesting and highly localized surface states, which again acquire novel properties when brought into contact with regular superconductors. Here however the required domain boundary is not created by superconductor and ferromagnet, but by two superconductors with differing superconducting phases instead. Hence a Josephson junction is created and a fractional Josephson current is indeed a proposed method to indicate the presence of Majorana zero modes [12, 13].
A major challenge regarding Majorana zero modes remains their conclusive experimental observation. Due to their very nature as quasiparticles direct experimental observation is impossible and signatures hinting at the existence of Majorana zero modes must instead be considered.

Over the years, various proposals of such signatures have been made, but many have turned out to be inconclusive, as other explanations for the corresponding observations have been found. A good example for such an experimental signature of Majorana zero modes is the zero-bias conductance peak, which has since been found out to also occur in topologically trivial systems without Majorana zero modes, though the absence of a zero-bias conductance peak would still indicate an absence of Majorana zero modes [25–27]. Another prominent, albeit inconclusive, signature of Majorana zero modes would be a fractional 4π periodic Josephson current [7, 28]. We will comment more on the usefulness and limitations of the observation of a fractional Josephson current as a signature of Majorana zero modes when introducing the basics of Josephson junctions in section 1.5. The last noteworthy experimental signature of Majorana zero modes we want to mention is the half integer thermal conductance, which is still considered to be a conclusive signature of Majorana zero modes and to which we are not aware of other possible explanations for its observation [29–31].
In this work we will have a look at both, a topological insulator–superconductor heterostructure and Dirac semimetal Josephson junctions as platforms for potentially hosting Majorana zero modes, though we will not look for conclusive signatures of such zero modes.

1.2 Physics of Superconducting Systems

Being a crucial phenomenon for our entire work, we will now have a brief look at the physics of superconducting systems, with an emphasis on BCS theory, which we will use later on. After superconductivity was first discovered experimentally by Onnes in 1911, it took until 1957 until a comprehensive microscopic theory of superconductivity was found, the so called BCS theory, named after its authors Bardeen, Cooper and Schrieffer [32, 33]. Since then more exotic forms of superconductivity such as the unconventional superconductivity of cuprates have been found. We shall however limit ourselves to conventional superconductivity described by BCS theory, as such superconductors are commonly used when pursuing Majorana zero modes via topological insulator-superconductor junctions or the Josephson effect in Dirac semimetal junctions.
From a phenomenological point of view, conventional superconductors are characterized by their perfect diamagnetism, the Meissner-Ochsenfeld effect, their perfect electrical conductivity, their second-order phase transition at a critical temperature T_C and their energy gap within their bandstructure. Other interesting phenomenons occur when superconductors are brought into contact with other materials such as normal metals or insulators. Such phenomena include Andreev reflection and the superconducting proximity effect, which are intimately

related and occur at the interface between a normal metal and a superconductor. Another interesting phenomenon are Josephson currents, which are observed between two superconductors separated a small distance by other materials such as insulators. All these phenomena will be described after this introduction to BCS theory.

BCS theory gives a microscopic description of conventional superconductivity from which all its interesting properties can be derived. We shall now give a brief explanation of the important details of that theory. This is not so much intended as a full introduction to BCS theory, but rather to clarify terminology and notation used. For a more thorough introduction any of a number of very good text books should be consulted [34–37].

The prototype model for a superconducting Hamiltonian is usually given as

$$H = \sum_{\mathbf{k}\sigma} \xi_{\mathbf{k}} c^\dagger_{\mathbf{k}\sigma} c_{\mathbf{k}\sigma} + \sum_{\mathbf{k}\mathbf{k}'} V_{\mathbf{k}\mathbf{k}'} c^\dagger_{\mathbf{k}\uparrow} c^\dagger_{-\mathbf{k}\downarrow} c_{-\mathbf{k}'\downarrow} c_{\mathbf{k}'\uparrow}. \tag{1.1}$$

After a mean-field treatment we find the Hamiltonian of the form

$$H_{\mathrm{BCS}} = \sum_{\mathbf{k}\sigma} \xi_{\mathbf{k}} c^\dagger_{\mathbf{k}\sigma} c_{\mathbf{k}\sigma} - \sum_{\mathbf{k}} \Delta^*_{\mathbf{k}} c_{-\mathbf{k}\downarrow} c_{\mathbf{k}\uparrow} - \sum_{\mathbf{k}} \Delta_{\mathbf{k}} c^\dagger_{\mathbf{k}\uparrow} c^\dagger_{-\mathbf{k}\downarrow} \tag{1.2}$$

with the mean field parameter

$$\Delta_{\mathbf{k}} = -\sum_{\mathbf{k}'} V_{\mathbf{k}\mathbf{k}'} \langle c_{-\mathbf{k}\downarrow} c_{\mathbf{k}'\uparrow} \rangle. \tag{1.3}$$

As a quick reminder, let us note that the expectation value $\langle c_{-\mathbf{k}\downarrow} c_{\mathbf{k}'\uparrow} \rangle$ is non-zero, because it is not defined with respect to the vacuum, but to the BCS ground state

$$|\psi_{\mathrm{BCS}}\rangle = \prod_{\mathbf{k}} (u_{\mathbf{k}} + v_{\mathbf{k}} c^\dagger_{\mathbf{k}\uparrow} c^\dagger_{-\mathbf{k}\downarrow} |0\rangle, \tag{1.4}$$

where $|0\rangle$ denotes the vacuum state and the complex numbers $u_{\mathbf{k}}$ and $v_{\mathbf{k}}$ are so-called coherence factors. Normalization of the BCS ground state requires that

$$1 = \langle \psi_{\mathrm{BCS}} | \psi_{\mathrm{BCS}} \rangle = \prod_{\mathbf{k}} \left(|u_{\mathbf{k}}|^2 + |v_{\mathbf{k}}|^2 \right). \tag{1.5}$$

Now we are all set and we could go ahead and calculate the mean-field parameters $\Delta_{\mathbf{k}}$ self-consistently. However, having a close look at the mean-field Hamiltonian (1.2) we can see that the Hamiltonian is quadratic in creation/annihilation operators, but it is not diagonal. Indeed, it contains terms of the form cc and $c^\dagger c^\dagger$, which do not preserve electron number. This

matches very well with the definition of the BCS ground state $|\psi_{\mathrm{BCS}}\rangle$, which also does not have a fixed number of electrons. The Hamiltonian can be brought into a diagonal form by performing a Bogoliubov-Valatin transformation. For this transformation, we introduce new fermion operators γ, $\gamma^\dagger$ as linear combinations of our regular electron operators c, $c^\dagger$ as follows

$$\begin{pmatrix} \gamma_{\mathbf{k}\uparrow} \\ \gamma^\dagger_{-\mathbf{k}\downarrow} \end{pmatrix} = \begin{pmatrix} u_{\mathbf{k}} & -v_{\mathbf{k}} \\ v^*_{\mathbf{k}} & u^*_{\mathbf{k}} \end{pmatrix} \begin{pmatrix} c_{\mathbf{k}\uparrow} \\ c^\dagger_{-\mathbf{k}\downarrow} \end{pmatrix}. \tag{1.6}$$

In order to check that the just defined Bogoliubov quasiparticle operators γ, $\gamma^\dagger$ are really fermionic, we need to check that they satisfy the fermionic anti-commutation relations

$$\left\{\gamma_{\mathbf{k}\uparrow}, \gamma^\dagger_{\mathbf{k}\uparrow}\right\} = \gamma_{\mathbf{k}\uparrow}\gamma^\dagger_{\mathbf{k}\uparrow} + \gamma^\dagger_{\mathbf{k}\uparrow}\gamma_{\mathbf{k}\uparrow} = |u_{\mathbf{k}}|^2 + |v_{\mathbf{k}}|^2 \stackrel{!}{=} 1. \tag{1.7}$$

This is consistent with the normalization conditions of the BCS ground state $|\psi_{\mathrm{BCS}}\rangle$ (1.5) and allows us to find the inverse transformation

$$\begin{pmatrix} c_{\mathbf{k}\uparrow} \\ c^\dagger_{-\mathbf{k}\downarrow} \end{pmatrix} = \begin{pmatrix} u^*_{\mathbf{k}} & v_{\mathbf{k}} \\ -v^*_{\mathbf{k}} & u_{\mathbf{k}} \end{pmatrix} \begin{pmatrix} \gamma_{\mathbf{k}\uparrow} \\ \gamma^\dagger_{-\mathbf{k}\downarrow} \end{pmatrix}. \tag{1.8}$$

We can now use this transformation and replace all electron operators c, $c^\dagger$ in the BCS Hamiltonian (1.2) by Bogoliubov quasiparticles and we will find

$$\begin{aligned} H_{\mathrm{BCS}} = \sum_{\mathbf{k}} & \gamma^\dagger_{\mathbf{k}\uparrow}\gamma_{\mathbf{k}\uparrow}\left(|u_{\mathbf{k}}|^2\xi_{\mathbf{k}} - |v_{\mathbf{k}}|^2\xi_{\mathbf{k}} + v_{\mathbf{k}}u^*_{\mathbf{k}}\Delta^*_{\mathbf{k}} + u_{\mathbf{k}}v^*_{\mathbf{k}}\Delta_{\mathbf{k}}\right) \\ & + \gamma^\dagger_{\mathbf{k}\uparrow}\gamma^\dagger_{-\mathbf{k}\downarrow}\underbrace{\left(2u_{\mathbf{k}}v_{\mathbf{k}}\xi_{\mathbf{k}} + v^2_{\mathbf{k}}\Delta^*_{\mathbf{k}} - u^2_{\mathbf{k}}\Delta_{\mathbf{k}}\right)}_{\text{non-diagonal term}} \\ & + \gamma_{-\mathbf{k}\downarrow}\gamma_{\mathbf{k}\uparrow}\underbrace{\left(2v^*_{\mathbf{k}}u^*_{\mathbf{k}}\xi_{\mathbf{k}} - {u^*_{\mathbf{k}}}^2\Delta^*_{\mathbf{k}} + {v^*_{\mathbf{k}}}^2\Delta_{\mathbf{k}}\right)}_{\text{non-diagonal term}} \\ & + \gamma_{-\mathbf{k}\downarrow}\gamma^\dagger_{-\mathbf{k}\downarrow}\left(|v_{\mathbf{k}}|^2\xi_{\mathbf{k}} - |u_{\mathbf{k}}|^2\xi_{\mathbf{k}} - u^*_{\mathbf{k}}v_{\mathbf{k}}\Delta^*_{\mathbf{k}} - v^*_{\mathbf{k}}u_{\mathbf{k}}\Delta_{\mathbf{k}}\right). \end{aligned} \tag{1.9}$$

In order to get a Hamiltonian truly diagonal in Bogoliubov quasiparticles we need to make sure that the non-diagonal terms vanish. Both conditions are equivalent, so we will focus only on the first. For this it is useful to rewrite the coherence factors and the BCS mean-field

parameters as

$$\Delta_{\mathbf{k}} = |\Delta_{\mathbf{k}}| e^{i\phi_{\mathbf{k}}} \tag{1.10}$$
$$u_{\mathbf{k}} = |u_{\mathbf{k}}| e^{i\alpha_{\mathbf{k}}} \tag{1.11}$$
$$v_{\mathbf{k}} = |v_{\mathbf{k}}| e^{i\beta_{\mathbf{k}}}, \tag{1.12}$$

where $\phi_{\mathbf{k}}$, $\alpha_{\mathbf{k}}$, $\beta_{\mathbf{k}} \in \mathbb{R}$. We then need to find any solution to

$$\begin{aligned} 0 &= 2u_{\mathbf{k}} v_{\mathbf{k}} \xi_{\mathbf{k}} + v_{\mathbf{k}}^2 \Delta_{\mathbf{k}}^* - u_{\mathbf{k}}^2 \Delta_{\mathbf{k}} \\ &= 2\xi_{\mathbf{k}} |u_{\mathbf{k}}||v_{\mathbf{k}}| e^{i(\alpha_{\mathbf{k}}+\beta_{\mathbf{k}})} + |\Delta_{\mathbf{k}}| \left(|v_{\mathbf{k}}|^2 e^{i(2\beta_{\mathbf{k}}-\phi_{\mathbf{k}})} - |u_{\mathbf{k}}|^2 e^{i(2\alpha_{\mathbf{k}}+\phi_{\mathbf{k}})} \right). \end{aligned} \tag{1.13}$$

A very simple solution is found if we choose $\phi_{\mathbf{k}} = \beta_{\mathbf{k}}$ and $\alpha_{\mathbf{k}} = 0$. This choice is permitted, because we previously did not have any other conditions on the parameters which would cause a contradiction. We thus end up with the rather simple condition

$$2\xi_{\mathbf{k}} |u_{\mathbf{k}}||v_{\mathbf{k}}| + |\Delta_{\mathbf{k}}| \left(|v_{\mathbf{k}}|^2 - |u_{\mathbf{k}}|^2 \right) = 0. \tag{1.14}$$

After some elementary transformations we find

$$\begin{aligned} |u_{\mathbf{k}}|^2 &= \frac{1}{2} \left(1 + \frac{\xi_{\mathbf{k}}}{\sqrt{\xi_{\mathbf{k}}^2 + |\Delta_{\mathbf{k}}|^2}} \right) \\ |v_{\mathbf{k}}|^2 &= \frac{1}{2} \left(1 - \frac{\xi_{\mathbf{k}}}{\sqrt{\xi_{\mathbf{k}}^2 + |\Delta_{\mathbf{k}}|^2}} \right) \\ u_{\mathbf{k}} v_{\mathbf{k}} &= \frac{\Delta_{\mathbf{k}}}{2\sqrt{\xi_{\mathbf{k}}^2 + |\Delta_{\mathbf{k}}|^2}}. \end{aligned} \tag{1.15}$$

Using all this in (1.9) we find the diagonal form of the BCS Hamiltonian

$$H_{\mathrm{BCS}} = \sum_{\mathbf{k}} \sqrt{\xi_{\mathbf{k}}^2 + |\Delta_{\mathbf{k}}|^2} \left(\gamma_{\mathbf{k}\uparrow}^\dagger \gamma_{\mathbf{k}\uparrow} + \gamma_{-\mathbf{k}\downarrow}^\dagger \gamma_{-\mathbf{k}\downarrow} \right) + \xi_{\mathbf{k}} \tag{1.16}$$

We have finally found the diagonal form of the BCS Hamiltonian in terms of Bogoliubov quasiparticles. This is very good and sufficient for many applications.
For Andreev reflection the Bogoliubov quasiparticles have the disadvantage that they do not have a well defined charge, because they are linear combinations of both electronic creation and annihilation operators. This can be addressed by adding (subtracting) a Cooper pair via the Cooper pair creation (annihilation) operator $S^\dagger$ (S) [38, 39]. We will then end up with

Operator	charge	momentum	spin
$\gamma^\dagger_{e\mathbf{k}\uparrow} = u^*_{\mathbf{k}} c^\dagger_{\mathbf{k}\uparrow} - v^*_{\mathbf{k}} S^\dagger c_{-\mathbf{k}\downarrow}$	$-e$	$+\mathbf{k}$	$+\frac{\hbar}{2}$
$\gamma^\dagger_{e-\mathbf{k}\downarrow} = v^*_{\mathbf{k}} S^\dagger c_{\mathbf{k}\uparrow} + u^*_{\mathbf{k}} c^\dagger_{-\mathbf{k}\downarrow}$	$-e$	$-\mathbf{k}$	$-\frac{\hbar}{2}$
$\gamma_{e\mathbf{k}\uparrow} = u_{\mathbf{k}} c_{\mathbf{k}\uparrow} - v_{\mathbf{k}} S c^\dagger_{-\mathbf{k}\downarrow}$	$+e$	$-\mathbf{k}$	$-\frac{\hbar}{2}$
$\gamma_{e-\mathbf{k}\downarrow} = v_{\mathbf{k}} S c^\dagger_{\mathbf{k}\uparrow} + u_{\mathbf{k}} c_{-\mathbf{k}\downarrow}$	$+e$	$+\mathbf{k}$	$+\frac{\hbar}{2}$

Table 1.1: List of electron-like Bogoliubov quasiparticle creation and annihilation operators and their change to the system's charge, momentum and spin.

electron-like and hole-like Bogoliubov quasiparticle operators γ_e and γ_h, respectively. They can be defined as

$$\gamma_{e,\mathbf{k}\uparrow} = u_{\mathbf{k}} c_{\mathbf{k}\uparrow} - v_{\mathbf{k}} S c^\dagger_{-\mathbf{k}\downarrow} \tag{1.17}$$

$$\gamma_{h,\mathbf{k}\uparrow} = u_{\mathbf{k}} S^\dagger c_{\mathbf{k}\uparrow} - v_{\mathbf{k}} c^\dagger_{-\mathbf{k}\downarrow} \tag{1.18}$$

$$\gamma^\dagger_{e,-\mathbf{k}\downarrow} = v^*_{\mathbf{k}} S^\dagger c_{\mathbf{k}\uparrow} + u^*_{\mathbf{k}} c^\dagger_{-\mathbf{k}\downarrow} \tag{1.19}$$

$$\gamma^\dagger_{h,-\mathbf{k}\downarrow} = v^*_{\mathbf{k}} c_{\mathbf{k}\uparrow} + u^*_{\mathbf{k}} S c^\dagger_{-\mathbf{k}\downarrow}. \tag{1.20}$$

Comparing the operators, it is easy to see that the hole-like and the electron-like Bogoliubov quasiparticle operators are related by

$$\gamma_{h,\mathbf{k}\sigma} = S^\dagger \gamma_{e,\mathbf{k}\sigma}. \tag{1.21}$$

As the Cooper pair creation (annihilation) operator $S^\dagger$ (S) does not change the systems total momentum or spin, but only creates (annihilates) two electron charges, we can restrict ourselves to the electron-like Bogoliubov quasiparticle operators and add or subtract Cooper pairs as needed. For convenience, the electron-like Bogoliubov quasiparticle operators and their effect on the system's charge, momentum and spin are listed in Table 1.1.

1.3 Basic Theory of Andreev Reflection

Having covered the basics of superconductivity in the previous section we will now turn to highlighting the effects that occur when a superconductor is brought into contact with a non-superconducting material such as a normal metal. This situation commonly occurs in induced topological superconductor systems. In these systems a topological insulator is brought into contact with a regular s-wave superconductor. Cooper pairs from the superconductor will then leak into the topological insulator, inducing a pairing amplitude and consequently a superconducting gap. This induced superconducting gap decreases with increasing distance

from the superconductor, though the exact form and magnitude of this decrease is difficult to calculate [23, 40]. Correctly understanding this superconducting proximity effect and being able to calculate its magnitude will enable us to build more precise models in the future.
Closely related is the so called Andreev reflection, where a single electron from a normal metal impinges on a superconductor and gets reflected back as a hole. We will have a look at these phenomena from the point of view of the Andreev reflection. Hereby we shall restrict ourselves to plain singlet s-wave superconductors, as they are the most common to be found in systems proposed for hosting Majorana zero modes. Extension to unconventional superconductors is certainly possible [35], but not required for our use case and thus outside the scope of this work.
In the following we will first introduce the phenomenology of Andreev reflection and then the two most common theoretical approaches to the phenomenon. In section 2.1 we will give our own approach of modeling Andreev reflection in a tight-binding model and which allows for self-consistent calculation of the decreasing pairing amplitude in the normal metal. Throughout this section we will refer to the Andreev reflection as effect between a normal metal and a superconductor, even though it is straight forward to replace the normal metal by other materials such as semimetals or topological insulators.

1.3.1 Phenomenology

Andreev reflection occurs at a normal metal – superconductor interface due to their differing band structures. The band structure for a prototypical metal and a superconductor in momentum space is given in Figure 1.3. Here one can clearly see that the metal has available states at Fermi energy E_F, whereas the band structure of the superconductor resembles that of an ordinary insulator and thus has no available states at Fermi energy. When metal and superconductor are brought into contact, the general shape of the band structure will persist. Consequently, if an electron at Fermi level from the metal moves towards the superconductor, it cannot penetrate the superconductor and will be reflected, as would happen at a metal – insulator interface. One would therefore assume that only electrons from the metal which have an energy larger than the superconducting gap Δ of the superconductor can pass the metal – superconductor interface.
However, unlike an insulator a superconductor has a reservoir of Cooper pairs to which pairs can be added or subtracted at will. Indeed, it has been shown both experimentally and theoretically that even electrons in the metal which have an energy within the superconducting gap can enter the superconductor via the process of the so-called Andreev reflection [39, 41, 42].

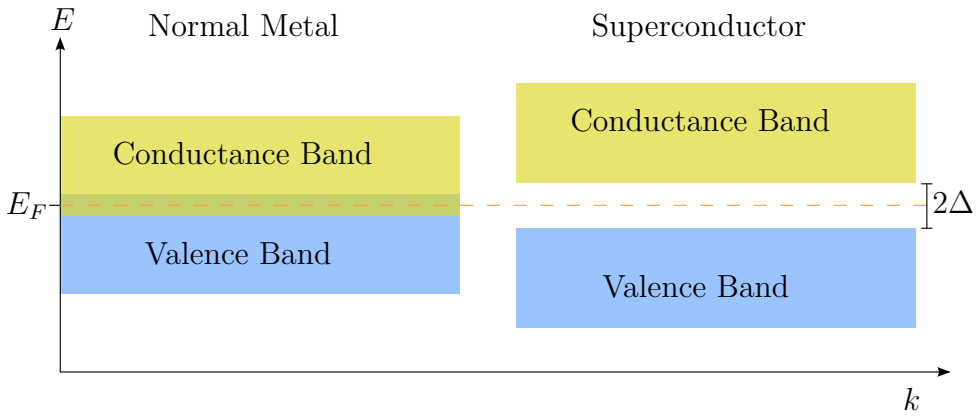

Figure 1.3: Band structure of a prototype metal and superconductor, respectively.

In order to describe the process of Andreev reflection, it is instructive to start with a single electron in the normal metal with an energy within the superconducting gap of the superconductor moving towards the latter, as depicted in Figure 1.4. Upon reaching the interface the electron has two options. It can either be specularly reflected, as it would be when the superconductor would be an insulator. Or it can enter the superconductor as a short-lived evanescent mode. In this case Andreev reflection will occur and a hole will be reflected back into the normal metal. The hole will have approximately the opposite momentum of the original electron [39, 40]. As a result a total charge of two electron charges is transferred from the normal metal to the superconductor and a Cooper pair is formed and added to the already present sea of Cooper pairs in the superconductor.
Another very pictorial description is given in Figure 1.5. Note that in this description it may appear as if energy conservation is violated. However, this is only an artifact of describing the process by breaking it up into several steps. Considering everything at once and comparing initial and final state we can confirm that there is no spurious appearance or disappearance of energy in this process and thus energy is indeed conserved.
Before finishing the phenomenological description of the Andreev reflection, a couple of remarks are in order. Contrary to common believe, the momentum of the Andreev reflected hole is not exactly the opposite of the momentum of the incident electron [39, 40]. However, the difference is generally very small and can usually be neglected. Another important point that should be mentioned is that Andreev reflection does not happen perfectly at the normal metal – superconductor interface, but rather in a finite region within about one coherence length inside the superconductor [39]. Furthermore, we would like to point out that intimately related to the Andreev reflection is the superconducting proximity effect as the opposite effect [40, 43]. The superconducting proximity effect describes the penetration of Cooper pairs from the superconductor into the normal metal, leading to a finite Cooper pair amplitude in

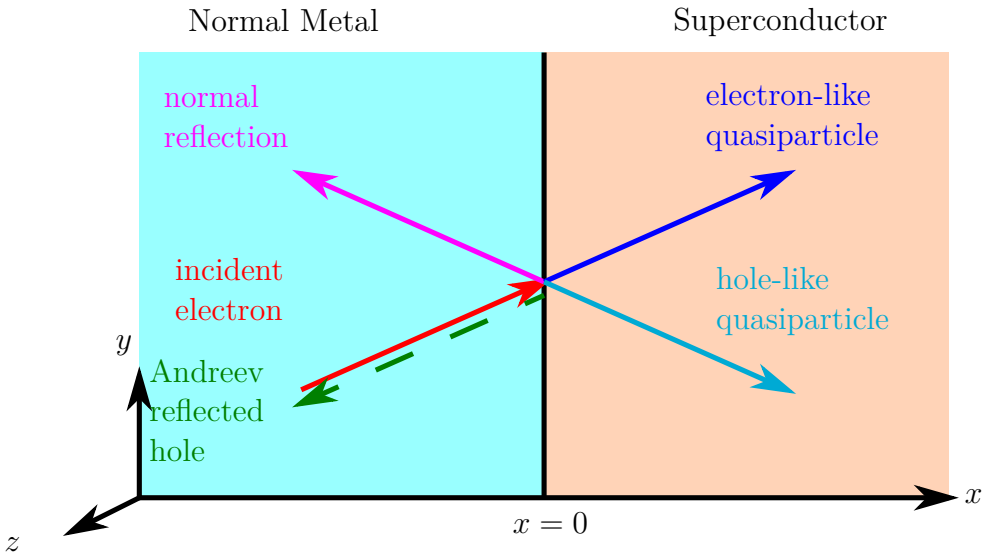

Figure 1.4: Normal metal – superconductor junction. Incident electron from the metal either gets normally reflected or retro-reflected as a hole. In the latter case quasiparticle excitations are created in the superconductor, finally resulting an the addition of a Cooper pair in the superconductor.

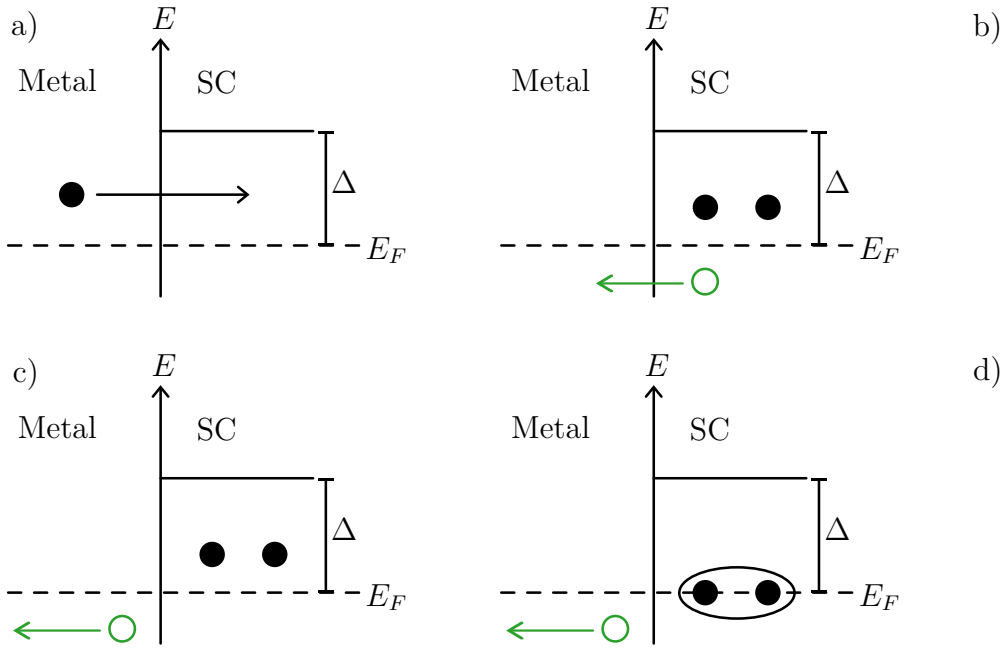

Figure 1.5: Pictorial description of Andreev reflection. a) An electron from the normal enters the superconductor as evanescent electron-like Bogoliubov quasiparticle. b) A pair of electron-like and hole-like Bogoliubov quasiparticles is created. c) The hole-like Bogoliubov quasiparticle leaves the superconductor and enters the normal metal as a hole. d) The two electron-like Bogoliubov quasiparticles decay to the ground state and get added to the condensate as Cooper pairs.

a region of the normal metal close to the superconductor, despite the absence of an attractive interaction [43]. In fact, as we shall see later, both effects can be described using the same interaction Hamiltonian.

1.3.2 Wave Matching

The so-called wave matching approach is a very common model for Andreev reflection [35, 39]. It works by splitting the space into two half-spaces, for example along the x-direction. The lower half-space $x < 0$ is then assumed to be filled with the normal metal, while the upper half-space $x > 0$ is filled with the superconductor, see Figure 1.4. Directions y and z are assumed to be infinite and can therefore be treated in momentum space. The method is well described in many textbooks and publications [35, 39, 44, 45]. We will therefore restrict ourselves to a brief overview of the method to describe the interesting physics and will not go into the mathematical details.
The entire system can be described by a single Bogoliubov–de Gennes (BdG) Hamiltonian

$$\mathcal{H}_{\mathrm{BdG}} = \begin{pmatrix} -\frac{\hbar^2}{2m}\nabla^2 - \mu & \Delta_0\Theta(x) \\ \Delta_0\Theta(x) & \frac{\hbar^2}{2m}\nabla^2 + \mu \end{pmatrix}. \tag{1.22}$$

Here μ denotes the chemical potential, $\Delta_0 \in \mathbb{R}$ the superconducting order parameter and $\Theta(x)$ the Heaviside theta function. This results in a step-like behavior of the superconducting order parameter, which is not physical, but commonly done. As mentioned before, in real systems the superconducting order parameter extends into the normal metal, where it eventually decays to zero [43]. Next we need to calculate the eigenfunctions $\Psi(\mathbf{r})$ separately in both regions, $x < 0$ and $x > 0$. We thus need to solve

$$\mathcal{H}_{\mathrm{BdG}}\Psi(\mathbf{r}) = E\Psi(\mathbf{r}). \tag{1.23}$$

We then end up with two wave functions $\Psi_{\mathrm{NM}}(\mathbf{r})$ and $\Psi_{\mathrm{SC}}(\mathbf{r})$, for the normal metal region and the superconducting region, respectively. Next we need to choose the parameters of the wave functions to ensure continuity of the solution of the entire system at $x = 0$. This requires

$$\Psi_{\mathrm{NM}}(x = 0, y, z) = \Psi_{\mathrm{SC}}(x = 0, y, z) \tag{1.24}$$

and

$$\frac{d}{dx}\Psi_{\mathrm{NM}}(x = 0, y, z) = \frac{d}{dx}\Psi_{\mathrm{SC}}(x = 0, y, z). \tag{1.25}$$

Instead of reproducing the lengthy but straight forward calculations, which are already nicely

covered in the aforementioned textbooks and publications, we will instead focus on discussing the physically interesting results. We limit our discussion to the case that the energy E lies inside the superconducting gap of the superconducting part of the system, i.e. $|E| < \Delta_0$. The first thing we notice is that the solution in the superconductor decays exponentially, as expected, since the energy lies within the superconducting gap. This furthermore indicates that Andreev reflection is not happening directly at the interface, but also within a small region within the superconductor. Another thing we can observe from the solutions is that the wave function describing the hole within the normal metal region has only approximately opposite momentum of the electron wave function in the normal metal region, $\mathbf{k}_{\text{hole}} \approx -\mathbf{k}_{\text{electron}}$. However, the deviation is small and can usually be neglected for most applications.

The most interesting result though is arguably the specularly reflected electron wave function in the normal metal region. Such a reflected wave function would also be expected from a simple potential step function. In the problem at hand however it turns out that the coefficient of reflection $|r|^2 < 1$, meaning that not all electrons are reflected. This is highly interesting, because we have earlier found that there is no stable solution on the superconductor side of the junction, meaning that electrons that do not get specularly reflected back into the normal metal cannot simply enter the superconductor. The only solution for the charge that is transported to the junction from the normal metal and not reflected back is to be added to the condensate of the superconductor, i.e. forming an additional Cooper pair in the superconductor. Remember that in BCS theory of superconductivity the number of particles in the superconductor is not fixed and thus addition and removal of Cooper pairs is easily possible [33]. The second electron which is needed to create the Cooper pair is coming from the hole that is reflected back into the normal metal.

As an extension to the regular wave matching approach, it has been proposed to add a variable potential barrier to the interface of the normal metal–superconductor system [39]. This allows to effectively mimic a normal metal–insulator–superconductor system and smoothly change back and forth to the normal metal–superconductor system. Mathematically this is implemented by adding a variable strength delta potential $V(x) = H\delta(x)$ to the Hamiltonian (1.22), where H is the strength of the barrier. The potential strength can be expressed dimensionless as $Z = k_F H/2\epsilon_F = H/\hbar v_F$.

The Hamiltonian of the system can then be written as

$$\mathcal{H}_{\text{BdG}} = \begin{pmatrix} -\frac{\hbar^2}{2m}\nabla^2 - \mu + V(x) & \Delta_0\Theta(x) \\ \Delta_0\Theta(x) & \frac{\hbar^2}{2m}\nabla^2 + \mu - V(x) \end{pmatrix}. \tag{1.26}$$

The calculation of the wave functions is analogous to what has been described above and

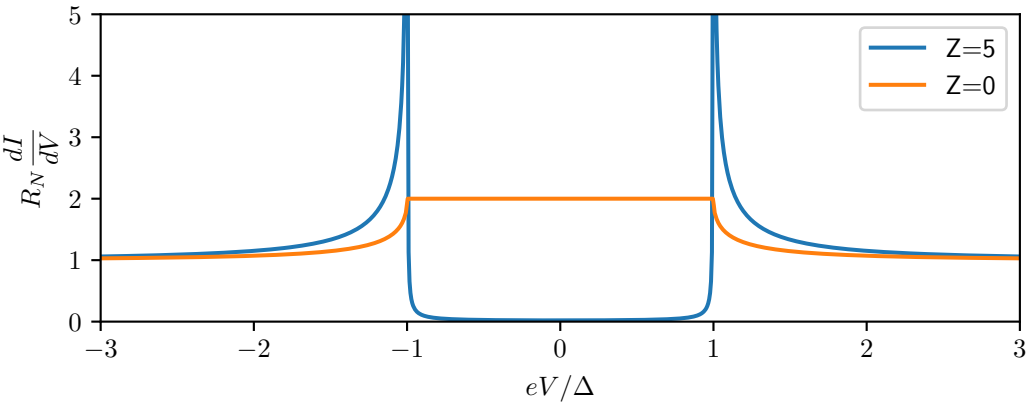

Figure 1.6: Differential conductance through a normal metal–superconductor interface with a variable barrier at the interface. The blue curve ($Z = 5$) denotes the case of a strong barrier, roughly corresponding to a normal metal–insulator–superconductor junction. The orange curve ($Z = 0$) denotes a perfect normal metal–superconductor junction.

will thus not be repeated here. What is interesting to note is that once the wave functions are constructed, one can then calculate the differential conductance across the normal metal–superconductor junction for different barrier strengths. The differential conductance is shown in Figure 1.6 for the two limiting cases of a high barrier ($Z = 5$) and no barrier ($Z = 0$). The high barrier case closely resembles the tunneling density of states of a superconductor as measured by scanning tunneling microscopy (STM) experiments [46, 47]. The case with no barrier is in principle inaccessible to STM measurements, but can be realized in specially manufactured samples and has indeed been observed in experiments [42]. Here it is especially interesting to observe that the differential conductance for energies within the superconducting gap is exactly two. This somewhat surprising feature comes from the fact that for those energies the direct electron transfer from the metal to the superconductor is impossible and thus all incoming electrons get Andreev reflected. Therefore, for every incoming electron exactly two electron charges get transferred across the interface, raising the differential conductance to two.

Before concluding this brief description of the wave matching approach, it seems instructive to briefly note its advantages and disadvantages. Advantageous of this approach is that it is an analytic approach which does not need numerics and thus allows for greater insight into what is happening, for example that the holes are reflected with approximately the opposite momentum of the incident electron. Another advantage is that the variable barrier allows us to compare the theory with different experimental setups such as STM measurements or

specifically fabricated normal metal–superconductor junctions. It is also interesting in a sense as it can show that electrons from the normal metal can enter the superconductor within the superconducting gap region as exponentially decaying evanescent modes and thereby shows that Andreev reflection happens not only at the interface, but within a region close to the interface. However, the analytic nature of the wave matching technique is also one of its biggest downsides, as it cannot easily be extended to more complicated normal metal–superconductor models such as multi-band models. This is because multi-band models will lead to Hamiltonian matrices larger than the present 4×4 case. For such larger matrices it is in principle impossible to construct analytic solutions, unless special symmetries can be exploited. While numerical solutions to larger matrices can easily be found, those solutions by their very nature of being numeric instead of analytic cannot be used for the matching of the wave functions. The wave matching approach is thus not suitable for real space tight-binding models, where large matrices are frequently encountered. Another disadvantage of the wave matching approach is the unphysical assumption of having a step-function-like change of the superconducting order parameter.

1.3.3 Tunneling Hamiltonian

Another common approach to Andreev reflection is the tunneling Hamiltonian approach. In this approach the total Hamiltonian H_{tot} of the system is constructed from an unperturbed normal metal H_{NM}, and unperturbed superconductor H_{SC} and a tunneling term H_T,

$$H_{\text{tot}} = H_{\text{NM}} + H_{\text{SC}} + H_T. \tag{1.27}$$

The tunneling Hamiltonian has been used since the early days of BCS theory [38, 48] and has remained popular since [49]. This approach is well suited for equilibrium phenomena, but has some difficulties when being applied to non-equilibrium phenomena such as Andreev reflection. In a non-equilibrium setting the above formulation is lacking moving electrons on the normal metal and the superconductor side, as these parts are considered unperturbed. In the past the tunneling Hamiltonian approach has thus been criticized as unsuitable for Andreev reflection and indeed in its basic form it cannot describe the differential current in a normal metal–superconductor case, but only for the normal metal–insulator–superconductor case [39, 50]. However, it has later been shown that the tunneling Hamiltonian approach can reproduce the differential conductance of the wave matching approach and is indeed equivalent when using the tunneling as a perturbation in perturbation theory up to infinite order [41]. The tunneling Hamiltonian approach thus lends itself to the application in real space tight-

binding models. However, it is still difficult to use the tunneling Hamiltonian approach to calculate the spatial variation of the Cooper pair pairing amplitude across the normal metal–superconductor interface. The way it is formulated in (1.27) still assumes a step-function for the superconducting order parameter.
In an attempt to overcome these limitations, we will have a fresh look at Andreev reflection in section 2.1, where we will discuss a method for obtaining the spatial variation of the superconducting order parameter in a self-consistent way.

1.4 Induced Topological Superconductors

Having introduced the basic notions of superconductivity, we will now explain how superconductors can be used to turn topological insulators into induced topological superconductors and how Majorana zero modes arise in such induced topological superconductors, as briefly touched upon in section 1.1. The idea of using conventional s-wave superconductors to turn topological insulators has been pioneered by Fu and Kane in 2008 [9]. We will consequently refer to this model as Fu-Kane model.
In their work Fu and Kane considered the two dimensional surface of a three dimensional superconductor which is in contact with a conventional s-wave superconductor, see Figure 1.7. The surface of a three dimensional strong topological insulator is gapless, with an odd number of Dirac nodes [51]. To get a clear understanding, we consider a generic strong topological insulator which is finite in z-direction and infinite in x- and y-directions. It thus has two surfaces parallel to the x-y-plane and the momenta k_x and k_y are good quantum numbers. Plotting the band structure this system we find that the insulating bulk is augmented by a single Dirac cone of surface states traversing the gap. This is depicted in Figure 1.8a. Having a close look at the localization of the states inside the bulk gap, we find that they are very strongly localized at either the top or the bottom surface of the system, see Figure 1.8b.
This strong localization of the surface states at the surface of the topological insulator in conjunction with the rather large bulk gap allows for creating an effective model around the Dirac node by considering only the two dimensional surface and neglecting all bulk states. The effective Hamiltonian is then given by

$$H_{\mathrm{TI}} = \sum_{\mathbf{k}} B_{\mathbf{k}}^{\dagger} \left[\sigma_x k_x + \sigma_y k_y - \sigma_0 \mu \right] B_{\mathbf{k}}, \tag{1.28}$$

where the electron annihilation operators are given by $B_{\mathbf{k}} = (b_{\mathbf{k}\uparrow}, b_{\mathbf{k}\uparrow})^{\top}$, the Pauli matrices in spin space are denoted by σ_i (with σ_0 being the unit matrix), and the chemical potential is

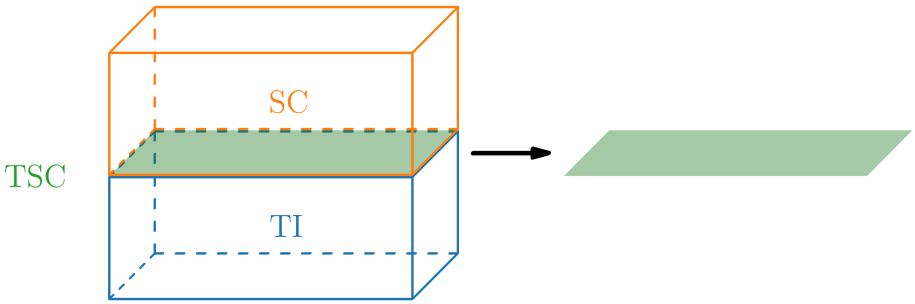

Figure 1.7: Two dimensional induced topological superconductor (TSC) at the interface between a three dimensional topological insulator (TI) and a three dimensional conventional s-wave superconductor (SC). The Fu-Kane model only considers the two dimensional superconductor, as indicated by the green plane on the right.

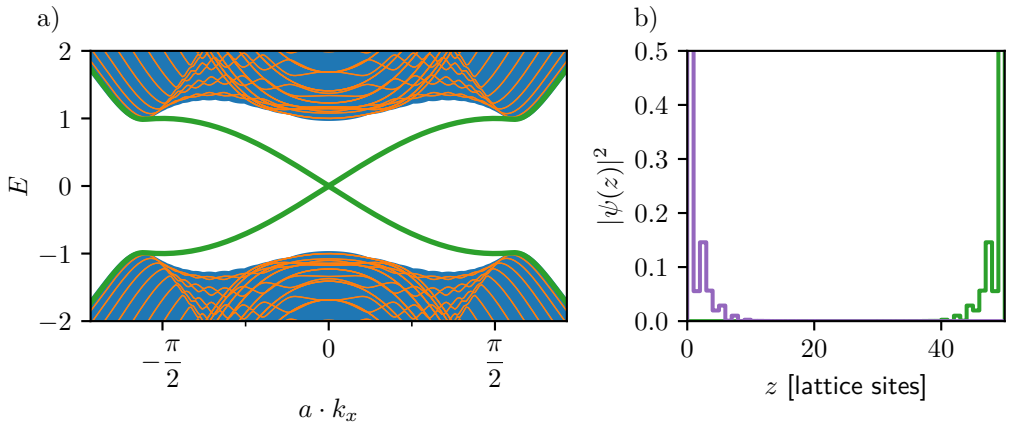

Figure 1.8: (a) Band structure of an ideal three dimensional topological insulator. Shown in blue is the bulk bandstructure. The band structure for system with finite extension in z-direction (50 lattice sites) is shown in orange, with the surface states marked green, for clarity. (b) Probability density of the surface states at the Dirac node along the finite z-direction. The states are strongly localized either at the bottom surface (purple) or the top surface (green) and completely absent in the bulk.

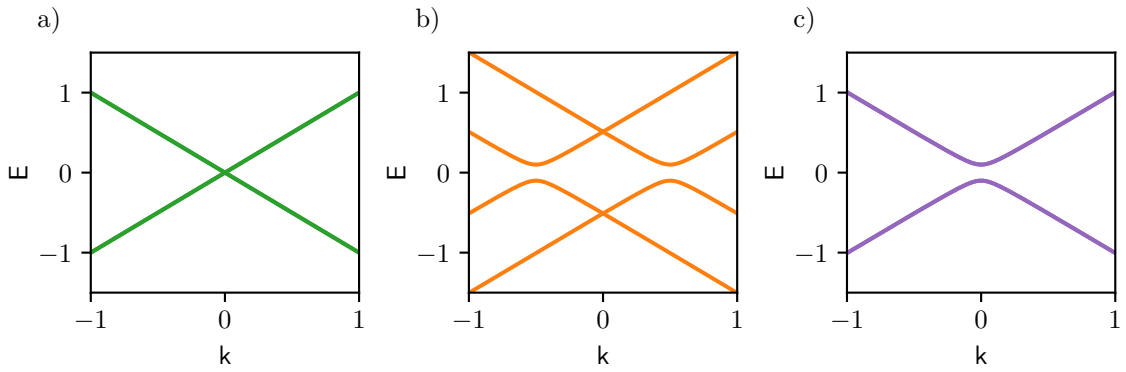

Figure 1.9: Band structure of the two dimensional surface of a topological insulator (a), with superconducting proximity effect (b) and with ferromagnetic exchange interaction (c). The pure topological insulator surface state is gapless (a), whereas the addition of superconducting proximity effect or ferromagnetic exchange interaction opens a gap (b), (c). We would like to stress that (b) and (c) belong to different topological phases.

denoted by μ. The corresponding bandstructure is gapless and given in Figure 1.9a.
The superconducting proximity effect can be incorporated by first extending the Hamiltonian to a Bogoliubov-de Gennes Hamiltonian and then adding the Cooper pair pairing amplitude $\Delta = \Delta_0 e^{i\phi}$. The Hamiltonian then becomes

$$H_{\text{TI,SC prox}} = \frac{1}{2}\sum_{\mathbf{k}} \tilde{B}^\dagger_{\mathbf{k}}\left[\rho_0\sigma_x k_x + \rho_z\sigma_y k_y) - \mu\rho_z\sigma_0 + \Delta_0(-\rho_y\sigma_y\cos\phi + \rho_x\sigma_y\sin\phi)\right]\tilde{B}_{\mathbf{k}}. \quad (1.29)$$

Here, $\tilde{B}_{\mathbf{k}} = (b_{\mathbf{k}\uparrow}, b_{\mathbf{k}\downarrow}, b^\dagger_{-\mathbf{k}\uparrow}, b^\dagger_{-\mathbf{k}\downarrow})^\top$ and ρ_i are the Pauli matrices in particle-hole space. The bandstructure is plotted in Figure 1.9b and can be calculated explicitly as

$$E = \pm\sqrt{(|\mathbf{k}|^2 \pm \mu)^2 + \Delta_0^2}. \quad (1.30)$$

Fu and Kane have pointed out that this resembles the low energy spectrum of a spinless $p_x + ip_y$ superconductor when $\mu \gg \Delta_0$ and both systems are indeed formally equivalent [9]. Though one crucial difference between the spinless $p_x + ip_y$ superconductor and the induced topological superconductor in the Fu-Kane model is that the latter is time reversal symmetric, while the former is not [9].
As a consequence, Fu and Kane have predicted that Majorana zero modes would form when the induced topological superconductor is brought into contact with a ferromagnet insulator in a setup as depicted in Figure 1.1a. This is because the ferromagnetic exchange interaction also induces a gap in the surface states of a topological insulator, albeit a topologically

distinct one. Hence, there needs to be a gap closing point between the topological insulator–superconductor system and the topological insulator–ferromagnet system. This boundary is where the Majorana zero modes are located [9].
For explicitness, we will give the Hamiltonian of the topological insulator surface state with induced ferromagnetic exchange interaction,

$$H_{\text{TI,FM prox}} = \sum_{\mathbf{k}} B_{\mathbf{k}}^{\dagger} \left[\sigma_x k_x + \sigma_y k_y - \sigma_0 \mu + J \sigma_z \right] B_{\mathbf{k}}. \tag{1.31}$$

Here J denotes the strength of the ferromagnetic exchange interaction. The corresponding gapless bandstructure is given in Figure 1.9c.
At this point we would like to emphasize again that gapped states in Figure 1.9b and Figure 1.9c correspond to different topological phases and gap closing will occur if one smoothly interpolates between these two phases, for example by adding ferromagnetic exchange interaction to the topological insulator with superconducting proximity effect (1.29) and slowly changing the strength of the exchange interaction.
Furthermore we would like to point out that in these calculations it does not matter what the origin of the ferromagnetic exchange interaction is. It could for example originate from a ferromagnetic insulator, from an external magnetic field or from magnetically doping the surface of the topological insulator. Tough the origin of the ferromagnetic exchange interaction may have practical consequences in experimental setups, as a ferromagnetic insulator in contact with a superconductor (as shown in Figure 1.1a) will usually suppress superconductivity and thus lead to a metallic state, which would interfere with the observation of the gap closing due to a topological phase transition. Similarly, an external magnetic field may induce vortices inside the superconductor, again changing the bandstructure of the system. Thus it may be favorable to induce the ferromagnetic gap in the topological insulator's surface states via ferromagnetic doping.
Before concluding the introduction of the Fu-Kane model, we would like to remark that Fu and Kane have also proposed that Majorana zero modes could be created in an induced topological superconductor when different superconductors with differing phases of their superconducting order parameters are placed on top of the topological insulator [9]. In such a setup with many different superconductors whose phases can be independently controlled it would be possible to move Majorana zero modes, create entanglement between Majorana zero modes and move them around each other to perform the so-called braiding, which could be used to probe the non-Abelian character of the Majorana zero modes [9]. However, this approach using multiple independent superconductors which can be independently tuned works a bit differently than

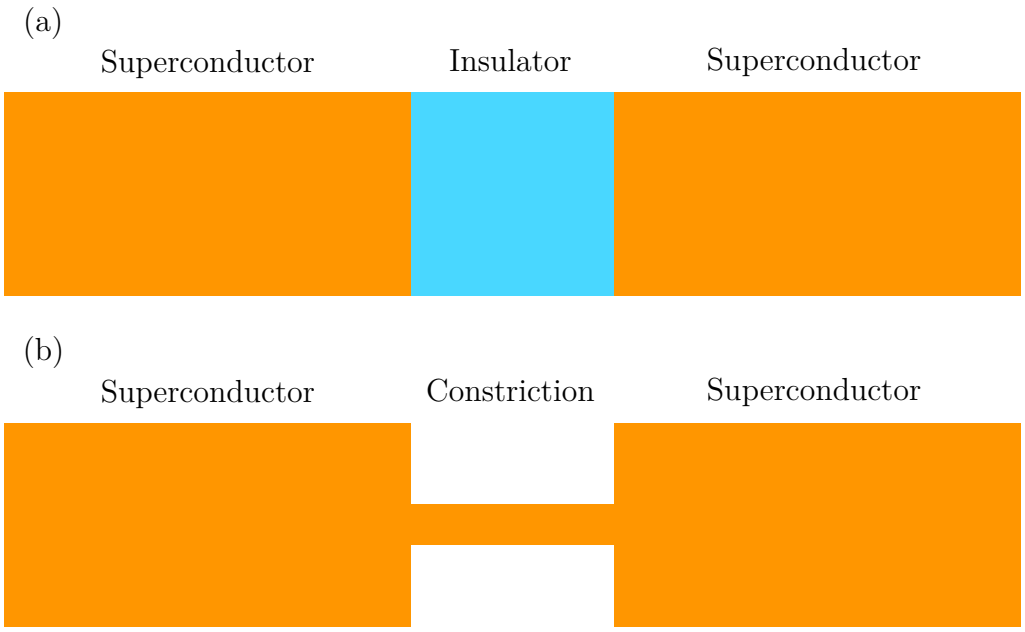

Figure 1.10: Different Josephson junctions. (a) Two separate superconductors connected by either an insulator or a normal metal. (b) One continuous superconductor which is severely constricted in a finite region.

the aforementioned use of superconductivity and ferromagnetism and is thus outside the scope of the present work.

1.5 Basics of Josephson Junctions

Josephson junctions are systems where two superconductors are physically separated and connected via a weak link, as depicted in Figure 1.10. The weak link may either be a normal metal, an insulator or simply a constriction within the superconductor.
Josephson junctions exhibit two very characteristic effects. One is the so called DC Josephson effect and is the sustained flow of electricity through the junction in the absence of any external voltage. The other is the AC Josephson effect and is an oscillating current arising in a situation where a constant voltage is kept across the junction. There are two fundamental approaches to deriving the Josephson effects, one from a phenomenological description via Ginzburg-Landau theory, the other via a microscopic description within the framework of BCS theory.
Though the theory of Josephson junctions has long been described in text books, we would like to briefly recap the basics using BCS theory and then explain how Majorana zero modes give rise to a characteristic form of the DC Josephson effect. The system of a Josephson junction with two independent superconductor separated by a small insulating barrier can most easily

described by

$$H = H_L + H_R + H_T, \tag{1.32}$$

where H_L (H_R) describes the left (right) superconductor and H_T some tunneling in between. Without considering the general case of three dimensional superconductors, we will focus on the simplification of one dimensional superconductors. Furthermore, in preparation for the case of topological superconductors with Majorana zero modes at their ends, we will assume the superconductors to be spinless. The superconductors can thus be written as

$$\begin{aligned} H_a = \sum_{j=1}^{N} \Big[& -w(c_{a,j}^\dagger c_{a,j+1} + c_{a,j+1}^\dagger c_{a,j}) - \mu\Big(c_{a,j}^\dagger c_{a,j} - \frac{1}{2}\Big) \\ & + \Delta e^{i\phi_a} c_{a,j} c_{a,j+1} + \Delta e^{-i\phi_a} c_{a,j+1}^\dagger c_{a,j}^\dagger \Big], \end{aligned} \tag{1.33}$$

where $a = L/R$ is used to distinguish between the left and right superconductor and ϕ_a is the phase of the respective superconducting order parameter, with $\phi = \phi_R - \phi_L$ being the relative phase.. The model (1.33) is know as Kitaev-chain and, depending on the choice of the parameters, can be either a topological superconductor or a trivial superconductor [7]. The tunneling can be simply described by

$$H_T = -t(c_{L,N}^\dagger c_{R,1} + c_{R,1}^\dagger c_{L,N}). \tag{1.34}$$

Now it can be shown that the Josephson current can be calculated as

$$I = 2e\frac{\partial \langle H_T \rangle}{\partial \phi}, \tag{1.35}$$

where $\phi = \phi_R - \phi_L$ is the difference of the complex phase of the superconducting order parameter between the right superconductor ϕ_R and the left superconductor ϕ_L. For a Josephson junction of trivial superconductors and in the absence of a magnetic field the Josephson current is thus given by

$$I = I_c \sin\phi, \tag{1.36}$$

which is proportional to the sine of the relative phase of the superconducting order parameters of the left and the right superconductors. I_c is the maximal (critical) current of the Josephson junction and depends mainly on the material of the superconductors and the junction's geometry.

The situation changes when both the left and the right superconductor are actually topological superconductors hosting Majorana zero modes on their ends, as shown in Figure 1.11b.

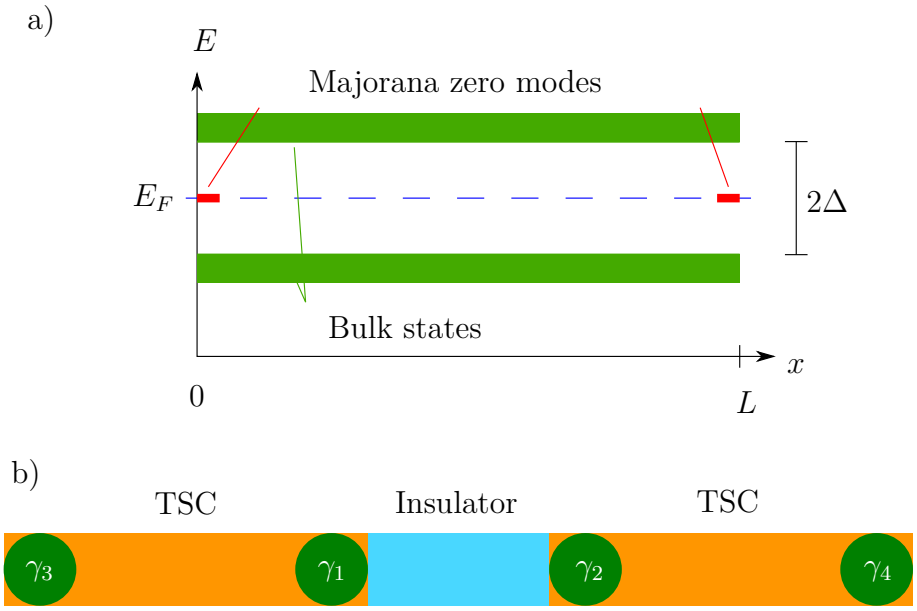

Figure 1.11: (a) Example bandstructure of a finite length one dimensional topological superconductor. At each end there is a single Majorana zero mode located exactly at Fermi level. (b) One dimensional Josephson junction constructed from two topological superconductors (TSC) and a regular insulator. Majorana zero modes (γ_i) are located at each end of each topological superconductor.

We will describe this situation in more detail following previous publications [7, 8], as this situation is somewhat unusual, highlights the special features of Majorana zero modes in Josephson junctions, and allows us to comment on real world ramifications. The tunneling Hamiltonian H_T can be adapted to the case of topological superconductors by formally replacing the conventional operators by Majorana operators,

$$c_j = \frac{\gamma_j + i\gamma_j'}{2} \tag{1.37}$$

$$c_j^\dagger = \frac{\gamma_j - i\gamma_j'}{2}. \tag{1.38}$$

Recalling that only one of the two Majorana operators constituting any regular fermion is a Majorana zero mode located at the edge, while the other is merged with the bulk, we can then rewrite the regular fermions in (1.34) for the low energy scenario as

$$c_{L,N} = \frac{1}{2}e^{\frac{i}{2}\phi_L}(\gamma_1 + i\gamma_1') \to \frac{1}{2}e^{\frac{i}{2}\phi_L}\gamma_1 \tag{1.39}$$

$$c_{R,1} = \frac{i}{2}e^{\frac{1}{2}\phi_R}(\gamma_2' + i\gamma_2) \to \frac{i}{2}e^{\frac{1}{2}\phi_R}\gamma_2. \tag{1.40}$$

This will then result in an effective tunneling Hamiltonian

$$H_{\text{eff}} = -\frac{t}{2}\cos\left(\frac{\phi}{2}\right) i\gamma_1\gamma_2 = \frac{t}{2}\cos\left(\frac{\phi}{2}\right)(2n-1). \tag{1.41}$$

Here n refers to the occupation of the Majorana zero modes which can either be present ($n = 1$) or absent ($n = 0$). It is crucial to note that in the low energy limit the occupation number n is conserved since

$$[H_{\text{eff}}, n] = 0. \tag{1.42}$$

This then results in DC Josephson current

$$I = 2e\frac{\partial\langle H_{\text{eff}}\rangle}{\partial\phi} = -\frac{te}{2}\sin\left(\frac{\phi}{2}\right)(2n-1). \tag{1.43}$$

This 4π periodic Josephson current mediated by Majorana zero modes originates from transporting half a Cooper pair (a single electron) across the junction and is therefore called fractional Josephson effect. The origin of this single electron transport can be easily understood. In a conventional superconductor-insulator-superconductor Josephson junction the bulk gap suppresses single electron tunneling. However, in the case of topological superconductors there are the Majorana zero modes within the bulk gap, mediating single electron tunneling.
The 4π periodicity of the Josephson current is more subtle, as the original Hamiltonian is 2π periodic. Looking at equation (1.41) we see that we actually have two distinct cases we need to distinguish. As shown in Figure 1.12a, when the system has a relative phase difference of $\phi = 0$ and the occupation of the Majorana modes $n = 1$, then the system is in the ground state of the effective Hamiltonian H_{eff} and has an energy of $E = -t/2$. When the relative phase of the superconductors is now advanced to $\phi = 2\pi$, then the energy of that state becomes $E = +t/2$. In this situation the other state with $n = 0$ actually has a lower energy of $E = -t/2$, but due to the conservation of n this state cannot be achieved when starting with $n = 1$. Advancing the phase by another 2π to $\phi = 4\pi$ brings the system back to its initial state. The periodicity of the ground state and the Josephson current is thus 4π, see Figure 1.12b. Measuring such a 4π periodic Josephson current has long been considered a smoking gun signature of Majorana zero modes [8], but newer theoretical studies suggest that other non-topological effects can also give rise to a 4π periodic Josephson [28]. In case it has been confirmed that a 4π periodic Josephson current indeed arises from the presence of Majorana zero modes, the Josephson current would provide a convenient tool for reading out the occupation number n, as any change in that number would reverse the direction of the current.
However, in reality there are various reasons why n does not need to be conserved. Stray

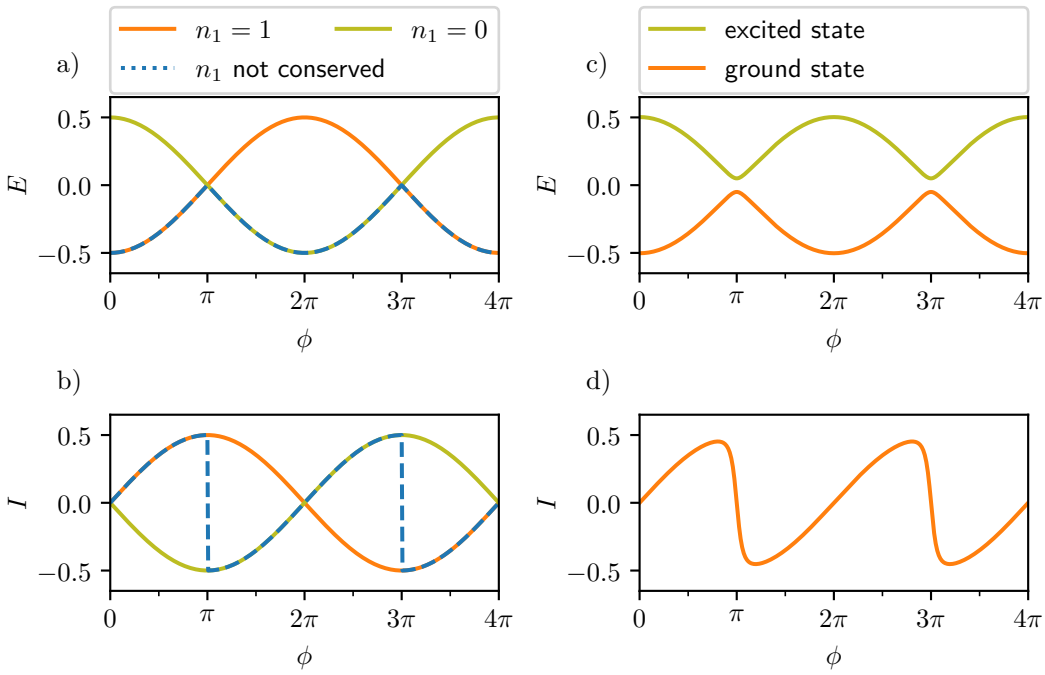

Figure 1.12: (a) Energy of the effective Hamiltonian H_{eff} in case of conserved occupation number n with the orange line representing $n = 1$, the yellow line representing $n = 0$ and the blue dashed line showing the ground state in case of non-conservation of n. (b) Corresponding Josephson currents. (c) Ground state (orange) end excited state (yellow) in the case of small hybridization. (d) Josephson current in the case of small hybridization.

quasiparticles from thermal excitations for example could switch n and bring the effective Hamiltonian H_{eff} back to the ground state. If the occupation number n were not to be conserved, then the system would change this occupation number at $\phi = (2l+1)\pi$, $l \in \mathbb{Z}$ such that it would always stay in the lowest energy state. This abrupt change of occupation number n would then result in a violent jump and a direction reversal of the Josephson current, as indicated in Figure 1.12b.

Another important reason why the occupation number n does not need to be conserved is hybridization with other Majorana zero modes. In the previous calculations it was assumed that only the Majorana zero modes γ_1 and γ_2 immediately adjacent to the insulator are involved and γ_3 and γ_4 are far away and thus isolated, see Figure 1.11b. This assumption is only approximately correct. In reality Majorana zero mode γ_3 will couple to γ_1 with a characteristic energy $\delta E \propto e^{-L/\xi}$, with L being the length of the superconductor and ξ the coherence length of the topological phase [8]. This issue can be overcome by changing the relative superconducting phase ϕ comparatively quickly, though this may be experimentally challenging, with having first to produce two sufficiently long one dimensional topological

superconductor, and then carefully controlling their phase.
Another difficulty for observing the 4π periodicity of the Majorana zero mode mediated Josephson current is that in general we would still observe the regular 2π periodic Josephson current and which could potentially be much larger in magnitude. However, more elaborate designs with an additional superconductor exist which would help to isolate the Majorana zero mode mediated contribution from the regular Josephson current occurring simultaneously [8].
As a last remark for finishing off this brief introduction to the physics of Josephson junctions, we would like to comment on the practicability of using Josephson junctions to irrefutably prove the existence of Majorana zero modes. For a long time it has been consensus that a 4π periodic Josephson current would be a hall mark of Majorana zero modes [8]. However, it has since been discovered that 4π periodic Josephson currents can also occur without Majorana zero modes [28]. It is henceforth only considered to be an indicator for the presence of Majorana zero modes, but no longer conclusive proof. The situation gets worse if only a heavily skewed 2π periodic Josephson current as shown in Figure 1.12d can be observed. In this case there are even more alternative explanations for this observation and further work to verify the origin of such observations would need to be performed. For example a quantum point contact instead of an insulator between the superconductors would show essentially the same skewed 2π periodic Josephson current [52]. Nonetheless, if neither a 4π periodic Josephson current nor a heavily skewed 2π Josephson current would be measured, then this would be, barring any experimental shortcomings, a very strong indication for the absence of Majorana zero modes.

1.5.1 Dirac Semimetal Josephson Junction

Having introduced Josephson junctions and how Majorana zero modes would give rise to either a 4π periodic Josephson current or a heavily skewed 2π periodic Josephson current, we can now focus on how Majorana zero modes manifest themselves in a Josephson junction over a Dirac semimetal. This concept has been proposed a couple of years ago for a time reversal symmetric Weyl semimetal [12]. Due to not depending on the broken inversion symmetry of the originally investigated Weyl semimetal, the argument carries over to Dirac semimetals, for which the authors have supported their claims by numerical calculations, though experimental confirmation of the findings is still outstanding [13].
A Dirac semimetal is a so called gapless topological material, similar to a Weyl semimetal. It has an insulating bulk band gap with an even number of Dirac nodes, band touching points at Fermi level. While Weyl semimetals are either time reversal symmetric or inversion symmetric, Dirac semimetals are simultaneously both, time reversal symmetric and inversion symmetric, leading to a degeneracy of all bands, the so called Kramer's degeneracy. As a consequence,

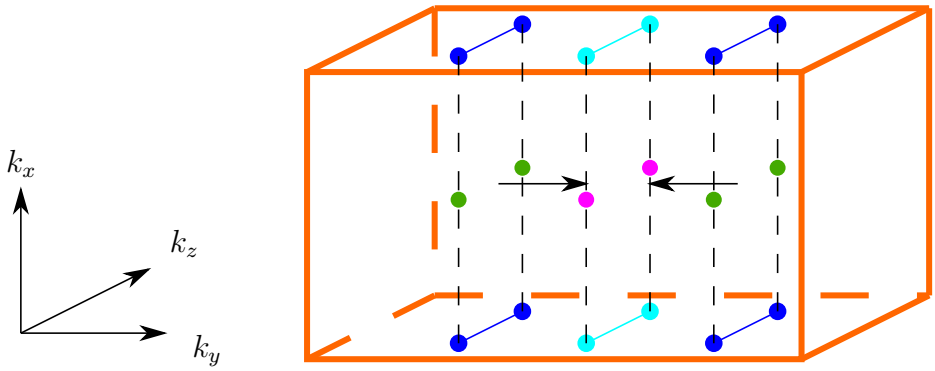

Figure 1.13: Symbolic representation of a time reversal symmetric Weyl semimetal and a Dirac semimetal. In green are shown the Weyl nodes of a time reversal symmetric Weyl semimetal, with the blue dots indicating their projections on the k_y-k_z-surface. On the surface the projection of the Weyl nodes are connected by Fermi arcs, as indicated by the solid blue lines. A Dirac semimetal with a minimum of 2 Dirac nodes (shown in magenta) can be understood as a Weyl semimetal with two Weyl nodes coinciding at each Dirac node. Surface projections and surface Fermi arc of the Dirac semimetal is shown by the cyan dots and lines, respectively.

the Dirac nodes are inherently unstable and need to be stabilized by crystal symmetries [53]. The most interesting features of Weyl and Dirac semimetals are their surface states, which are surface Fermi arcs and not closed Fermi surfaces. Those Fermi arcs are connecting the projections of the Weyl/Dirac nodes, as shown in Figure 1.13. An advantage of using Dirac semimetals over Weyl semimetals is the availability in real materials. While there are well known Dirac semimetals such as Na_3Bi and Cd_3As_2 with the minimal number of two Dirac nodes, the situation is different for time reversal symmetric Weyl semimetals. There are known Weyl semimetals with 24 Weyl nodes, but cases with the minimal number of only 4 Weyl nodes remain an active topic of research [54, 55].

In the following we will give a short reproduction of earlier work on how Majorana zero modes can develop in Weyl semimetal–superconductor junctions [12]. Weyl semimetals can host Majorana zero modes along their surface when brought into contact with a superconductor. The resulting Fermi arc surface states can be considered in isolation, as they are well separated from the bulk, except near the projection of the Weyl nodes. An effective two dimensional surface Hamiltonian can therefore be given by

$$H = \sum_{k_y,k_z} B^\dagger_{k_y,k_z} \mathcal{H}_{\mathrm{BdG}}(k_y,k_z) B_{k_y,k_z}, \tag{1.44}$$

with

$$B^\dagger_{k_y,k_z} = (b^\dagger_{k_y,k_z,\uparrow}, b^\dagger_{k_y,k_z,\downarrow}, b_{-k_y,-k_z,\uparrow}, -b_{-k_y,-k_z,\downarrow}) \tag{1.45}$$

and

$$\mathcal{H}_{\mathrm{BdG}}(k_y, k_z) = (v\sigma_z k_y - \tilde{\mu})\tau_z + \mathrm{re}\Delta\tau_x - \mathrm{im}\Delta\tau_y, \quad \mathrm{for}|k_z| < k_D \tag{1.46}$$

Here, σ_i, τ_i denote Pauli matrices in spin space and particle-hole space, respectively. Δ is the induced Cooper pair amplitude stemming from the adjacent superconductor, $\tilde{\mu} = \mu + \eta$ is a modified chemical potential μ, η is a parameter describing the separation between the two Fermi arcs. The Fermi arcs originate at the projections of the Weyl nodes onto the surface, thus ranging between $(k_y, k_z) = (0, \pm k_D)$. v is the Fermi velocity. In the case of a Dirac semimetal $\eta = 0$ and the two Fermi arcs would coincide, as explained above. Here it is important to note that this model is only valid if

$$v\big||k_z| - k_D\big| > \Delta, \tag{1.47}$$

i.e. away from the surface projections of the Weyl nodes, because otherwise the bulk bands, which reach Fermi level at the Weyl nodes, become important and the simple model breaks down. The topological nature of the system can be inferred from its similarity to the edge of a two dimensional topological insulator in contact with a superconductor [56]. For each permitted value k_z the Hamiltonian (1.46) matches that of the two dimensional topological insulator. The Weyl semimetal (or rather its edge states) can thus be thought of a stack of two dimensional topological insulators. However, unlike in the two dimensional topological insulator case, breaking the time reversal symmetry of the surface states of the Weyl semimetal will not generically open a gap. Instead, a gap can be opened by creating a domain wall in the order parameter $\Delta(y)$, in a geometry shown in Figure 1.14.

For each k_z along the Fermi arc permitted by (1.47) this will result in an exact Jackiw-Rossi zero mode

$$\psi_s(y) = A \begin{pmatrix} i \\ s \end{pmatrix} \exp\left\{ -\frac{1}{v} \int_0^y dy' \left[\Delta(y') - is\tilde{\mu}\right] \right\}, \tag{1.48}$$

where $s = \pm 1$ [57]. This zero mode is strongly localized near the junction. Hereby it is not important how the superconducting order parameter $\Delta(y)$ changes, as long as it is real and has the correct limit $\lim_{y\to\pm\infty} \Delta(y) = \pm\Delta_0$. The strong localization of this zero mode is shown in Figure 1.15 for the simple but unphysical case of adjacent superconductors with opposite superconducting order parameter $\Delta(y)$, and for the more realistic case with a gap in between these two superconductors, similar to the situation shown in Figure 1.14. In both cases we can see a strong localization of the zero mode in between the superconductors, with only an exponential decay into the superconducting region. As a final remark it shall be pointed out that there is a crucial difference from the Weyl/Dirac semimetal–superconductor system to the stacked two dimensional topological insulator–superconductor model: In a single two dimensional topological insulator–superconductor system the occupation of the Majorana

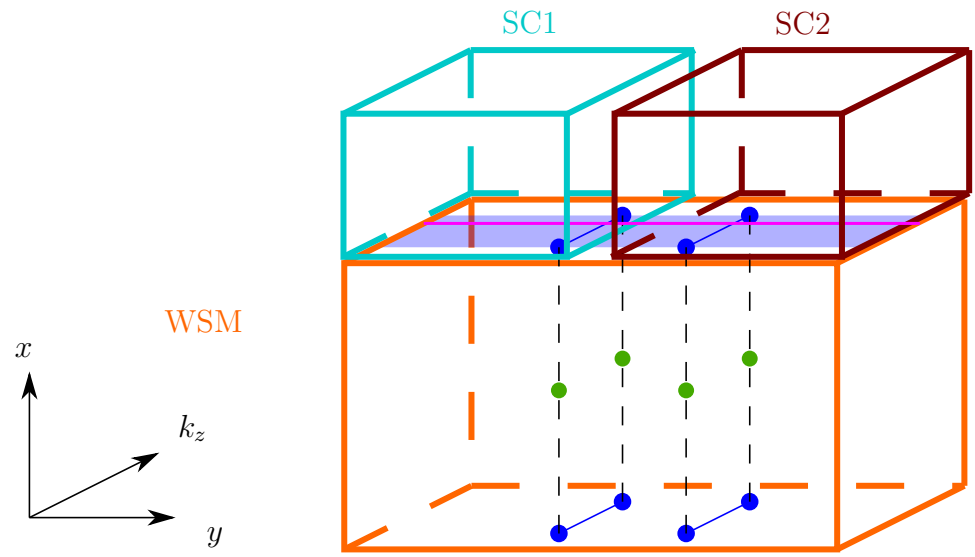

Figure 1.14: Weyl semimetal with two superconductors coupled on top via superconducting proximity effect. The Fermi arc in momentum space is no longer present as an arc due to the system being transformed into real space in x- and y-directions. Instead it is now indicated by the blue shaded band. Indicated by the magenta line is a one dimensional cut for a fixed k_z value, where a pair of Majorana zero modes is present.

zero modes is protected by fermion parity, resulting in a 4π periodic Josephson current under the restrictions mentioned before. This, however, does not hold true for the Weyl/Dirac semimetal–superconductor system. Here, Majorana zero modes located at different k_z values can simultaneously occupied by a splitting Cooper pair, removing the parity protection of the occupation number. It can thus only be expected to see a highly skewed jump of the Josephson current when such change of occupation number occurs.

1.6 Purpose and Outline

The goal of this work is to further investigate two popular proposals of creating Majorana zero modes in condensed matter systems and gain further insight and guidance for optimizing those approaches and experimentally realizing and unambiguously identify Majorana zero modes.
The first system we are going to analyze is the induced topological superconductor in a topological insulator–superconductor system. While the theory of the physics at the interface between topological insulator and superconductor has been well understood and the ARPES experiment showing the Dirac cone at the surface of the superconductor is a highly interesting result, there are still lots of questions how theory of the Fu-Kane model and experiment are

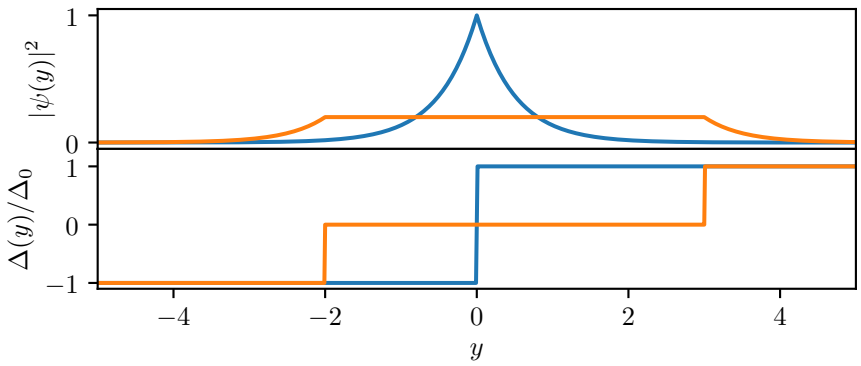

Figure 1.15: Jackiw-Rossi zero mode for directly adjacent superconductors with opposite superconducting order parameter $\Delta(y)$ (blue) and for superconductors separated by a gap (orange). Upper graph shows the spacial localization of the Jackiw-Rossi zero mode, lower graph shows the spacial localization of the order parameter.

related [9, 11]. It seems plausible that both the Fu-Kane model, which only deals with the interface and incorporates the superconductor only via superconducting proximity effect, and the experiment describe the same topological phase. However, the relation between theory and experiment is not quite clear and it is entirely possible that they do actually correspond to different topological phases. We will thus investigate the topological insulator–superconductors system with a tight-binding model and thereby establish the connection between the Fu-Kane model and the recent experiment, showing that they both indeed belong to the same topological phase. At the same time we will use our model to analyze which conditions enhance experimental observability of the Dirac nodes from the topological insulator at the free surface of the superconductor. This can be useful for future experimental observations of Dirac cones in different material combinations of topological insulator and superconductor. Furthermore, we will show how magnetic doping will induce a differently gapped phase. In agreement with the Fu-Kane model, our calculations show that there is a single band closing when changing from the superconductivity gapped regime to the ferromagnetically gapped regime, indicating a topological phase transition. At this phase transition Majorana zero modes are predicted [9], though additional calculations are required to irrefutably confirm the existence of Majorana zero modes in the present model.

The second system we are investigating is a Josephson junction on a Dirac semimetal. This system has been proposed to host Majorana zero modes which would manifest themselves in a skewed Josephson current [12] and numerical analysis supports this for a simplified version of a lattice model of the Dirac semimetal Cd_3As_2 [13]. We are exploring how the system behavior changes when the system geometry is changed to a more experimentally accessible one, when

the Dirac semimetal is exchanged for the similar Na_3Bi, how different model parameters affect the Josephson current and what conclusions can be drawn from this.
The work is outlined as follows: In chapter 2 we will introduce all the models and methods that we use, including the tight-binding Andreev reflection method that we have developed. In chapter 3 we will present the results of our investigations and finally draw conclusions and suggestions for further research in chapter 4.

2 Methods and Models

In this chapter we shall introduce the specific models which we use to investigate the topological insulator–superconductor system as well as the Dirac semimetal Josephson junction. We shall also introduce the appropriate methods for investigating these systems. First we will introduce the mean-field approach to Andreev reflection we have developed and which can be used to describe the topological insulator–superconductor as well as the Dirac semimetal Josephson junction more accurately. Afterwards we will introduce our model of the topological insulator–superconductor system and argue why for our purposes it is not required to include all of the elaborate details of the Andreev reflection which we have just worked out. In the last part of this chapter we will explain the Dirac semimetal Josephson junction and the challenges unique to this system.

2.1 Mean-Field Approach to Andreev Reflection

It is inherently difficult to accurately describe Andreev reflection in a tight-binding model, as explained in section 1.3. The wave matching approach is by its very nature unsuited for tight-binding models and the tunneling Hamiltonian approach has difficulties describing the spatial evolution of the Cooper pair pairing amplitude. While it would be possible to calculate the pairing potential within the superconductor by reformulating the Hamiltonian (1.1) in real space and then calculate the pairing potential self-consistently, this approach cannot be used within the normal metal, as there is no pairing potential, but only a pair amplitude being induced by the superconductor [43]. Hence a different approach is needed.
In order to overcome the limitations of both the wave matching approach and the tunneling approach we will introduce an interaction term which describes Andreev reflection more faithfully. For simplicity, we will assume that the Andreev reflection happens only exactly at the interface between metal and superconductor. This can then be straight forwardly extended to a more realistic setup where the interaction happens within a finite distance from the interface, as we shall discuss later on in subsection 2.1.4.

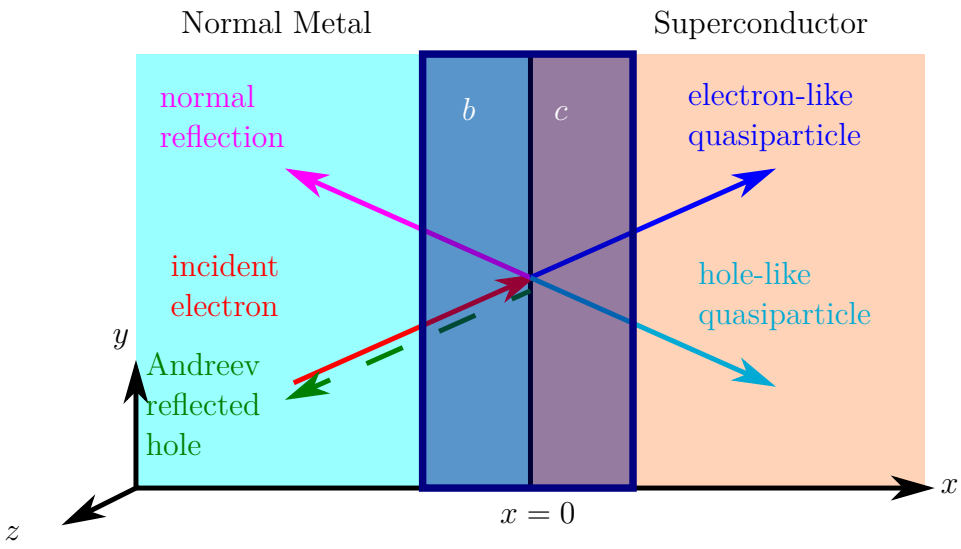

Figure 2.1: Normal metal – superconductor junction. The junction is modeled by one unit cell of the normal metal and one unit cell of the superconductor on the sides of the junction in x-direction. y- and z-directions are assumed to be infinite. Electronic creation/annihilation operators are denoted by b on the normal metal side of the junction, and by c on the superconductor side.

2.1.1 Hamiltonians

Our prototypical system consists of a generic normal metal H_{NM}, a generic superconductor H_{SC} and an interaction term H_{int}, which describes the Andreev reflection at the interface between the normal metal and the superconductor. H_{NM} and H_{SC} by themselves are independent and non-interacting and are therefore combined into H_0,

$$H_{\mathrm{tot}} = H_{\mathrm{NM}} + H_{\mathrm{SC}} + H_{\mathrm{int}} = H_0 + H_{\mathrm{int}}. \tag{2.1}$$

It shall be stressed that H_{int} is not a mere tunneling term, but a real interaction term describing the Andreev Reflection as explained in subsection 1.3.1. In order to avoid confusion, we will denote all electronic creation (annihilation) operators in the normal metal by b ($b^\dagger$) and in the superconductor by c ($c^\dagger$). The system is assumed to be extended infinitely in y- and z-directions, but finite in x-direction. We will therefore describe the y- and z-directions in momentum space, denoted by $\mathbf{k} = (k_y, k_z)$. Furthermore, we will restrict ourselves to a single unit cell of the normal metal/superconductor on either side of the interface, as indicated in Figure 2.1. We will later explain how this can be extended to an interaction within multiple unit cells of the interface.

For the normal metal part H_{NM} of the Hamiltonian we choose a simple generic non-magnetic metal. The exact form does not play any role in the calculations and it is only given for

illustrative purposes, as it will simplify visualizing later how the metal part gets coupled to the superconducting part. It is given in the form of a BdG Hamiltonian as

$$H_{\mathrm{NM}} = \frac{1}{2}\sum_{\mathbf{k}} \begin{pmatrix} b^\dagger_{\mathbf{k}\uparrow}, & b^\dagger_{\mathbf{k}\downarrow}, & b_{-\mathbf{k}\uparrow}, & b_{-\mathbf{k}\downarrow} \end{pmatrix} \mathcal{H}_{\mathrm{NM}}(\mathbf{k}) \begin{pmatrix} b_{\mathbf{k}\uparrow} \\ b_{\mathbf{k}\downarrow} \\ b^\dagger_{-\mathbf{k}\uparrow} \\ b^\dagger_{-\mathbf{k}\downarrow} \end{pmatrix}, \tag{2.2}$$

where

$$\mathcal{H}_{\mathrm{NM}}(\mathbf{k}) = \begin{pmatrix} f(\mathbf{k}) & & & \\ & f(\mathbf{k}) & & \\ & & -f^*(-\mathbf{k}) & \\ & & & -f^*(-\mathbf{k}) \end{pmatrix}. \tag{2.3}$$

The function $f(\mathbf{k})$ does not have a special meaning and is simply representative for the internal structure of the metal, for example nearest neighbor hopping, and would in general depend on the specific properties of the metal.
Similarly, we use a very simple construction for the superconducting part, in order not to clutter our notation and distract from the interesting physics happening due to the interaction. The Hamiltonian is thus given by

$$H_{\mathrm{SC}} = \frac{1}{2}\sum_{\mathbf{k}} \begin{pmatrix} c^\dagger_{\mathbf{k}\uparrow}, & c^\dagger_{\mathbf{k}\downarrow}, & c_{-\mathbf{k}\uparrow}, & c_{-\mathbf{k}\downarrow} \end{pmatrix} \mathcal{H}_{\mathrm{SC}}(\mathbf{k}) \begin{pmatrix} c_{\mathbf{k}\uparrow} \\ c_{\mathbf{k}\downarrow} \\ c^\dagger_{-\mathbf{k}\uparrow} \\ c^\dagger_{-\mathbf{k}\downarrow} \end{pmatrix}, \tag{2.4}$$

with

$$\mathcal{H}_{\mathrm{SC}}(\mathbf{k}) = \begin{pmatrix} g(\mathbf{k}) & & & \Delta^* \\ & g(\mathbf{k}) & -\Delta^* & \\ & -\Delta & -g^*(-\mathbf{k}) & \\ \Delta & & & -g^*(-\mathbf{k}) \end{pmatrix}. \tag{2.5}$$

Here again, $g(\mathbf{k})$ does not have any deeper meaning and the superconducting order parameter Δ is assumed to be independent of the momentum $\mathbf{k}$, for simplicity.
We can now write down the entire non-interacting part of the system and also introduce some new notation, which will aid us later in understanding the effects of the interaction. The

non-interaction Hamiltonian will thus be written as

$$H_0 = \frac{1}{2}\sum_{\mathbf{k}} A_{\mathbf{k}}^\dagger \mathcal{H}_0(\mathbf{k}) A_{\mathbf{k}}, \tag{2.6}$$

where

$$A_{\mathbf{k}}^\dagger = \left(b_{\mathbf{k}\uparrow}^\dagger, b_{\mathbf{k}\downarrow}^\dagger, b_{-\mathbf{k}\uparrow}, b_{-\mathbf{k}\downarrow}, c_{\mathbf{k}\uparrow}^\dagger, c_{\mathbf{k}\downarrow}^\dagger, c_{-\mathbf{k}\uparrow}, c_{-\mathbf{k}\downarrow}\right) \tag{2.7}$$

and

$$\mathcal{H}_0(\mathbf{k}) = \begin{array}{c} \\ b_{\mathbf{k}\uparrow}^\dagger \\ b_{\mathbf{k}\downarrow}^\dagger \\ b_{-\mathbf{k}\uparrow} \\ b_{-\mathbf{k}\downarrow} \\ c_{\mathbf{k}\uparrow}^\dagger \\ c_{\mathbf{k}\downarrow}^\dagger \\ c_{-\mathbf{k}\uparrow} \\ c_{-\mathbf{k}\downarrow} \end{array} \begin{array}{c} \begin{array}{cccc} b_{\mathbf{k}\uparrow} & b_{\mathbf{k}\downarrow} & b_{-\mathbf{k}\uparrow}^\dagger & b_{-\mathbf{k}\downarrow}^\dagger \end{array} \\ \left(\begin{array}{cccc:cccc} f(\mathbf{k}) & & & & & & & \\ & f(\mathbf{k}) & & & & & & \\ & & -f^*(-\mathbf{k}) & & & & & \\ & & & -f^*(-\mathbf{k}) & & & & \\ \hdashline & & & & g(\mathbf{k}) & & & \Delta \\ & & & & & g(\mathbf{k}) & -\Delta & \\ & & & & & -\Delta^* & -g^*(-\mathbf{k}) & \\ & & & & \Delta^* & & & -g^*(-\mathbf{k}) \end{array}\right) \end{array} \begin{array}{c} \\ c_{\mathbf{k}\uparrow} \\ c_{\mathbf{k}\downarrow} \\ c_{-\mathbf{k}\uparrow}^\dagger \\ c_{-\mathbf{k}\downarrow}^\dagger \end{array}. \tag{2.8}$$

Here the operators b and c are obviously not part of the matrix $\mathcal{H}_0(\mathbf{k})$, but instead are printed as a help to quickly see which operators are coupled by which entries of the matrix. From this representation it is immediately clear that without interaction term the system behaves as two completely separate systems of normal metal and superconductor. We shall next focus on the interaction term and incorporate it into the total Hamiltonian, so that we can clearly and easily see the effects of the interaction.

2.1.2 Interaction Hamiltonian

Having established the background and notation, it is now time to turn to the interaction term itself. From the phenomenological description above we know that we need to annihilate an electron in the metal, create a hole in the metal and create two electron-like Bogoliubov quasiparticles in the superconductor. The Hamiltonian can thus be written as

$$H_{\text{int}} = \sum_{\mathbf{k}}\sum_{\sigma} W_{\mathbf{k}} b_{-\mathbf{k}\bar{\sigma}} b_{\mathbf{k}\sigma} \gamma_{e,\mathbf{k}\sigma}^\dagger \gamma_{e,-\mathbf{k}\bar{\sigma}}^\dagger + \text{h.c.}, \tag{2.9}$$

where $W_{\mathbf{k}}$ is a prefactor which modulates the Andreev reflection due to previously unconsidered factors such as spin texture, which is known to make the Andreev reflection dependent on the

angle under which the incident electron hits the interface [58]. An extreme example would be a fully spin polarized normal metal instead of our well behaved generic normal metal. In this case Andreev reflection is totally suppressed and we would get a prefactor $W_{\mathbf{k}} = 0$, effectively disabling Andreev reflection in the model [40, 59].

We would like to point out that we have implicitly made the common assumption that the Andreev reflected hole will have exactly opposite momentum to the incident electron, even though this is only true if the incoming electron is exactly at Fermi level [39, 40, 60]. This is akin to the usual assumption that Cooper pairs in a conventional superconductor consist of two electrons with exactly opposite momentum, even though we know that this is only approximately true [33].

Next, in order to use our regular machinery for dealing with tight-binding models, we need to convert the Bogoliubov quasiparticle operators to regular electron operators which our model is based on. For this we simply need to replace the Bogoliubov quasiparticle operators in (2.9) with their definitions from table 1.1

$$\begin{aligned} H_{\text{int}} &= \sum_{\mathbf{k}} \sum_{\sigma} W_{\mathbf{k}} b_{-\mathbf{k}\bar{\sigma}} b_{\mathbf{k}\sigma} (u_{\mathbf{k}}^* c_{\mathbf{k}\sigma}^\dagger - v_{\mathbf{k}}^* S^\dagger c_{-\mathbf{k}\bar{\sigma}})(v_{\mathbf{k}}^* S^\dagger c_{\mathbf{k}\sigma} + u_{\mathbf{k}}^* c_{-\mathbf{k}\bar{\sigma}}^\dagger) + \text{h.c.} \\ &= \sum_{\mathbf{k}} \sum_{\sigma} W_{\mathbf{k}} b_{-\mathbf{k}\bar{\sigma}} b_{\mathbf{k}\sigma} \Big[u_{\mathbf{k}}^* v_{\mathbf{k}}^* c_{\mathbf{k}\sigma}^\dagger S^\dagger c_{\mathbf{k}\sigma} + u_{\mathbf{k}}^* u_{\mathbf{k}}^* c_{\mathbf{k}\sigma}^\dagger c_{-\mathbf{k}\bar{\sigma}}^\dagger \\ &\quad - v_{\mathbf{k}}^* v_{\mathbf{k}}^* S^\dagger c_{-\mathbf{k}\bar{\sigma}} S^\dagger c_{\mathbf{k}\sigma} - v_{\mathbf{k}}^* u_{\mathbf{k}}^* S^\dagger c_{-\mathbf{k}\bar{\sigma}} c_{-\mathbf{k}\bar{\sigma}}^\dagger \Big] + \text{h.c.} \\ &= \sum_{\mathbf{k}} \sum_{\sigma} W_{\mathbf{k}} \left[u_{\mathbf{k}}^{*\,2} - v_{\mathbf{k}}^{*2} \right] b_{-\mathbf{k}\bar{\sigma}} b_{\mathbf{k}\sigma} c_{\mathbf{k}\sigma}^\dagger c_{-\mathbf{k}\bar{\sigma}}^\dagger + \text{h.c.}. \end{aligned} \tag{2.10}$$

This can be further simplified when taking into account previous conditions on the coherence factors $u_{\mathbf{k}}$ and $v_{\mathbf{k}}$ (1.10)-(1.15). We will find that the prefactor can be written as

$$u_{\mathbf{k}}^{*\,2} - v_{\mathbf{k}}^{*2} = \frac{1}{2\sqrt{\xi_{\mathbf{k}}^2 + |\Delta_{\mathbf{k}}|^2}} \left[\sqrt{\xi_{\mathbf{k}}^2 + |\Delta_{\mathbf{k}}|^2} \left(1 - e^{-2i\phi_{\mathbf{k}}}\right) + \xi_{\mathbf{k}}^2 \left(1 + e^{-2i\phi_{\mathbf{k}}}\right) \right], \tag{2.11}$$

where $\phi_{\mathbf{k}}$ describes the phase of the superconducting order parameters $\Delta_{\mathbf{k}}$, as previously defined in (1.10). Note that in the limit of vanishing superconductivity $\Delta_{\mathbf{k}} \to 0$ this term will simply be unity, as could be expected for two normal metals.

In the following it will not be necessary to explicitly deal with the coherence factors, so we can conveniently absorb them into the already present prefactor as

$$\tilde{W}_{\mathbf{k}} := W_{\mathbf{k}} (u_{\mathbf{k}}^{*\,2} - v_{\mathbf{k}}^{*2}). \tag{2.12}$$

We can then write the interaction Hamiltonian as

$$H_{\text{int}} = \sum_{\mathbf{k}} \sum_{\sigma} \tilde{W}_{\mathbf{k}} b_{-\mathbf{k}\bar{\sigma}} b_{\mathbf{k}\sigma} c^{\dagger}_{\mathbf{k}\sigma} c^{\dagger}_{-\mathbf{k}\bar{\sigma}} + \tilde{W}^{*}_{\mathbf{k}} c_{-\mathbf{k}\bar{\sigma}} c_{\mathbf{k}\sigma} b^{\dagger}_{\mathbf{k}\sigma} b^{\dagger}_{-\mathbf{k}\bar{\sigma}}. \tag{2.13}$$

Looking closely at the interaction Hamiltonian (2.13), we observe that we would have almost reached the same result if we would have started with electron operators c instead of Bogoliubov quasiparticle operators γ in equation (2.9). The only difference would have been in the prefactor $\tilde{W}_{\mathbf{k}}$. Having taken into account the nature of the Bogoliubov quasiparticles within the superconductor, we have found the interaction Hamiltonian to be dependent on the superconducting order parameter $\Delta_{\mathbf{k}}$, as could be expected.

2.1.3 Mean-Field Decoupling of Andreev Interaction

The interaction term of the Andreev reflection (2.13) is quartic in operators and as such inherently difficult to treat. A common and often successful approach to this kind of problem is to treat the interaction Hamiltonian with a mean-field approach. There are two different channels for decoupling the interaction which should be considered here: First is the direct or density channel, which would lead to effective single electron hopping between normal metal and superconductor. Second would be the Cooper channel, which would lead to the presence of Cooper pairs in the normal metal. The exchange channel can be excluded, as we do not consider any magnetic impurities at the interface, which could account for the required spin flip. We will first discuss the mean-field decoupling separately in the direct and the Cooper channels and then give a formulation of a unified approach treating both channels simultaneously.

Direct Channel

Decoupling the interaction Hamiltonian (2.13) in the direct channel is a straight forward exercise covered in many textbooks and will therefore not be reproduced in detail here. However, for the reader's convenience, let us quickly show which operators are grouped together in the mean-field decoupling in the direct channel

$$H_{\text{int}} = \sum_{\mathbf{k}} \sum_{\sigma} \tilde{W}_{\mathbf{k}} \overbrace{b_{-\mathbf{k}\bar{\sigma}} \overbrace{b_{\mathbf{k}\sigma} c^{\dagger}_{\mathbf{k}\sigma}}^{} c^{\dagger}_{-\mathbf{k}\bar{\sigma}}}^{} + \tilde{W}^{*}_{\mathbf{k}} \overbrace{c_{-\mathbf{k}\bar{\sigma}} \overbrace{c_{\mathbf{k}\sigma} b^{\dagger}_{\mathbf{k}\sigma}}^{} b^{\dagger}_{-\mathbf{k}\bar{\sigma}}}^{}. \tag{2.14}$$

The mean-field decoupling then results in a mean-field Hamiltonian of the form

$$H_{\text{int,MF,direct}} = \sum_{\mathbf{k}} \sum_{\sigma} \tilde{W}_{\mathbf{k}} \Big[b_{\mathbf{k}\sigma} c^{\dagger}_{\mathbf{k}\sigma} \langle b_{-\mathbf{k}\bar{\sigma}} c^{\dagger}_{-\mathbf{k}\bar{\sigma}} \rangle + b_{-\mathbf{k}\bar{\sigma}} c^{\dagger}_{-\mathbf{k}\bar{\sigma}} \underbrace{\langle b_{\mathbf{k}\sigma} c^{\dagger}_{\mathbf{k}\sigma} \rangle}_{=:\Gamma_{\mathbf{k}\sigma}} \Big] + \tilde{W}^{*}_{\mathbf{k}} \Big[c_{\mathbf{k}\sigma} b^{\dagger}_{\mathbf{k}\sigma} \langle c_{-\mathbf{k}\bar{\sigma}} b^{\dagger}_{-\mathbf{k}\bar{\sigma}} \rangle + c_{-\mathbf{k}\bar{\sigma}} b^{\dagger}_{-\mathbf{k}\bar{\sigma}} \langle c_{\mathbf{k}\sigma} b^{\dagger}_{\mathbf{k}\sigma} \rangle \Big] + \text{const.} \tag{2.15}$$

The constant stems from the process of the mean-field decoupling but does not change the band structure besides a constant shift and will thus henceforth be ignored.
Looking at the mean-field Hamiltonian decoupled in the direct channel, we see an effective single electron coupling between normal metal and superconductor, which is dependent on the superconducting order parameter Δ by the virtue of the modified prefactor $\tilde{W}_{\mathbf{k}}$. This becomes even more apparent if we write the entire resulting Hamiltonian

$$H_{\text{MF,direct}} = \frac{1}{2} \sum_{\mathbf{k}} A^{\dagger}_{\mathbf{k}} \mathcal{H}_{\text{MF,direct}}(\mathbf{k}) A_{\mathbf{k}}, \tag{2.16}$$

with $A^{\dagger}_{\mathbf{k}}$ as given in (2.7) and

$$\mathcal{H}_{\text{MF,direct}}(\mathbf{k}) = \mathcal{H}_0(\mathbf{k}) + \mathcal{H}_{\text{int,MF,direct}}(\mathbf{k})$$

$$= \begin{array}{c} \\ b^{\dagger}_{\mathbf{k}\uparrow} \\ b^{\dagger}_{\mathbf{k}\downarrow} \\ b_{-\mathbf{k}\uparrow} \\ b_{-\mathbf{k}\downarrow} \\ \hdashline c^{\dagger}_{\mathbf{k}\uparrow} \\ c^{\dagger}_{\mathbf{k}\downarrow} \\ c_{-\mathbf{k}\uparrow} \\ c_{-\mathbf{k}\downarrow} \end{array} \left(\begin{array}{cccc:cccc} b_{\mathbf{k}\uparrow} & b_{\mathbf{k}\downarrow} & b^{\dagger}_{-\mathbf{k}\uparrow} & b^{\dagger}_{-\mathbf{k}\downarrow} & & & & \\ f(\mathbf{k}) & & & & & & & \\ & f(\mathbf{k}) & & & & & & \\ & & -f^{*}(-\mathbf{k}) & & & & & \\ & & & -f^{*}(-\mathbf{k}) & & & & \\ \hdashline & & & & -2\Gamma_{-\mathbf{k}\downarrow}\tilde{W}_{\mathbf{k}} & & & \\ & & & & & -2\Gamma_{-\mathbf{k}\uparrow}\tilde{W}_{\mathbf{k}} & & \\ & & & & & & 2\Gamma^{*}_{\mathbf{k}\downarrow}\tilde{W}^{*}_{\mathbf{k}} & \\ & & & & & & & 2\Gamma^{*}_{\mathbf{k}\uparrow}\tilde{W}^{*}_{\mathbf{k}} \end{array} \right)$$

$$\left(\begin{array}{cccc:cccc} -2\Gamma^{*}_{-\mathbf{k}\downarrow}\tilde{W}^{*}_{\mathbf{k}} & & & & & & & \\ & -2\Gamma^{*}_{-\mathbf{k}\uparrow}\tilde{W}^{*}_{\mathbf{k}} & & & & & & \\ & & 2\Gamma_{\mathbf{k}\downarrow}\tilde{W}_{\mathbf{k}} & & & & & \\ & & & 2\Gamma_{\mathbf{k}\uparrow}\tilde{W}_{\mathbf{k}} & & & & \\ \hdashline & & & & g(\mathbf{k}) & & & \Delta \\ & & & & & g(\mathbf{k}) & -\Delta & \\ & & & & & -\Delta^{*} & -g^{*}(-\mathbf{k}) & \\ & & & & \Delta^{*} & & & -g^{*}(-\mathbf{k}) \end{array} \right) \begin{array}{c} b^{\dagger}_{\mathbf{k}\uparrow} \\ b^{\dagger}_{\mathbf{k}\downarrow} \\ b_{-\mathbf{k}\uparrow} \\ b_{-\mathbf{k}\downarrow} \\ \hdashline c^{\dagger}_{\mathbf{k}\uparrow} \\ c^{\dagger}_{\mathbf{k}\downarrow} \\ c_{-\mathbf{k}\uparrow} \\ c_{-\mathbf{k}\downarrow} \end{array} \tag{2.17}$$

$$\begin{array}{cccc} c_{\mathbf{k}\uparrow} & c_{\mathbf{k}\downarrow} & c^{\dagger}_{-\mathbf{k}\uparrow} & c^{\dagger}_{-\mathbf{k}\downarrow} \end{array}$$

This notation clearly shows how the mean-field decoupling in the direct channel connects the

normal metal and the superconductor together in a fashion very similar to how a tunneling Hamiltonian would connect the two systems.

Cooper Channel

As mentioned before, the direct channel is not the only viable channel for a mean-field treatment and we will thus have a look at what happens when we choose to decouple the interaction in the Cooper channel instead. We again start with our interaction Hamiltonian

$$H_{\text{int}} = \sum_{\mathbf{k}} \sum_{\sigma} \tilde{W}_{\mathbf{k}} \overbrace{b_{-\mathbf{k}\bar{\sigma}} b_{\mathbf{k}\sigma}} \overbrace{c^{\dagger}_{\mathbf{k}\sigma} c^{\dagger}_{-\mathbf{k}\bar{\sigma}}} + \tilde{W}^{*}_{\mathbf{k}} \overbrace{c_{-\mathbf{k}\bar{\sigma}} c_{\mathbf{k}\sigma}} \overbrace{b^{\dagger}_{\mathbf{k}\sigma} b^{\dagger}_{-\mathbf{k}\bar{\sigma}}}, \tag{2.18}$$

only this time we group the operators differently than in (2.14). The mean-field decoupling in the Cooper channel results in a mean-field Hamiltonian of the form

$$\begin{aligned} H_{\text{int,MF,Cooper}} = \sum_{\mathbf{k}} \sum_{\sigma} \tilde{W}_{\mathbf{k}} \Big[b_{-\mathbf{k}\bar{\sigma}} b_{\mathbf{k}\sigma} \langle c^{\dagger}_{\mathbf{k}\sigma} c^{\dagger}_{-\mathbf{k}\bar{\sigma}} \rangle + c^{\dagger}_{\mathbf{k}\sigma} c^{\dagger}_{-\mathbf{k}\bar{\sigma}} \underbrace{\langle b_{-\mathbf{k}\bar{\sigma}} b_{\mathbf{k}\sigma} \rangle}_{=:\bar{\Delta}_{\mathbf{k}\sigma}} \Big] \\ + \tilde{W}^{*}_{\mathbf{k}} \Big[c_{-\mathbf{k}\bar{\sigma}} c_{\mathbf{k}\sigma} \langle b^{\dagger}_{\mathbf{k}\sigma} b^{\dagger}_{-\mathbf{k}\bar{\sigma}} \rangle + b^{\dagger}_{\mathbf{k}\sigma} b^{\dagger}_{-\mathbf{k}\bar{\sigma}} \underbrace{\langle c_{-\mathbf{k}\bar{\sigma}} c_{\mathbf{k}\sigma} \rangle}_{=:\bar{\Delta}_{\mathbf{k}\sigma}} \Big] + \text{const.} \end{aligned} \tag{2.19}$$

This result is apparently a lot more interesting than the decoupling in the direct channel. For example, we get expectation values of the form $\langle b_{-\mathbf{k}\bar{\sigma}} b_{\mathbf{k}\sigma} \rangle = \bar{\Delta}_{\mathbf{k}\sigma}$ where two annihilation operator of the normal metal appear. At first sight one might naively think that those terms should vanish, as in any normal metal. This would certainly be true if we would calculate the expectation value with regard to the non-interacting Hamiltonian H_0, where we would find $\langle b_{-\mathbf{k}\bar{\sigma}} b_{\mathbf{k}\sigma} \rangle_0 = 0$. However, here we need to calculate the the expectation value with respect to the full Hamiltonian H_{tot}, which includes the interaction term H_{int}. Indeed, we will find that the mean-field parameters $\bar{\Delta}_{\mathbf{k}\sigma}$ describe the induced Cooper pair amplitude in the normal metal which arises from Cooper pairs from the superconductor penetrating into the normal metal region without immediately decaying at the interface.

Turning again to our more informative notation, we find

$$
\begin{aligned}
&\mathcal{H}_{\mathrm{MF,Cooper}}(\mathbf{k}) = \mathcal{H}_0(\mathbf{k}) + \mathcal{H}_{\mathrm{int,MF,Cooper}}(\mathbf{k}) \\
&= \begin{array}{c|cccc|cccc}
 & b_{\mathbf{k}\uparrow} & b_{\mathbf{k}\downarrow} & b^\dagger_{-\mathbf{k}\uparrow} & b^\dagger_{-\mathbf{k}\downarrow} & & & & \\
b^\dagger_{\mathbf{k}\uparrow} & f(\mathbf{k}) & & & 2\tilde{\Delta}_{\mathbf{k}\uparrow}\tilde{W}^*_{\mathbf{k}} & & & & \\
b^\dagger_{\mathbf{k}\downarrow} & & f(\mathbf{k}) & 2\tilde{\Delta}_{\mathbf{k}\downarrow}\tilde{W}^*_{\mathbf{k}} & & & & & \\
b_{-\mathbf{k}\uparrow} & & 2\tilde{\Delta}^*_{\mathbf{k}\downarrow}\tilde{W}_{\mathbf{k}} & -f^*(-\mathbf{k}) & & & & & \\
b_{-\mathbf{k}\downarrow} & 2\tilde{\Delta}^*_{\mathbf{k}\uparrow}\tilde{W}_{\mathbf{k}} & & & -f^*(-\mathbf{k}) & & & & \\
\hline
c^\dagger_{\mathbf{k}\uparrow} & & & & & g(\mathbf{k}) & & & \Delta + 2\bar{\Delta}_{\mathbf{k}\uparrow}\tilde{W}_{\mathbf{k}} \\
c^\dagger_{\mathbf{k}\downarrow} & & & & & & g(\mathbf{k}) & -\Delta + 2\bar{\Delta}_{\mathbf{k}\downarrow}\tilde{W}_{\mathbf{k}} & \\
c_{-\mathbf{k}\uparrow} & & & & & & -\Delta^* + 2\bar{\Delta}^*_{\mathbf{k}\downarrow}\tilde{W}^*_{\mathbf{k}} & -g^*(-\mathbf{k}) & \\
c_{-\mathbf{k}\downarrow} & & & & & \Delta^* + 2\bar{\Delta}^*_{\mathbf{k}\uparrow}\tilde{W}^*_{\mathbf{k}} & & & -g^*(-\mathbf{k}) \\
 & & & & & c_{\mathbf{k}\uparrow} & c_{\mathbf{k}\downarrow} & c^\dagger_{-\mathbf{k}\uparrow} & c^\dagger_{-\mathbf{k}\downarrow}
\end{array}
\begin{array}{c}
b^\dagger_{\mathbf{k}\uparrow} \\ b^\dagger_{\mathbf{k}\downarrow} \\ b_{-\mathbf{k}\uparrow} \\ b_{-\mathbf{k}\downarrow} \\ c^\dagger_{\mathbf{k}\uparrow} \\ c^\dagger_{\mathbf{k}\downarrow} \\ c_{-\mathbf{k}\uparrow} \\ c_{-\mathbf{k}\downarrow}
\end{array}
\end{aligned}
\tag{2.20}
$$

Here we can nicely see how a pairing amplitude gets induced into the normal metal, as can be expected from the superconducting proximity effect [40]. It is also instructive to see that the pairing potential within the superconductor gets modified. This is expected, as Cooper pairs leaking into the normal metal will reduce the Cooper pair density within the superconductor. However, this qualitative analysis does not allow for any insight whether this is really the case. Only a self consistent calculation of the mean-field parameters allows to determine whether the pairing potential in the superconductor is really reduced. If it turns out that the pairing potential is increased instead, then this would be a clear indication that something has gone wrong during the calculation.

Unified Mean-Field Decoupling

Having investigated both the direct channel and the Cooper channel for decoupling the interaction with a mean-field approach, it would now be time to decide which channel contributes

stronger and is thus more important for the interesting physics. However, given the fact that both channels yield interesting physical results, namely the tunneling limit for the direct channel and the superconducting proximity effect for the Cooper channel, it is highly likely that both channels contribute in a meaningful way and thus should to be considered simultaneously. This is nothing out of the ordinary, though details and reasoning of the exact steps are often omitted [36, 61].

We start by first splitting the full interaction (2.9) in two and then decouple one part in the direct channel and the other part in the Cooper channel

$$H_{\text{int}} = \underbrace{\frac{1}{2}H_{\text{int}}}_{\rightarrow\text{direct channel}} + \underbrace{\frac{1}{2}H_{\text{int}}}_{\rightarrow\text{Cooper channel}} . \tag{2.21}$$

Note that this splitting seems completely arbitrary and indeed nothing guarantees us that both channels should carry equal weight. However, keep in mind that when calculating the mean-field parameters self-consistently we do so for both channels simultaneously and thus the magnitude of the self-consistent order parameters will adjust for this seemingly arbitrary splitting.

Building upon our earlier results, the interaction Hamiltonian comprising both the direct channel and the Cooper channel is given by

$$H_{\text{int,MF}} = \frac{1}{2}H_{\text{inf,MF,direct}} + \frac{1}{2}H_{\text{int,MF,Cooper}}, \tag{2.22}$$

where $H_{\text{int,MF,direct}}$ is given by (2.15) and $H_{\text{int,MF,Cooper}}$ by (2.19). Including the non-interacting parts for the normal metal (2.2) and the superconductor (2.4), we can write the complete mean-field Hamiltonian decoupled in both the direct channel and the Cooper channel as

$$H_{\text{MF}} = \frac{1}{2}\sum_{\mathbf{k}} A_{\mathbf{k}}^{\dagger}\mathcal{H}_{\text{MF}}(\mathbf{k})A_{\mathbf{k}}, \tag{2.23}$$

where $A^\dagger_{\mathbf{k}}$ is again given by (2.7) and

$$\mathcal{H}_{\mathrm{MF}}(\mathbf{k}) = \mathcal{H}_0(\mathbf{k}) + \frac{1}{2}\mathcal{H}_{\mathrm{int,MF,direct}}(\mathbf{k}) + \frac{1}{2}\mathcal{H}_{\mathrm{int,MF,Cooper}}(\mathbf{k})$$

$$= \begin{array}{c|cccc|cccc|c}
 & b_{\mathbf{k}\uparrow} & b_{\mathbf{k}\downarrow} & b^\dagger_{-\mathbf{k}\uparrow} & b^\dagger_{-\mathbf{k}\downarrow} & c_{\mathbf{k}\uparrow} & c_{\mathbf{k}\downarrow} & c^\dagger_{-\mathbf{k}\uparrow} & c^\dagger_{-\mathbf{k}\downarrow} & \\
\hline
b^\dagger_{\mathbf{k}\uparrow} & f(\mathbf{k}) & & & \tilde{\Delta}_{\mathbf{k}\uparrow}\tilde{W}^*_{\mathbf{k}} & -\Gamma^*_{-\mathbf{k}\downarrow}\tilde{W}^*_{\mathbf{k}} & & & & b^\dagger_{\mathbf{k}\uparrow} \\
b^\dagger_{\mathbf{k}\downarrow} & & f(\mathbf{k}) & \tilde{\Delta}_{\mathbf{k}\downarrow}\tilde{W}^*_{\mathbf{k}} & & & -\Gamma^*_{-\mathbf{k}\uparrow}\tilde{W}^*_{\mathbf{k}} & & & b^\dagger_{\mathbf{k}\downarrow} \\
b_{-\mathbf{k}\uparrow} & & \tilde{\Delta}^*_{\mathbf{k}\downarrow}\tilde{W}_{\mathbf{k}} & -f^*(-\mathbf{k}) & & & & \Gamma_{\mathbf{k}\downarrow}\tilde{W}_{\mathbf{k}} & & b_{-\mathbf{k}\uparrow} \\
b_{-\mathbf{k}\downarrow} & \tilde{\Delta}^*_{\mathbf{k}\uparrow}\tilde{W}_{\mathbf{k}} & & & -f^*(-\mathbf{k}) & & & & \Gamma_{\mathbf{k}\uparrow}\tilde{W}_{\mathbf{k}} & b_{-\mathbf{k}\downarrow} \\
\hline
c^\dagger_{\mathbf{k}\uparrow} & -\Gamma_{-\mathbf{k}\downarrow}\tilde{W}_{\mathbf{k}} & & & & g(\mathbf{k}) & & & \Delta + \bar{\Delta}_{\mathbf{k}\uparrow}\tilde{W}_{\mathbf{k}} & c^\dagger_{\mathbf{k}\uparrow} \\
c^\dagger_{\mathbf{k}\downarrow} & & -\Gamma_{-\mathbf{k}\uparrow}\tilde{W}_{\mathbf{k}} & & & & g(\mathbf{k}) & -\Delta + \bar{\Delta}_{\mathbf{k}\downarrow}\tilde{W}_{\mathbf{k}} & & c^\dagger_{\mathbf{k}\downarrow} \\
c_{-\mathbf{k}\uparrow} & & & \Gamma^*_{\mathbf{k}\downarrow}\tilde{W}^*_{\mathbf{k}} & & & -\Delta^* + \bar{\Delta}^*_{\mathbf{k}\downarrow}\tilde{W}^*_{\mathbf{k}} & -g^*(-\mathbf{k}) & & c_{-\mathbf{k}\uparrow} \\
c_{-\mathbf{k}\downarrow} & & & & \Gamma^*_{\mathbf{k}\uparrow}\tilde{W}^*_{\mathbf{k}} & \Delta^* + \bar{\Delta}^*_{\mathbf{k}\uparrow}\tilde{W}^*_{\mathbf{k}} & & & -g^*(-\mathbf{k}) & c_{-\mathbf{k}\downarrow} \\
\hline
 & c_{\mathbf{k}\uparrow} & c_{\mathbf{k}\downarrow} & c^\dagger_{-\mathbf{k}\uparrow} & c^\dagger_{-\mathbf{k}\downarrow} & & & & &
\end{array}. \tag{2.24}$$

Here we can nicely see how the mean-field Hamiltonian contains both, effective single electron hopping between normal metal and superconductor as well as induced pairing amplitude in the normal metal and a modified pairing potential in the superconductor. This is exactly what we expect to find from experiments, and we therefore think that this is the correct form of the Andreev interaction in a tight binding model after a mean-field decoupling.

As a next step it would now be required to (numerically) calculate the mean-field parameters self-consistently. This is strongly dependent on the exact forms of both the normal metal and the superconductor and thus outside the scope of this work. However, all the physics behind the phenomenon of Andreev reflection is now explained and the self-consistent calculation merely needs a numerical implementation, though we admit that this is challenging in its own way.

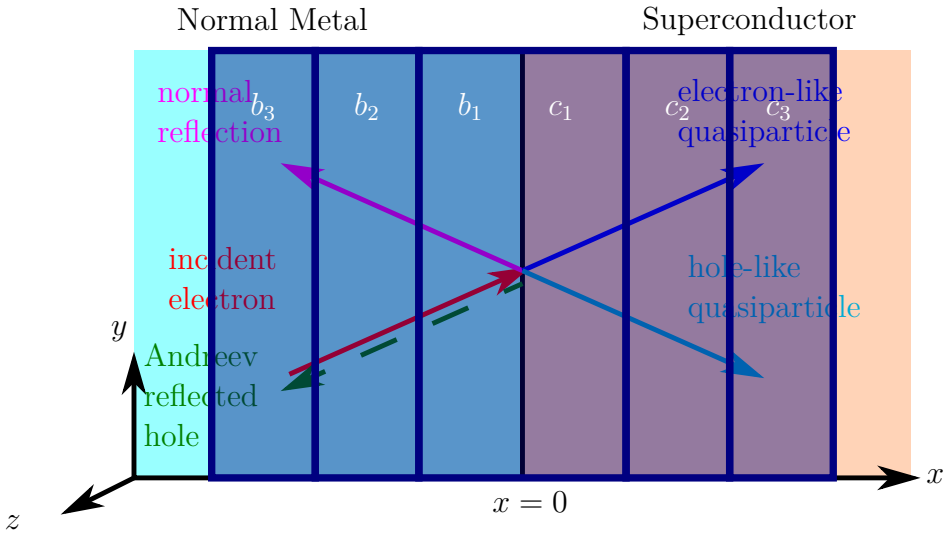

Figure 2.2: Normal metal – superconductor junction. The junction is modeled by multiple unit cells of the normal metal and of the superconductor on the sides of the junction in x-direction. y- and z-directions are assumed to be infinite. Electronic creation/annihilation operators are denoted by $b_n^\dagger/b_n$ on the normal metal side of the junction, and by $c_n^\dagger/c_n$ on the superconductor side. The operator index n denotes the n-th unit cell of the normal metal (superconductor) in the $-x$-direction ($+x$-direction).

2.1.4 Andreev Reflection in Multiple Layers

One of the major drawbacks of the aforementioned tight-binding approach to accurately describing Andreev reflection is the rather limited region in which the Andreev reflection occurs. While it does not cause a step-function-like drop of the superconducting order parameter, it is still far from the expected Cooper pair coherence length during which Andreev reflection occurs [39].

This last part of the chapter on Andreev reflection is thus dedicated to an extension of the earlier tight-binding model to account for a larger region next to the interface where Andreev reflection occurs. To this end we extend the system to be comprised of multiple unit cells of the normal metal and the superconductor in the x-direction, while the y- and z-directions are considered to be infinite, as before. The electronic creation/annihilation operators $b_n^\dagger/b_n$ ($c_n^\dagger/c_n$) of the normal metal (superconductor) are now indexed in order to indicate the n-th unit cell from the interface to which they belong to, see Figure 2.2.

The new interaction covering all unit cells can be expressed as

$$H_{\text{int,total}} = H_{\text{int}} + H_{\text{int,NM}} + H_{\text{int,SC}} \tag{2.25}$$

where H_{int} refers to the interaction between the unit cells directly at the interface, as described in (2.13), $H_{\text{int,NM}}$ describes the interaction induced in the unit cells on the normal metal side of the interface and $H_{\text{int,SC}}$ describes the interaction in the unit cell on the superconductor side. The interaction induced by the junction in the normal metal side can be written as

$$H_{\text{int,NM}} = \sum_{\mathbf{k}} \sum_{\sigma} \sum_{i=1}^{N_{\text{NM}}-1} W_{\text{NM},\mathbf{k}} b_{i+1,-\mathbf{k}\bar{\sigma}} b_{i+1,\mathbf{k}\sigma} b^{\dagger}_{i,\mathbf{k}\sigma} b^{\dagger}_{i,-\mathbf{k}\bar{\sigma}} + W^{*}_{\text{NM},\mathbf{k}} b_{i,-\mathbf{k}\bar{\sigma}} b_{i,\mathbf{k}\sigma} b^{\dagger}_{i+1,\mathbf{k}\sigma} b^{\dagger}_{i+1,-\mathbf{k}\bar{\sigma}}. \tag{2.26}$$

Here N_{NM} denotes how many unit cells on the normal metal side are used and $W_{\text{NM},\mathbf{k}}$ accounts for any peculiar momentum dependencies within the normal metal. Similarly, the interaction on the superconducting side can be written as

$$H_{\text{int,SC}} = \sum_{\mathbf{k}} \sum_{\sigma} \sum_{i=1}^{N_{\text{SC}}-1} W_{\text{SC},\mathbf{k}}, c_{i,-\mathbf{k}\bar{\sigma}} c_{i,\mathbf{k}\sigma} c^{\dagger}_{i+1,\mathbf{k}\sigma} c^{\dagger}_{i+1,-\mathbf{k}\bar{\sigma}} + W^{*}_{\text{SC},\mathbf{k}} c_{i+1,-\mathbf{k}\bar{\sigma}} c_{i+1,\mathbf{k}\sigma} c^{\dagger}_{i,\mathbf{k}\sigma} c^{\dagger}_{i,-\mathbf{k}\bar{\sigma}}, \tag{2.27}$$

where, as above, N_{SC} denotes the number of unit cells on the superconductor side and $W_{\text{SC},\mathbf{k}}$ accounts for momentum dependencies within the superconductor as well as the coherence factors of the superconductor.

Splitting the action evenly as in (2.21) and applying the mean-field decoupling in the direct channel (Cooper channel) on the first (second) term, we will find the mean-field interaction for the normal metal part as

$$\begin{aligned} H_{\text{int,NM,MF}} = \frac{1}{2} \sum_{\mathbf{k}} \sum_{\sigma} \sum_{i=1}^{N_{\text{NM}}-1} & W_{\text{NM},\mathbf{k}} \left[b_{i+1,-\mathbf{k}\bar{\sigma}} b^{\dagger}_{i,-\mathbf{k}\bar{\sigma}} \Gamma_{\text{NM},i,\mathbf{k}\sigma} + b_{i+1,\mathbf{k}\sigma} b^{\dagger}_{i,\mathbf{k}\sigma} \Gamma_{\text{NM},i,-\mathbf{k}\bar{\sigma}} \right] \\ & + W^{*}_{\text{NM},\mathbf{k}} \left[b_{i,-\mathbf{k}\bar{\sigma}} b^{\dagger}_{i+1,-\mathbf{k}\bar{\sigma}} \Gamma^{*}_{\text{NM},i,\mathbf{k}\sigma} + b_{i,\mathbf{k}\sigma} b^{\dagger}_{i+1,\mathbf{k}\sigma} \Gamma^{*}_{\text{NM},i,-\mathbf{k}\bar{\sigma}} \right] \\ & + W_{\text{NM},\mathbf{k}} \left[b_{i+1,-\mathbf{k}\bar{\sigma}} b_{i+1,\mathbf{k}\sigma} \tilde{\Delta}^{*}_{\text{NM},i,\mathbf{k}\sigma} + b^{\dagger}_{i,\mathbf{k}\sigma} b^{\dagger}_{i,-\mathbf{k}\bar{\sigma}} \bar{\Delta}_{\text{NM},i,\mathbf{k}\sigma} \right] \\ & + W^{*}_{\text{NM},\mathbf{k}} \left[b_{i,-\mathbf{k}\bar{\sigma}} b_{i,\mathbf{k}\sigma} \bar{\Delta}^{*}_{\text{NM},i,\mathbf{k}\sigma} + b^{\dagger}_{i+1,\mathbf{k}\sigma} b^{\dagger}_{i+1,-\mathbf{k}\bar{\sigma}} \tilde{\Delta}_{\text{NM},i,\mathbf{k}\sigma} \right], \end{aligned} \tag{2.28}$$

where the constant arising from the mean-field procedure has been suppressed again. The

mean-field parameters are given by

$$\Gamma_{\mathrm{NM},i,\mathbf{k}\sigma} = \langle b_{i+1,\mathbf{k}\sigma} b^\dagger_{i,\mathbf{k}\sigma} \rangle \tag{2.29}$$

$$\Gamma_{\mathrm{NM},i,-\mathbf{k}\bar{\sigma}} = \langle b_{i+1,-\mathbf{k}\bar{\sigma}} b^\dagger_{i,-\mathbf{k}\bar{\sigma}} \rangle \tag{2.30}$$

$$\bar{\Delta}_{\mathrm{NM},i,\mathbf{k}\sigma} = \langle b_{i+1,-\mathbf{k}\bar{\sigma}} b_{i+1,\mathbf{k}\sigma} \rangle \tag{2.31}$$

$$\tilde{\Delta}_{\mathrm{NM},i,\mathbf{k}\sigma} = \langle b_{i,-\mathbf{k}\bar{\sigma}} b_{i,\mathbf{k}\sigma} \rangle. \tag{2.32}$$

Here again one might object that there is no Cooper pair pairing potential in a normal metal and consequently the mean-field parameters $\bar{\Delta}_{\mathrm{NM},i,\mathbf{k}\sigma}$ and $\tilde{\Delta}_{\mathrm{NM},i,\mathbf{k}\sigma}$ should vanish. However, the same argument as before applies and the required Cooper pair pairing amplitude will be coming from the adjacent unit cells within the normal metal, starting from the junction. The mean-field parameters $\bar{\Delta}_{\mathrm{NM},i,\mathbf{k}\sigma}$ and $\tilde{\Delta}_{\mathrm{NM},i,\mathbf{k}\sigma}$ therefore need to be calculated according to (2.31) and (2.32) using the full Hamiltonian (2.25) or rather its mean-field decoupled version (2.38). Moving on to the interaction within the superconductor (2.27) and applying the same mean-field decoupling there, we find

$$\begin{aligned} H_{\mathrm{int,SC,MF}} = \frac{1}{2} \sum_{\mathbf{k}} \sum_{\sigma} \sum_{i=1}^{N_{\mathrm{SC}}-1} & W_{\mathrm{SC},\mathbf{k}} \left[c_{i,\mathbf{k}\sigma} c^\dagger_{i+1,\mathbf{k}\sigma} \Gamma_{\mathrm{SC},i,-\mathbf{k}\bar{\sigma}} + c_{i,-\mathbf{k}\bar{\sigma}} c^\dagger_{i+1,-\mathbf{k}\bar{\sigma}} \Gamma_{\mathrm{SC},i,\mathbf{k}\sigma} \right] \\ & + W^*_{\mathrm{SC},\mathbf{k}} \left[c_{i+1,\mathbf{k}\sigma} c^\dagger_{i,\mathbf{k}\sigma} \Gamma^*_{\mathrm{SC},i,-\mathbf{k}\bar{\sigma}} + c_{i+1,-\mathbf{k}\bar{\sigma}} c^\dagger_{i,-\mathbf{k}\bar{\sigma}} \Gamma^*_{\mathrm{SC},i,\mathbf{k}\sigma} \right] \\ & + W_{\mathrm{SC},\mathbf{k}} \left[c_{i,-\mathbf{k}\bar{\sigma}} c_{i,\mathbf{k}\sigma} \tilde{\Delta}^*_{\mathrm{SC},i,\mathbf{k}\sigma} + c^\dagger_{i+1,\mathbf{k}\sigma} c^\dagger_{i+1,-\mathbf{k}\bar{\sigma}} \bar{\Delta}_{\mathrm{SC},i,\mathbf{k}\sigma} \right] \\ & + W^*_{\mathrm{SC},\mathbf{k}} \left[c_{i+1,-\mathbf{k}\bar{\sigma}} c_{i+1,\mathbf{k}\sigma} \bar{\Delta}^*_{\mathrm{SC},i,\mathbf{k}\sigma} + c^\dagger_{i,\mathbf{k}\sigma} c^\dagger_{i,-\mathbf{k}\bar{\sigma}} \tilde{\Delta}_{\mathrm{SC},i,\mathbf{k}\sigma} \right], \end{aligned} \tag{2.33}$$

again with the constant arising from the mean-field procedure being suppressed. The mean-field parameters are given by

$$\Gamma_{\mathrm{SC},i,\mathbf{k}\sigma} = \langle c_{i,\mathbf{k}\sigma} c^\dagger_{i+1,\mathbf{k}\sigma} \rangle \tag{2.34}$$

$$\Gamma_{\mathrm{SC},i,-\mathbf{k}\bar{\sigma}} = \langle c_{i,-\mathbf{k}\bar{\sigma}} c^\dagger_{i+1,-\mathbf{k}\bar{\sigma}} \rangle \tag{2.35}$$

$$\bar{\Delta}_{\mathrm{SC},i,\mathbf{k}\sigma} = \langle c_{i,-\mathbf{k}\bar{\sigma}} c_{i,\mathbf{k}\sigma} \rangle \tag{2.36}$$

$$\tilde{\Delta}_{\mathrm{SC},i,\mathbf{k}\sigma} = \langle c_{i+1,-\mathbf{k}\bar{\sigma}} c_{i+1,\mathbf{k}\sigma} \rangle. \tag{2.37}$$

With this we have now found all parts of the mean-field decoupled Hamiltonian both at the immediate interface as well as within the normal metal and within the superconductor. The entire mean-field decoupled Hamiltonian is then simply given by

$$H_{\mathrm{MF,total}} = H_{\mathrm{NM}} + H_{\mathrm{SC}} + H_{\mathrm{MF}} + H_{\mathrm{int,NM,MF}} + H_{\mathrm{int,SC,MF}}, \tag{2.38}$$

where H_{NM} (H_{SC}) refers to the unperturbed normal metal (2.2) (superconductor (2.4)). H_{MF}, $H_{\mathrm{int,NM,MF}}$ and $H_{\mathrm{int,SC,MF}}$ are as given above in equations (2.22), (2.28) and (2.33), respectively. With this we now have an explicit description of Andreev reflection in a finite size tight-binding model by the means of a mean-field Hamiltonian. Before ending this part, we would like to briefly comment on the size of the interaction region between normal metal and superconductor. In a mean-field model it is always desirable to limit the amount mean-field parameters so that the computational difficulty remains manageable. In our case that means restricting the the number of unit cells away from the normal metal–superconductor interface which contribute to the Andreev reflection. We have chosen to allow for different number of unit cells of normal metal/superconductor to be taken into account, because there is no obvious reason why the interaction should symmetrically decay in both materials with increasing distance from the interface. In order to give an estimate of how large an interaction zone within the superconductor should be taken into account, we can have a look at how far from the surface of a superconductor in vacuum the pairing potential reaches the bulk limit. For the range of the interaction zone inside the normal metal, the superconducting coherence length of the superconductor is a good starting point.

2.1.5 Remarks

To finish off this chapter, let us have a quick look at the advantages of our novel approach to Andreev reflection. The biggest advantage of the presented tight-binding approach to Andreev reflection is likely the possibility to self-consistently calculate the superconducting order parameter over a large volume and not be restricted to just the immediate vicinity of the normal metal–superconductor junction. Furthermore, the approach is not restricted to only normal metal–superconductor junctions. In principle it is possible to substitute any material for the normal metal. A common weakness of such large scale numerical systems is however their computational complexity, which might make cause issues especially in cases of a long coherence length of the Cooper pairs, in which case it is expected to find a non-vanishing pairing amplitude in the non-superconducting region for a very long distance. Nonetheless we believe that the tight-binding description of Andreev reflection can be a helpful tool in many situations and allow for an easy extension of many existing problems where the superconducting proximity effect is crudely modeled by a simple step function for the pairing amplitude.

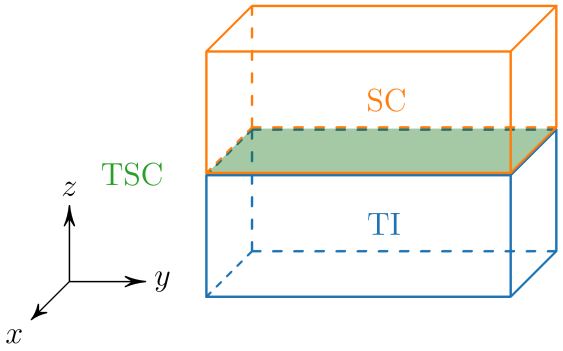

Figure 2.3: Topological insulator–superconductor heterostructure stacked in z-direction. Indicated by the green plane is the interface at which a topological superconductor is predicted to form.

2.2 Topological Insulator–Superconductor Model

In this section we will introduce our tight-binding model of the topological insulator–superconductor system. The model we have chosen focuses on the essential physics, but at the same time remains sufficiently close to existing materials and uses realistic parameters throughout.
As a reminder, we need to construct a three dimensional topological insulator–superconductor heterostructure. For concreteness, the system will be stacked in the z-direction, whereas x- and y-directions are taken as infinite, in a setup as shown Figure 2.3. In this setup the predicted two dimensional induced topological superconductor lies in the x-y-plane, at the interface between topological insulator and s-wave superconductor.

2.2.1 Topological Insulator

We will first introduce the model of the topological insulator. It is modeled on a cubic three dimensional lattice. The model is a isotropic variant derived from a commonly used low-energy effective model near the Γ point of topological insulators such as Sb_2Te_3, Bi_2Se_3 and Bi_2Te_3 [62].
The model Hamiltonian on an infinite three dimensional lattice is given by

$$H = \sum_{\mathbf{k}} B_{\mathbf{k}}^{\dagger} \mathcal{H}(\mathbf{k}) B_{\mathbf{k}}, \tag{2.39}$$

where

$$B_{\mathbf{k}}^{\dagger} = (b_{\mathbf{k}+\uparrow}^{\dagger}, b_{\mathbf{k}+\downarrow}^{\dagger}, b_{\mathbf{k}-\uparrow}^{\dagger}, b_{\mathbf{k}-\downarrow}^{\dagger}), \tag{2.40}$$

and $+/-$ denotes the different orbitals, whereas $\uparrow$ / $\downarrow$ denotes the spin. $\mathcal{H}(\mathbf{k})$ is given by

$$\mathcal{H}(\mathbf{k}) = \epsilon_0(\mathbf{k})\tau_0\sigma_0 + A\sum_{i=1}^{3}\sin(k_i a)\tau_x\sigma_i + M(\mathbf{k})\tau_z\sigma_0. \tag{2.41}$$

Here τ_i (σ_i) denotes the Pauli matrices in orbital space (spin space) and $\tau_0 = \sigma_0 = \mathbb{1}_{2\times2}$ is the 2×2 unit matrix. The first two parts of the Hamiltonian correspond to regular hopping on a lattice, whereas the last term originally originates from spin orbit coupling and is responsible for a band inversion around $\mathbf{k} = (0,0,0)$. The separate terms of the Hamiltonian are given by

$$\epsilon_0(\mathbf{k}) = C + D\sum_{i=1}^{3}\sin^2\frac{k_i a}{2} \tag{2.42}$$

$$M(\mathbf{k}) = G - 4B\sum_{i=1}^{3}\sin^2\frac{k_i a}{2}. \tag{2.43}$$

The system is both time reversal symmetric and inversion symmetric. Inversion symmetry is given by $U_I = \tau_z\sigma_0$. Time reversal symmetry is given by $\mathcal{T} = U_T\mathcal{K}$, where $U_T = \tau_0\sigma_y$ and $\mathcal{K}$ denotes complex conjugation. With $\mathcal{T}^2 = -1$ the topological insulator belongs to symmetry class AII, allowing for a $\mathbb{Z}_2$ topological invariant, as expected [63–65].
A similar system with $C = D = 0$ has been been investigated before [66] and it was found to be topologically non-trivial for the following conditions

$$0 < G < 4B \rightarrow \text{strong topological insulator} \tag{2.44}$$

$$4B < G < 8B \rightarrow \text{weak topological insulator} \tag{2.45}$$

$$8B < G < 12B \rightarrow \text{strong topological insulator} \tag{2.46}$$

$$\text{else} \rightarrow \text{trivial band insulator.} \tag{2.47}$$

$$\tag{2.48}$$

Here, weak topological insulator means that is a trivial band insulator in the presence of disorder, whereas the strong topological insulator remains robust even in the presence of disorder [51]. For the rest of our studies we will be focusing on the strong topological insulator and thus avoid the region where the system becomes a weak topological insulator.
Before continuing, we would like to point out that omitting the diagonal terms in (2.41) by setting $C = D = 0$ introduces a particle-hole like symmetry between electrons of different orbitals and also makes the system qualitatively different from the low-energy effective model for real materials such as Bi_2Se_2. It is important to note that neither the C-term nor the D-

term change the topological character of the system, as long as they do not close the band gap. This does not introduce any restrictions onto the C-term, as it is diagonal and independent of any momentum $\mathbf{k}$ and therefore only causes a constant shift of the band structure. The D-term however does deform the bands and can potentially close the band gap if it exceeds A. In the following we will therefore always choose D to be small but non-zero so that we do not accidentally close the band gap and at the same time avoid a spurious particle-hole like symmetry between the different orbitals.

Having established the Hamiltonian of the topological insulator in momentum space, we next need to transform it into real space in order to introduce an interface where to observe the topologically protected surface states and also to prepare for adding a superconductor to a surface of the topological insulator. Since we only need one surface, we take the topological insulator infinite in two directions and finite only in one direction, for example the z-direction. We can then maintain k_x- and k_y-directions in momentum space and thus significantly reduce the computational complexity of the system.

As a quick recall, the partial Fourier transform in z-direction is performed via

$$b^\dagger_{\mathbf{k}\eta} = \frac{1}{\sqrt{N_z}} \sum_i e^{i\mathbf{R}_{i,z}} b^\dagger_{i,k_x,k_y,\eta}, \tag{2.49}$$

where η comprises both orbital degree of freedom τ and spin degree of freedom σ. The transformed Hamiltonian can then be written as

$$H = \sum_{k_x,k_y} \sum_{i,j} B^\dagger_{k_x,k_y,i} \mathcal{H}_{i,j}(k_x,k_y) B_{k_x,k_y,j} \tag{2.50}$$

with

$$B^\dagger_{k_x,k_y,i} = (b^\dagger_{k_x,k_y,i,+\uparrow}, b^\dagger_{k_x,k_y,i,+\downarrow}, b^\dagger_{k_x,k_y,i,-\uparrow}, b^\dagger_{k_x,k_y,i,-\downarrow}) \tag{2.51}$$

and

$$\begin{aligned}
\mathcal{H}_{i,j}(k_x,k_y) = {} & \frac{A}{2i}(\delta_{i,j-1} - \delta_{i,j+1})\tau_x\sigma_z - 2B\left[\delta_{i,j} - \frac{1}{2}(\delta_{i,j-1} + \delta_{i,j+1})\right]\tau_z\sigma_0 \\
& + \frac{D}{2}\left[\delta_{i,j} - \frac{1}{2}(\delta_{i,j-1} + \delta_{i,j+1})\right]\tau_0\sigma_0 \\
& + A\sin(k_x a)\delta_{i,j}\tau_x\sigma_x + A\sin(k_y a)\delta_{i,j}\tau_x\sigma_y \\
& + \left[G - 4B\left(\sin^2\frac{k_x a}{2} + \sin^2\frac{k_y a}{2}\right)\right]\delta_{i,j}\tau_z\sigma_0 \\
& + \left[C + D\left(\sin^2\frac{k_x a}{2} + \sin^2\frac{k_y a}{2} + \sin^2\frac{k_z a}{2}\right)\right]\delta_{i,j}\tau_0\sigma_0
\end{aligned} \tag{2.52}$$

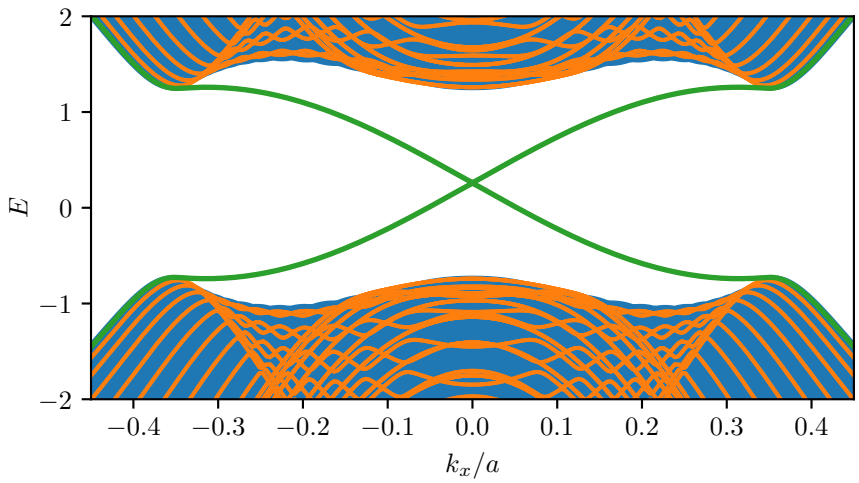

Figure 2.4: Band structure of a topological insulator, plotted for multiple different momenta k_y and $N = 20$ unit cells in z-direction (orange). Clearly seen can be the surface states within the gap (green). Indicated in blue is the band structure for the infinite model without surfaces nor surface states.

with $\delta_{n,m}$ being the Kronecker delta. By restricting the sum $\sum_{i,j}$ in (2.50) to be finite, say from 1 to N_{TI}, we obtain a topological insulator which is finite in z-direction and thus exhibits two surfaces parallel to the x-y-plane. The resulting band structure is shown in Figure 2.4, where the blue shaded background indicates the band structure of the infinite topological insulator as defined in (2.41). In the figure one can clearly see the surface bands within the band gap, meeting at $k_x = k_y = 0$, albeit not at $E = 0$. This is due to the diagonal terms C and D, which shift and slightly distort the band structure. In order to see how strongly the surface states are located at the surface, we plot the probability density of the wave function of the band touching point in Figure 2.5. As can be clearly seen, the surface wave functions are strongly located towards the surface of the sample and practically absent in the bulk. Note that the apparent hybridization between the edges is a mathematical artifact arising from the fact that the surface states at both surfaces have exactly the same eigenenergy. This degeneracy can be lifted by making the surfaces non-equivalent and thus slightly shifting their band structures. We will now do this by applying the superconducting proximity effect on one surface only.

Topological Insulator with Superconducting Proximity Effect

Before moving on to construct the entire topological insulator–superconductor structure, let us first discuss only applying the superconducting proximity effect to the bottom surface of the topological insulator. This will allow us to distinguish the top from the bottom surface

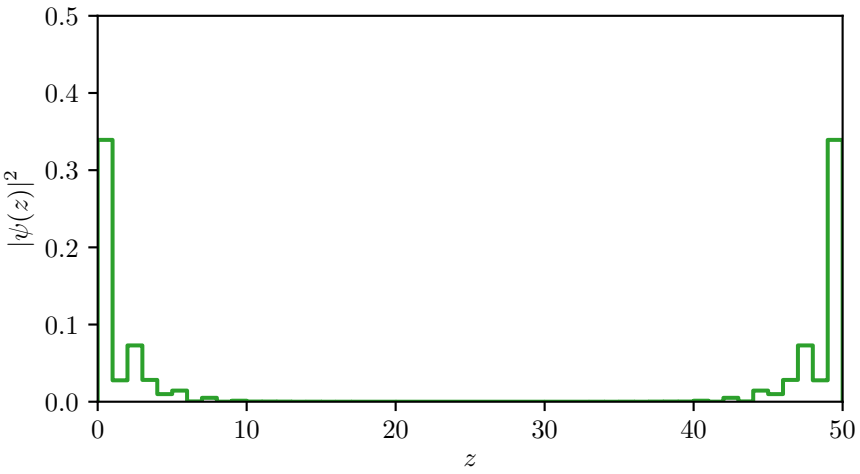

Figure 2.5: Probability density of the wave function of the topological insulator corresponding to the band touching point in Figure 2.4, albeit for a sample thickness of $N = 50$ unit cells in z-direction. A strong localization towards the edges of the sample can be observed. The perceived simultaneous localization at both edges is a mathematical artifact: Both surfaces have states with the same eigenvalue. The calculated eigenvectors can thus be any linear combination of the eigenvectors belonging to either surface. Physically the states will be localized at either surface, as can be observed when making both surfaces in-equivalent, for example by imposing the superconducting proximity effect on one surface, as done in Figure 2.7

and allows us to remove the states from the bottom surface out of the band gap. This in turn will help us identify the relevant states at the top surface of the topological insulator, which will remain completely unaffected. The procedure for adding the superconducting proximity effect on the bottom surface is quite simple and goes as follows: First, we rewrite the Hamiltonian (2.39) as a BdG Hamiltonian, Fourier transform the k_z-component to real space and then as the last step apply a superconducting pairing amplitude to bottom surface.
Rewriting (2.39) as BdG Hamiltonian results in

$$H_{\mathrm{BdG}} = \frac{1}{2}\sum_{\mathbf{k}} B_{\mathbf{k}}^{\dagger}\mathcal{H}_{\mathrm{BdG}}(\mathbf{k})B_{\mathbf{k}}, \tag{2.53}$$

with

$$B_{\mathbf{k}}^{\dagger} = (b_{\mathbf{k}+\uparrow}^{\dagger}, b_{\mathbf{k}+\downarrow}^{\dagger}, b_{\mathbf{k}-\uparrow}^{\dagger}, b_{\mathbf{k}-\downarrow}^{\dagger}, b_{-\mathbf{k}+\uparrow}, b_{\mathbf{k}+\downarrow}, b_{-\mathbf{k}-\uparrow}, b_{-\mathbf{k}-\downarrow}), \tag{2.54}$$

and

$$\mathcal{H}_{\mathrm{BdG}}(\mathbf{k}) = \begin{pmatrix} \mathcal{H}(\mathbf{k}) - \mu_{\mathrm{TI}} & 0 \\ 0 & -\mathcal{H}^{*}(-\mathbf{k}) + \mu_{\mathrm{TI}} \end{pmatrix}. \tag{2.55}$$

Here, $\mathcal{H}(\mathbf{k})$ is as given in (2.41) and μ_{TI} denotes the chemical potential. We can use this chemical potential to move the Dirac node up and down. Note however that we now have both electron and hole states, so if we move the Dirac node away from Fermi level it will split into two Dirac nodes; one electronic Dirac node and one hole Dirac node. Which Dirac node is electronic and which is a hole Dirac node depends on the chemical potential.
Next we perform the Fourier transform in z-direction so that we can again build a finite system in z-direction. The Hamiltonian then becomes

$$H_{\mathrm{BdG}} = \frac{1}{2}\sum_{k_x,k_y}\sum_{i,j} B_{i,k_x,k_y}^{\dagger}\mathcal{H}_{\mathrm{BdG},i,j}(k_x,k_y)B_{j,k_x,k_y} \tag{2.56}$$

where

$$\begin{aligned}\mathcal{H}_{\mathrm{BdG},i,j}(k_x,k_y) = &\frac{A}{2i}(\delta_{i,j-1}-\delta_{i,j+1})\rho_0\tau_x\sigma_z \\ &- 2B\left[\delta_{i,j}-\frac{1}{2}(\delta_{i,j-1}+\delta_{i,j+1})\right]\rho_z\tau_z\sigma_0 \\ &+ \frac{D}{2}\left[\delta_{i,j}-\frac{1}{2}(\delta_{i,j-1}+\delta_{i,j+1})\right]\rho_z\tau_0\sigma_0 \\ &+ A\sin(k_xa)\delta_{i,j}\rho_0\tau_x\sigma_x + A\sin(k_ya)\delta_{i,j}\rho_z\tau_x\sigma_y \\ &+ \left[G-4B\left(\sin^2\frac{k_xa}{2}+\sin^2\frac{k_ya}{2}\right)\right]\delta_{i,j}\rho_z\tau_z\sigma_0 \\ &+ \left[C+D\left(\sin^2\frac{k_xa}{2}+\sin^2\frac{k_ya}{2}\right)-\mu_{\mathrm{TI}}\right]\delta_{i,j}\rho_z\tau_0\sigma_0 \end{aligned} \tag{2.57}$$

and

$$\begin{aligned}B^\dagger_{i,k_x,k_y} = (&b^\dagger_{i,k_x,k_y+\uparrow}, b^\dagger_{i,k_x,k_y+\downarrow}, b^\dagger_{i,k_x,k_y-\uparrow}, b^\dagger_{i,k_x,k_y-\downarrow}, \\ &b_{i,-k_x,-k_y+\uparrow}, b_{i,-k_x,-k_y+\downarrow}, b_{i,-k_x,-k_y-\uparrow}, b_{i,-k_x,-k_y-\downarrow}).\end{aligned} \tag{2.58}$$

Here, as before, τ_i and σ_i denote the Pauli matrices in orbital space and spin space, respectively, whereas the newly introduced ρ_i denotes the Pauli matrices in particle-hole space. Again, we make the model finite by restricting the sum over the lattice sites $\sum_{i,j}$ to be running from 1 to N_{TI} for both i and j.

As a last step, we will add a superconducting pairing amplitude to the bottom surface of the system to mimic the superconducting proximity effect. Focusing only on the bottom surface, we can write the contribution of superconducting proximity effect to the Hamiltonian (2.56) as

$$H_{\mathrm{proximity}} = \frac{1}{2}\sum_{k_x,k_y} B^\dagger_{1,k_x,k_y}\mathcal{H}_{\mathrm{proximity}}B_{1,k_x,k_y}. \tag{2.59}$$

Here we have assumed that the induced pairing amplitude will come from a plain s-wave superconductor with a uniform pairing potential Δ which is independent of momentum $\mathbf{k}$. The induced pairing amplitude can then be written as

$$\mathcal{H}_{\mathrm{proximity}} = \begin{pmatrix} 0 & \mathcal{H}_\Delta \\ \mathcal{H}^\dagger_\Delta & 0 \end{pmatrix} \tag{2.60}$$

with

$$\mathcal{H}_\Delta = \begin{pmatrix} 0 & -\Delta_+ & 0 & -\Delta_\pm \\ \Delta_+ & 0 & \Delta_\pm & 0 \\ 0 & -\Delta_\mp & 0 & -\Delta_- \\ \Delta_\mp & 0 & \Delta_- & 0 \end{pmatrix}. \tag{2.61}$$

Here we get confronted with the many choices that the pairing amplitude can take, either in form of intraband pairing in the + band (− band), represented by Δ_+ (Δ_-) or in the form of interband pairing between the + and the − band, represented by $\Delta_\pm$ and $\Delta_\mp$. Both kinds of pairing can in principle occur and it depends on the model details which pairing channel is dominant [67–69]. However, since we are not really interested in the bottom surface and only use the proximity effect as a convenient device for clearing the surface bands from the bottom surface out of the bulk band gap, we will assume uniform intraband pairing amplitude $\Delta_+ = \Delta_- =: \Delta$ and no interband pairing amplitude $\Delta_\pm = \Delta_\mp = 0$.
The entire Hamiltonian for the topological insulator can thus be written as

$$H_{\mathrm{TI}} = H_{\mathrm{BdG}} + H_{\mathrm{proximity}}. \tag{2.62}$$

Before continuing and having a look at the band structure of the topological insulator with proximity effect applied to its bottom surface, it is instructive to rewrite the Hamiltonian in a matrix notation, as this will more easily point out what is happening once we connect the topological insulator to the superconductor. We thus rewrite the entire Hamiltonian (2.62) as

$$H_{\mathrm{TI}} = \frac{1}{2} \sum_{k_x,k_y} \vec{B}^\dagger_{k_x,k_y} \mathcal{H}_{\mathrm{TI}}(k_x,k_y) \vec{B}_{k_x,k_y}, \tag{2.63}$$

with

$$\mathcal{H}_{\mathrm{TI}}(k_x,k_y) = \begin{pmatrix} \tilde{\mathcal{H}}^{\mathrm{TI}}_D(k_x,k_y) & \mathcal{H}^{\mathrm{TI}}_N & & \\ \mathcal{H}^{\mathrm{TI}\dagger}_N & \mathcal{H}^{\mathrm{TI}}_D(k_x,k_y) & \ddots & \\ & \ddots & \mathcal{H}^{\mathrm{TI}}_D(k_x,k_y) & \mathcal{H}^{\mathrm{TI}}_N \\ & & \mathcal{H}^{\mathrm{TI}\dagger}_N & \mathcal{H}^{\mathrm{TI}}_D(k_x,k_y) \end{pmatrix} \tag{2.64}$$

and

$$\vec{B}^\dagger_{k_x,k_y} = (b^\dagger_{1,k_x,k_y+\uparrow}, b^\dagger_{1,k_x,k_y+\downarrow}, \ldots, b_{N_T I,-k_x,-k_y-\downarrow}). \tag{2.65}$$

Table 2.1: Parameters used for the topological insulator. Unless explicitly stated otherwise those parameter were used for all calculations.

A	B	C	D	G	μ_{TI}	a	N_{TI}
1eV	1.7eV	0.1eV	0.2eV	4.1eV	0.31eV	5Å	50

Here $\mathcal{H}_D^{\mathrm{TI}}(k_x, k_y)$ captures the on-site terms, whereas $\mathcal{H}_N^{\mathrm{TI}}$ describes hopping amongst adjacent lattice indices, i.e. hopping in z-direction. $\tilde{\mathcal{H}}_D^{\mathrm{TI}}(k_x, k_y)$ additionally captures the proximity effect, which is assumed to only affect the lower most layer of the system. We thus have

$$\begin{aligned}\mathcal{H}_D^{\mathrm{TI}}(k_x, k_y) = &-2B\rho_z\tau_z\sigma_0 + \frac{D}{2}\rho_z\tau_0\sigma_0 \\ &+ A\sin(k_x a)\rho_0\tau_x\sigma_x + A\sin(k_y a)\rho_z\tau_x\sigma_y \\ &+ \left[G - 4B\left(\sin^2\frac{k_x a}{2} + \sin^2\frac{k_y a}{2}\right)\right]\rho_z\tau_z\sigma_0 \\ &+ \left[C + D\left(\sin^2\frac{k_x a}{2} + \sin^2\frac{k_y a}{2}\right) - \mu_{\mathrm{TI}}\right]\rho_z\tau_0\sigma_0,\end{aligned} \tag{2.66}$$

$$\mathcal{H}_N^{\mathrm{TI}} = \frac{A}{2i}\rho_0\tau_x\sigma_z + B\rho_z\tau_z\sigma_0 - \frac{D}{4}\rho_z\tau_0\sigma_0 \tag{2.67}$$

and

$$\tilde{\mathcal{H}}_D^{\mathrm{TI}}(k_x, k_y) = \mathcal{H}_D^{\mathrm{TI}}(k_x, k_y) + \mathcal{H}_{\mathrm{proximity}} \tag{2.68}$$

Using this Hamiltonian we can now proceed and plot the band structure to see the localization of the surface states in presence of a superconductor. Figure 2.6 shows the band structure of the Hamiltonian. Here one can clearly see a gapless and a gapped surface state, corresponding to the unperturbed surface and the surface with induced pairing amplitude. The localization of those surface states is shown in Figure 2.7, showing a strong localization at either surface. Note that the previously observed spurious degeneracy between the surface states is now absent due to the states having slightly different energy.

Finishing our introduction of the topological insulator part of the model, we will give the parameters we used to characterize the topological insulator in Table 2.1. The parameters were chosen to be experimentally viable and at the same time ensure that the system is deep in the strong topological insulator phase. Unless otherwise noted, those parameter are used throughout the text.

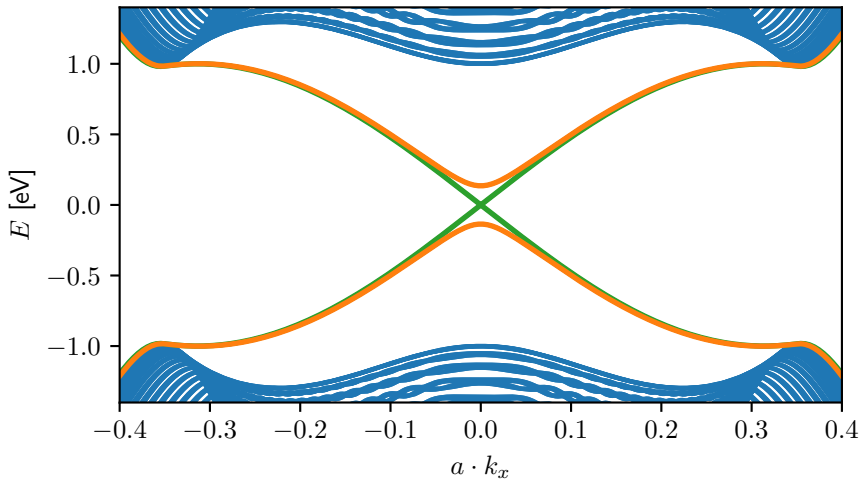

Figure 2.6: Band structure of a topological insulator with induced superconducting pairing amplitude on one surface. Surface states on unperturbed surface (green) are gapless as in Figure 2.4, whereas the surface states on the other surface (orange) are gapped due to a small induced intraband pairing amplitude.

Figure 2.7: Localization of surface states of a topological insulator with induced superconducting pairing amplitude on one surface. Wave functions both at $k_x = k_y = 0$. In green is shown the wave function at exactly zero energy, strongly localized at the non-perturbed surface, whereas in orange is shown the surface wave function at slightly off zero energy being strongly localized at the surface with the induced pairing amplitude.

2.2.2 Superconductor

We will briefly introduce the generic s-wave superconductor which we will use to construct the topological insulator–superconductor hybrid system. In order to avoid confusion about the notation, we will stick to the convention of using c and $c^\dagger$ for the annihilation and creation operators in the superconductor, respectively. Similar to subsection 2.1.1 the Hamiltonian for the superconductor is very simple and given by

$$H_{\mathrm{SC}} = \frac{1}{2}\sum_{\mathbf{k}} C_{\mathbf{k}}^\dagger \mathcal{H}_{\mathrm{SC}}(\mathbf{k}) C_{\mathbf{k}}, \tag{2.69}$$

with

$$C_{\mathbf{k}}^\dagger = (c_{\mathbf{k}\uparrow}^\dagger, c_{\mathbf{k}\downarrow}^\dagger, c_{-\mathbf{k}\uparrow}, c_{-\mathbf{k}\downarrow}) \tag{2.70}$$

and

$$\mathcal{H}_{\mathrm{SC}}(\mathbf{k}) = \big[Q\sum_{i=1}^{3}\cos ak_i - \mu_{\mathrm{SC}}\big]\rho_z\sigma_0 + \mathrm{re}\Delta\rho_y\sigma_y + \mathrm{im}\Delta\rho_x\sigma_y. \tag{2.71}$$

Here again, σ_i denotes Pauli matrices in spin space and ρ_i represents Pauli matrices in particle-hole space. This corresponds to a superconductor with a cubic lattice, as realized in lead or niobium. Note that we have deliberately chosen the same lattice constant a as for the topological insulator, because dealing with the additional complication from lattice mismatch will not gain significant new physical insight and only complicate notation and calculation.
Fourier transforming along the k_z-direction for creating a finite width system in z-direction the yields

$$H_{\mathrm{SC}} = \frac{1}{2}\sum_{k_x,k_y}\sum_{i,j} C_{i,k_x,k_y}^\dagger \mathcal{H}_{\mathrm{SC},i,j}(k_x,k_y) C_{j,k_x,k_y}, \tag{2.72}$$

where

$$\begin{aligned}\mathcal{H}_{\mathrm{SC},i,j}(k_x,k_y) = &\big[\left(Q\cos ak_x + Q\cos ak_y - \mu_{\mathrm{SC}}\right)\rho_z\sigma_0 + \mathrm{re}\Delta\rho_y\sigma_y + \mathrm{im}\Delta\rho_x\sigma_y\big]\delta_{i,j} \\ &+ \frac{Q}{2}\rho_z\sigma_0(\delta_{i,j+1} + \delta_{i,j-1})\end{aligned} \tag{2.73}$$

and

$$C_{i,k_x,k_y}^\dagger = (c_{i,k_x,k_y,\uparrow}^\dagger, c_{i,k_x,k_y,\downarrow}^\dagger, c_{i,-k_x,-k_y,\uparrow}, c_{i,-k_x,-k_y,\downarrow}). \tag{2.74}$$

The lattice indices i, j are hereby assumed to run over the entire height of the superconductor, namely from 1 to N_{SC}.
Before constructing the full model of the topological insulator–superconductor heterostructure, it is again useful to write the Hamiltonian in matrix notation rather than by summation over

Table 2.2: Parameters used for the superconductor. Unless explicitly stated otherwise, those parameters are used for all calculations involving the topological insulator–superconductor heterostructure.

Q	Δ	μ_{SC}	a	N_{SC}
2eV	10meV	3.2eV	5Å	4

the lattice indices. The Hamiltonian of equation (2.72) is thus written as

$$H_{\mathrm{SC}} = \frac{1}{2} \sum_{k_x,k_y} \vec{C}^{\dagger}_{k_x,k_y} \mathcal{H}_{\mathrm{SC}}(k_x,k_y) \vec{C}_{k_x,k_y} \tag{2.75}$$

with

$$\mathcal{H}_{\mathrm{SC}}(k_x,k_y) = \begin{pmatrix} \mathcal{H}_D^{\mathrm{SC}} & \mathcal{H}_N^{\mathrm{SC}} & & \\ \mathcal{H}_N^{\mathrm{SC}\dagger} & \mathcal{H}_D^{\mathrm{SC}} & \ddots & \\ & \ddots & \mathcal{H}_D^{\mathrm{SC}} & \mathcal{H}_N^{\mathrm{SC}} \\ & & \mathcal{H}_N^{\mathrm{SC}\dagger} & \mathcal{H}_D^{\mathrm{SC}} \end{pmatrix} \tag{2.76}$$

and

$$\vec{C}^{\dagger}_{k_x,k_y} = (c^{\dagger}_{1,k_x,k_y,\uparrow}, c^{\dagger}_{1,k_x,k_y,\downarrow}, c_{1,-k_x,-k_y,\uparrow}, c_{1,-k_x,-k_y,\downarrow}, c^{\dagger}_{2,k_x,k_y,\uparrow}, \ldots, c_{N_{\mathrm{SC}},-k_x,-k_y,\downarrow}). \tag{2.77}$$

$\mathcal{H}_D^{\mathrm{SC}}(k_x,k_y)$ describes the on-site terms, whereas $\mathcal{H}_N^{\mathrm{SC}}$ describes hopping between nearest neighbors in z-direction. We thus have

$$\mathcal{H}_D^{\mathrm{SC}}(k_x,k_y) = (A_x \cos ak_x + A_y \cos ak_y - \mu_{\mathrm{SC}})\rho_z\sigma_0 + \mathrm{re}\Delta\rho_y\sigma_y + \mathrm{im}\Delta\rho_x\sigma_y, \tag{2.78}$$

$$\mathcal{H}_N^{\mathrm{SC}} = \frac{A_z}{2}\rho_z\sigma_0. \tag{2.79}$$

We finish the introduction of the superconductor model by giving the parameters in Table 2.2. The parameters were chosen with existing regular superconductors such as lead and niobium in mind. Unless explicitly stated otherwise, it is those parameters that are used for all calculations involving the topological insulator–superconductor heterostructure.

2.2.3 Topological Insulator–Superconductor Heterostructure

Having introduced and discussed the models for both the topological insulator and the superconductor, it is time to construct the topological insulator–superconductor structure as shown in Figure 2.3. For this we only need to stack together the previously constructed Hamiltonians (2.62) for the topological insulator and (2.69) for the superconductor and ensure proper coupling between the two. For this we will use the tunneling Hamiltonian approach

$$H = H_{\mathrm{TI}} + H_{\mathrm{SC}} + H_c. \tag{2.80}$$

We deliberately denoted the tunneling Hamiltonian as H_c, as in coupling, in order to avoid confusion between H_{TI} and H_T. As we have argued in section 2.1 we should ideally include the superconducting proximity effect and calculate the decrease of the pairing amplitude self-consistently. However, we would like to point out that all energy scales involved are much larger than the maximum value of the superconducting order parameter Δ, so it is reasonable to assume that including those corrections would not give a qualitatively different result. Furthermore we are only interested in the equilibrium physics in the problem at hand. Therefore we do not need to deal with the infinite order perturbation approach which is required for the tunneling Hamiltonian to give correct results in non-equilibrium settings.
The combined Hamiltonian can best be written in matrix form as

$$H = \sum_{k_x,k_y} \vec{A}^{\dagger}_{k_x,k_y} \mathcal{H}(k_x,k_y) \vec{A}_{k_x,k_y}, \tag{2.81}$$

with

$$\vec{A}^{\dagger}_{k_x,k_y} = (b^{\dagger}_{1,k_x,k_y,+\uparrow}, b^{\dagger}_{1,k_x,k_y,+\downarrow}, \ldots, b_{N_{\mathrm{TI}},-k_x,-k_y,-\downarrow}, c^{\dagger}_{1,k_x,k_y,\uparrow}, \ldots, c_{N_{\mathrm{SC}},-k_x,-k_y,\downarrow}), \tag{2.82}$$

and

$$\mathcal{H}(k_x, k_y) = \begin{pmatrix} \mathcal{H}_D^{\mathrm{TI}} & \mathcal{H}_N^{\mathrm{TI}} & & & & & & & \\ \mathcal{H}_N^{\mathrm{TI}\dagger} & \mathcal{H}_D^{\mathrm{TI}} & & & & & & & \\ & & \mathcal{H}_D^{\mathrm{TI}} & \mathcal{H}_N^{\mathrm{TI}} & & & & & \\ & & \mathcal{H}_N^{\mathrm{TI}\dagger} & \mathcal{H}_D^{\mathrm{TI}} & \mathcal{H}_c & & & & \\ & & & & \mathcal{H}_c{}^{\dagger} & \mathcal{H}_D^{\mathrm{SC}} & \mathcal{H}_N^{\mathrm{SC}} & & \\ & & & & & \mathcal{H}_N^{\mathrm{SC}\dagger} & \mathcal{H}_D^{\mathrm{SC}} & & \\ & & & & & & & \mathcal{H}_D^{\mathrm{SC}} & \mathcal{H}_N^{\mathrm{SC}} \\ & & & & & & & \mathcal{H}_N^{\mathrm{SC}\dagger} & \mathcal{H}_D^{\mathrm{SC}} \end{pmatrix}. \tag{2.83}$$

The only new term introduced here is the coupling term $\mathcal{H}_c$, which describes direct electron transfer between topological insulator and superconductor. We again use our special notation from subsection 2.1.1 to highlight the couplings between topological insulator and superconductor as given by

$$\mathcal{H}_c = \begin{array}{c} \\ b^{\dagger}_{N_T I,k_x,k_y,+\uparrow} \\ b^{\dagger}_{N_T I,k_x,k_y,+\downarrow} \\ b^{\dagger}_{N_T I,k_x,k_y,-\uparrow} \\ b^{\dagger}_{N_T I,k_x,k_y,-\downarrow} \\ b_{N_T I,-k_x,-k_y,+\uparrow} \\ b_{N_T I,-k_x,-k_y,+\downarrow} \\ b_{N_T I,-k_x,-k_y,-\uparrow} \\ b_{N_T I,-k_x,-k_y,-\downarrow} \end{array} \begin{array}{c} \begin{array}{cccc} c_{1,k_x,k_y,\uparrow} & c_{1,k_x,k_y,\downarrow} & c^{\dagger}_{1,-k_x,-k_y,\uparrow} & c^{\dagger}_{1,-k_1,-k_y,\downarrow} \end{array} \\ \left(\begin{array}{cccc} t_1 & & & \\ & t_1 & & \\ t_2 & & & \\ & t_2 & & \\ \hdashline & & -t_1 & \\ & & & -t_1 \\ & & -t_2 & \\ & & & -t_2 \end{array}\right) \end{array}. \tag{2.84}$$

Here we have assumed the couplings t_1 and t_2 to be identical for both spins, but allow for different couplings for the different orbitals of the topological insulator. Different coupling strengths t_1 and t_2 are expected especially when different orbitals of the topological insulator are relevant around Fermi level and thus enter the effective model. In our case however the different orbitals of the topological insulator are strongly coupled to each other, as can be seen in (2.41). Additionally, t_1 and t_2 couple the different orbitals of the topological insulator to the same orbital of the superconductor. It is thus expected, and confirmed via explicit calculations, that the effects of t_1 and t_2 on the band structure of the coupled system are small and we thus use $t := t_1 = t_2$, unless noted otherwise.

2.2.4 Topological Insulator–Superconductor Heterostructure with Ferromagnetic Exchange Interaction

As discussed in section 1.4, Majorana zero modes will occur at the interface between the induced topological superconductor and a ferromagnetically gapped region. In our model we will add the ferromagnetic exchange interaction via magnetic doping of the topological insulator surface. Furthermore, we will not add a distinct ferromagnetic region, as indicated in Figure 2.8a, but instead uniformly add magnetic doping to the entire surface of the topological insulator so that the system geometry remains as depicted in Figure 2.3. Changing between regions with a gap dominated by superconducting proximity effect and a gap dominated by ferromagnetic exchange interaction can then simply be accomplished by tuning the strength of the magnetic doping. This approach allows us to keep with only one real space dimension z and keep k_x and k_y in momentum space, significantly reducing the computational complexity. In experiments this would correspond to creating many samples in which only the strength of the magnetic doping is changed. While this is of course unfeasible, the need to create arbitrarily many samples can be overcome by creating a single sample with a gradient in the magnetic doping strength. Figure 2.8b shows a doping gradient employed in y-direction, where for small y doping would be weak and the system would be in the state gapped due to superconductivity, whereas for large y doping would be strong and the system would be in the ferromagnetically gapped state. At some intermediate y_{pt} the phase transition would occur and Majorana zero modes should be located there. Focusing whatever experimental means available close to y_{pt} allows to one to not only investigate the predicted Majorana zero modes, but simultaneously the phase transition itself. In this regard using a gradient of magnetic doping can be seen as superior to the conventional approach of having clearly distinct regions of superconductivity and ferromagnetism, as it allows for further physical insight. However, it is also experimentally more demanding, as the location of the Majorana zero modes is not a priori known and creating a doping gradient brings along its own challenges. Thus, if one only aims to create Majorana zero modes and potentially use them in applications, then a system with well distinct superconducting and ferromagnetic regions may be favorable.

Having made some remarks about experimental realization of our proposal, we will next introduce the theoretical model used throughout. Adding ferromagnetic doping to the surface of the topological insulator is straight forward. The exchange interaction itself is given by

$$H_{\mathrm{ex}} = \sum_{k_x,k_y} B^{\dagger}_{N_{\mathrm{TI}},k_x,k_y} \mathcal{H}_{\mathrm{ex}} B_{N_{\mathrm{TI}},k_x,k_y}, \tag{2.85}$$

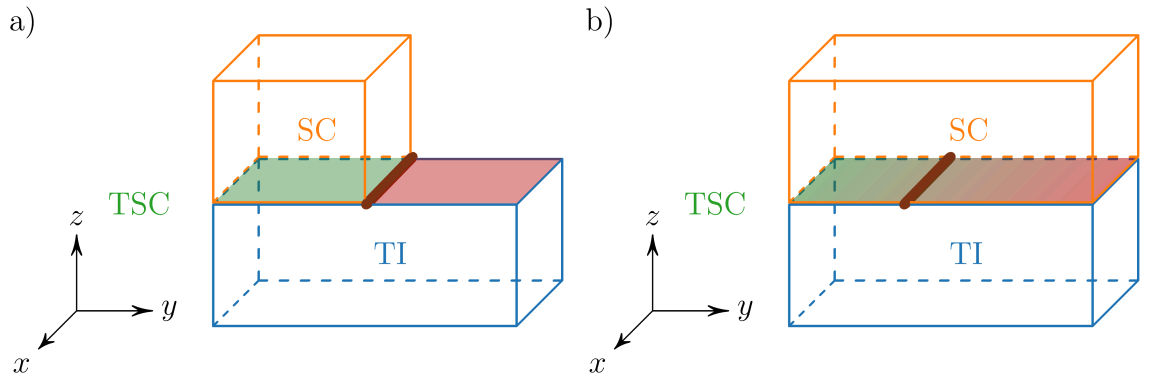

Figure 2.8: (a) Topological insulator (TI, blue) partially covered by superconductor (SC, orange). Indicated in green is the induced topological insulator (TSC) at the interface. Ferromagnetic doping is applied at the surface of the topological insulator in the red region. At the transition between the ferromagnetically doped region and the topological superconductor Majorana zero modes are predicted (thick brown line). (b) The topological insulator is entirely covered by the superconductor. However, the ferromagnetic doping at the surface of the topological insulator has a doping gradient in y-direction, ranging from weak doping for small y to strong doping for large y. Indicated by the thick brown line is the position y_{pt} where the system briefly becomes gapless and Majorana zero modes are predicted.

where $B^{\dagger}_{N_{\mathrm{TI}},k_x,k_y}$ is given by (2.58) and

$$\mathcal{H}_{\mathrm{ex}} = J\rho_z\tau_0\sigma_z, \tag{2.86}$$

where J is the strength of the ferromagnetic exchange interaction, which in turn is set by the strength of the ferromagnetic doping, and ρ, τ, σ are the Pauli matrices for particle-hole space, orbital space and spin space, respectively.
Adding the exchange interaction (2.85) to the Hamiltonian of the topological insulator–superconductor heterostructure (2.80) we obtain the Hamiltonian for the full system with variable exchange interaction as

$$H = H_{\mathrm{TI}} + H_{\mathrm{SC}} + H_c + H_{\mathrm{ex}}. \tag{2.87}$$

Having introduced the full model of the topological insulator–superconductor heterostructure including coupling and ferromagnetic doping, we would like to highlight which parameters are used to tune the model so that the migration of the Dirac cones of the topological insulator can be observed. First and foremost, we tune the coupling constant t. In experiments this would depend on the involved materials due to effects such as lattice mismatch and which orbitals are involved, as well as interface details such as impurities due to sample fabrication

process. Another important tuning parameter is the chemical potential of the superconductor, μ_{SC}. This parameter shifts around the confinement subbands of the superconductor, which influences how they can hybridize with the surface states of the topological insulator. Furthermore, we adjust the thickness of the superconductor by changing the parameter N_{SC} in order to investigate possible limitations for the thickness of the superconductor. The last very important parameter which we are tuning is the strength of the ferromagnetic exchange interaction J. Changing this parameter allows us to go from the pure topological insulator–superconductor system, where the induced gap in the surface states of the topological insulator is only due to the superconducting proximity effect, to a system with strong magnetic doping where the gap is dominated by the ferromagnetic exchange interaction. For intermediate values of J, we can see how the superconducting proximity effect and the ferromagnetic exchange interaction compensate each other, ultimately leading to a gap closing for a specific value of the exchange interaction strength J. This concludes our introduction of the topological insulator–superconductor heterostructure model with optional ferromagnetic doping, which we extensively analyze in section 3.1.

2.3 Dirac Semimetal Josephson Junction

In the following we will introduce the model of the Dirac semimetal Josephson junction. The model is an effective two band model on a tetragonal lattice, based on the low energy effective Hamiltonian around the Γ point [12, 14, 15, 70] and is essentially the same for the Dirac semimetals Cd_3As_2 and Na_3Bi, with only the parameters changing between these two materials. Higher order extensions mixing up and down spins have been proposed, but not used here due to a lack of suitable material parameters and in general not being relevant for the present analysis [71]. The model is given by

$$H = \sum_{\mathbf{k}} B_{\mathbf{k}}^{\dagger} \mathcal{H}(\mathbf{k}) B_{\mathbf{k}}, \tag{2.88}$$

with

$$B_{\mathbf{k}}^{\dagger} = (b_{\mathbf{k}+\uparrow}^{\dagger}, b_{\mathbf{k}+\downarrow}^{\dagger}, b_{\mathbf{k}-\uparrow}^{\dagger}, b_{\mathbf{k}-\downarrow}^{\dagger}). \tag{2.89}$$

Here $\uparrow$ / $\downarrow$ denotes the spin orientation, whereas $+/-$ distinguishes the orbital degree of freedom.

$$\mathcal{H}(\mathbf{k}) = \varepsilon_{\mathbf{k}} \tau_0 \sigma_0 + t \sin(k_x a) \tau_x \sigma_z - t \sin(k_y a) \tau_y \sigma_0 + m_{\mathbf{k}} \tau_z \sigma_0, \tag{2.90}$$

Table 2.3: Ab-initio parameters for Dirac semimetals Cd_3As_2 [15, 70] and Na_3Bi [14].

parameter symbol	Cd_3As_2	Na_3Bi
$\tilde{t}$[eV Å]	0.889	2.4598
$\tilde{C}_0$[eV]	−0.0145	−0.063 82
$\tilde{C}_1$[eVÅ^2]	10.59	8.7536
$\tilde{C}_2$[eVÅ^2]	11.5	−8.4008
$\tilde{m}_0$[eV]	0.0205	0.086 86
$\tilde{m}_1$[eVÅ^2]	−18.77	−10.6424
$\tilde{m}_2$[eVÅ^2]	−13.5	−10.361
a[Å]	3.0	5.448
c[Å]	5.0	9.655

where

$$\varepsilon_k = C_0 - C_1 \cos(k_z c) - C_2 \left[\cos(k_x a) + \cos(k_y a)\right], \tag{2.91}$$

$$m_{\mathbf{k}} = m_0 + m_1 \cos(k_z c) + m_2 \left[\cos(k_x a) + \cos(k_y a)\right]. \tag{2.92}$$

Here σ_i (τ_i) denotes the Pauli matrices in spin (orbital) space. The lattice constants are a and c, respectively. The hopping parameters are given by t, C_1, and C_2, with C_0 giving a constant energy shift. The remaining parameters m_0, m_1 and m_2 are due to spin-orbit coupling and lead to band inversion. The Dirac nodes are located at $\mathbf{k}_D = (0, 0, \pm k_D)$, with

$$k_D = \frac{1}{c} \arccos\left(-\frac{m_0 + 2m_2}{m_1}\right). \tag{2.93}$$

The parameters have been obtained by ab-initio calculations for the effective model [14, 15, 70]. As we will be using different lattice constants to investigate the Dirac semimetal later on, we will give the parameters of the effective model in Table 2.3 alongside their transformation rules in (2.95). In order to avoid confusion, the parameters for the effective model are written overset with a tilde ∼. The magnitude of the superconducting order parameter Δ is the same for all involved superconductors and will usually be

$$|\Delta| = 10\text{meV}, \tag{2.94}$$

unless noted otherwise.

The transformation of the coefficients from the effective low energy model to the coefficients

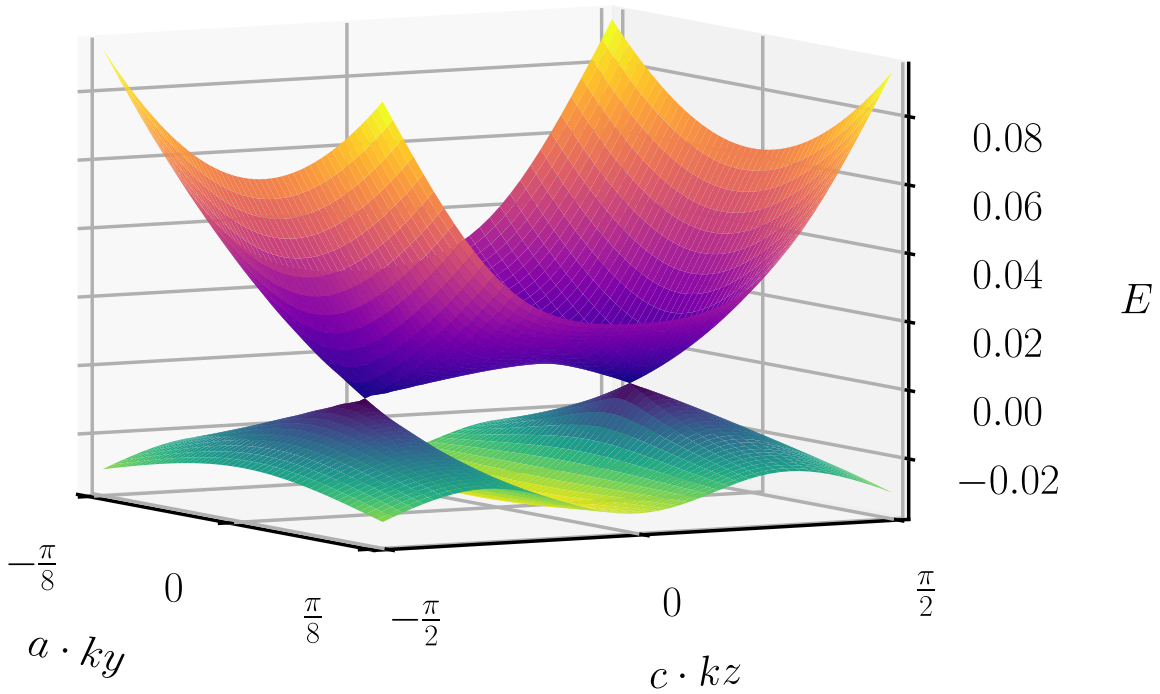

Figure 2.9: Relevant part of the band structure of Cd_3As_2 for $k_x = 0$. Two degenerate bands touching at the Dirac nodes at $\mathbf{k} = (0, 0, \pm k_D)$ can be seen.

of the lattice model is given by

$$\begin{aligned} C_0 &= \tilde{C}_0 + \frac{2\tilde{C}_1}{c^2} + \frac{4\tilde{C}_2}{a^2}, \quad C_1 = \frac{2\tilde{C}_1}{c^2}, \quad C_2 = \frac{2\tilde{C}_2}{a^2} \\ m_0 &= -\tilde{m}_0 - \frac{2\tilde{m}_1}{c^2} - \frac{4\tilde{m}_2}{a^2}, \quad m_1 = \frac{2\tilde{m}_1}{c^2}, \quad m_2 = \frac{2\tilde{m}_2}{a^2} \\ t &= \frac{\tilde{t}}{a}. \end{aligned} \tag{2.95}$$

The relevant part of the band structure of Cd_3As_2 is shown in Figure 2.9 for reference. As expected, two degenerate bands can be seen. The bands only touch at the two Dirac nodes and are otherwise well separated, as expected for an ideal Dirac semimetal. Outside the shown area the bands stay well separated.

Having discussed the model and properties of pristine Dirac semimetals, we now need to create a Josephson junction. The general setup looks like shown in Figure 2.10. The original design called for the superconductors to be directly adjacent, as the region in between superconductors does not contribute to the Josephson current and thus only increases computational complexity [13]. However, such a setup with adjacent superconductors having an independent phase of the superconducting order parameter is not physically viable, so we have opted to include in insulating gap of variable width. Changing the width of the gap allows us to in-

vestigate whether the gap has profound experimental consequences, if any. Another feature to remark is the inclusion of two Josephson junctions instead of just one. This has been done because it allows for periodic boundary conditions to be used in y-direction, avoiding possible surface contributions. Nonetheless this setup still requires all calculations being performed in two real space dimensions x and y, and only permits to use momentum space in k_z-direction. Thus it is numerically very expensive to calculate large systems. In the light of this, it is common practice to only model the topological material by a full Hamiltonian and include the superconductors only via proximity effect into the outermost layer of the topological material [2, 9, 13, 72, 73]. This is well justified in our case, as we are only interested in the Josephson current of the system, which, as seen in equation (1.35), only depends on the Hamiltonian of the weak link, the Dirac semimetal. Of course there would also be another contribution to the Josephson current via direct tunneling through the insulating gaps between the superconductors, but because this will only add a regular sine wave like 2π-periodic Josephson current on top of the skewed Josephson current mediated by the Dirac semimetal. However, this regular Josephson current needs to be taken care of in real experiments, where it will always appear and cannot simply be turned off. Another slight inaccuracy introduced by including the superconductors by proximity effect only is that the direct coupling channel from the full Dirac semimetal–superconductor system as described in section 2.1 has been completely ignored. However, this is well justified, as this direct coupling channel would only change the details of the system, but not the topological protected surface states, unless the effect is strong enough to close the band gap. The superconductor on the bottom of the Dirac semimetal does not contribute to the Josephson current and is mostly included for numerical reasons. It gaps the surface states of the bottom surface of the Dirac semimetal, which would otherwise appear in the gap of the band structure and one would have to perform additional calculations in order to determine the location of those in gap states so that one can clearly distinguish what happens at the top surface.

Having introduced the concept of the Dirac semimetal Josephson junction alongside all assumptions and justifications, all that is left to do is to Fourier transform the Hamiltonian of the bulk Dirac semimetal (2.88) in x- and y-directions, extend it to a BdG Hamiltonian and add terms for the superconducting proximity effect on the top and bottom surfaces. It seems like a rather strong assumption that the superconducting proximity effect would mostly be present in the surface and not the bulk. However, experiments with the Dirac semimetal Cd_3As_2 have confirmed that the superconducting proximity effect indeed opens a rather large superconducting gap in the surface and only a relatively small one in the bulk [23]. The procedure is the same as for the topological insulator in subsection 2.2.1 and will therefore not be reproduced in detail here. For concreteness, we assume the Hamiltonian to extend to

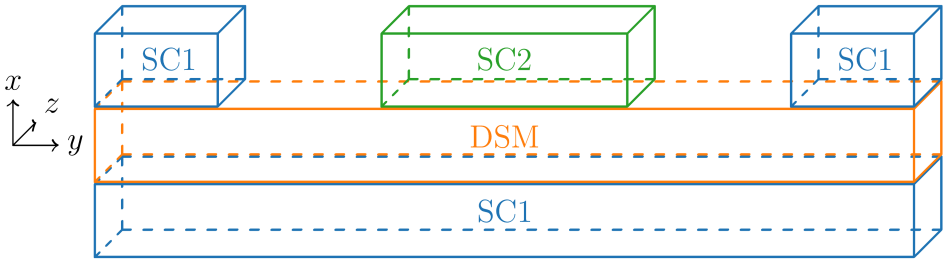

Figure 2.10: Dirac semimetal Josephson junction. Superconductors 1 (SC1) and 2 (SC2) differ only in the phase of their superconducting order parameter, not the magnitude. The Dirac semimetal (DSM) in the Josephson junction leads to a modified Josephson current, as explained in the text.

$N_x \times N_y \times N_z$ lattice sites in x-, y- and z-direction, respectively. For most calculations a lattice size on $N_x \times N_y \times N_z = 30 \times 48 \times 60$ will be chosen, unless the superconductors are physically separated. In this case the separation will be added to N_y. The Hamiltonian then reads

$$H = \frac{1}{2} \sum_{k_z} \sum_{i,j} B^\dagger_{i,k_z} \mathcal{H}_{i,j}(k_z) + \mathcal{H}_{i,j,\mathrm{SPE}} B_{j,k_z} \tag{2.96}$$

with

$$B^\dagger_{i,k_z} = (b^\dagger_{i,k_z,+\uparrow}, b^\dagger_{i,k_z,+\downarrow}, b^\dagger_{i,k_z,-\uparrow}, b^\dagger_{i,k_z,-\downarrow}, b_{i,-k_z,+\uparrow}, b_{i,-k_z,+\downarrow}, b_{i,-k_z,-\uparrow}, b_{i,-k_z,-\downarrow}). \tag{2.97}$$

i, j denote the lattice index in the x-y-plane, $\mathcal{H}_{i,j}(k_z)$ the Dirac semimetal and $\mathcal{H}_{i,j,\mathrm{SPE}}$ the contributions due to the superconducting proximity effect. The contribution of the Dirac semimetal can be given as

$$\begin{aligned}
\mathcal{H}_{i,j}(k_z) = &\left\{ \rho_z \tau_0 \sigma_0 \left[C_0 - C_1 \cos(k_z c) \right] + \rho_z \tau_z \sigma_0 \left[m_0 + m_1 \cos(k_z c) \right] \right\} \delta_{i,j} \\
&- \rho_z \tau_0 \sigma_0 \frac{C_2}{2} \delta_{i_y,j_y} \left[\delta_{i_x,j_x-1} + \delta_{i_x,j_x+1} \right] \\
&+ \rho_z \tau_z \sigma_0 \frac{m_2}{2} \delta_{i_y,j_y} \left[\delta_{i_x,j_x-1} + \delta_{i_x,j_x+1} \right] \\
&- \rho_z \tau_y \sigma_0 \frac{t}{2i} \delta_{i_y,j_y} \left[\delta_{i_x,j_x-1} - \delta_{i_x,j_x+1} \right] \\
&- \rho_z \tau_0 \sigma_0 \mu \delta_{i,j}.
\end{aligned} \tag{2.98}$$

Here i_x (i_y) denotes the x (y) component of the lattice position that the lattice index i corresponds to. Pauli matrices in particle-hole space, orbital space and spin space are denoted by ρ_i, τ_i and σ_i, respectively. The chemical potential is given by μ and all other parameters are exactly as in the bulk Dirac semimetal (2.88). Periodic boundary conditions in y-direction

can be implemented by extending the lattice to N_y+1 sites in y-direction and then identifying all lattice indices where $i_y = 1$ with $i_y = N_y + 1$.
The contribution due to the superconducting proximity effect is a bit more involved, as the phase of the superconducting order parameter $\Delta(i) = |\Delta| \exp^{i\varphi(i)}$ changes between the superconductors deposited on the surface of the Dirac semimetal and is therefore not spatially uniform. Similar to the situation in the topological insulator–superconductor system in section 2.2 the superconductor could induce both interband pairing and intraband pairing in the Dirac semimetal. However, following the earlier work on the Dirac semimetal Josephson junction we have decided to not investigate which of the two is favored and used uniform intraband pairing instead [13]. The contribution from the superconductors to the Dirac semimetal can thus be given as

$$\mathcal{H}_{i,j\mathrm{SPE}} = \big[-\rho_y\tau_0\sigma_y \mathrm{re}\Delta(i) - \rho_x\tau_0\sigma_y \mathrm{im}\Delta(i)\big]\delta_{i,j}[\delta(i_x,1) + \delta(i_x - N_x)], \tag{2.99}$$

with the space dependent superconducting order parameter given as

$$\Delta(i) = \begin{cases} |\Delta_0|, & (1 \le i_y \le y_1 \text{ or } y_4 \le i_y \le N_y) \text{ and } i_x = 1 \\ |\Delta_0| e^{i\varphi}, & y_2 \le i_y \le y_3 \text{ and } i_x = 1 \\ |\Delta_0|, & i_x = N_x \\ 0, & \text{else} \end{cases} . \tag{2.100}$$

This puts superconductor 1 uniformly on the bottom surface ($i_x = N_x$) as well as at the beginning and the end in y-direction on the top surface, between lattice coordinates $i_y = 1$ and $i_y = y_1$ as well between $i_y = y_4$ and $i_y = N_y$, as shown in Figure 2.10. Superconductor 2 gets put only on the top surface in the middle in y-direction between lattice coordinates $i_y = y_2$ and $i_y = y_3$. The gaps where there are no superconductors are simply modeled by a vanishing superconducting order parameter. Here we have arbitrarily set superconductor 1 to have a real superconducting order parameter, while the phase of the superconductor 2 can be varied by φ. This is not an undue restriction, as the Josephson current only depends on the relative phases of the superconductors.
Calculating the Josephson current in a numerical model as described above is straight forward. In order to use equation (1.35) we first need to calculate the free energy F of our system. This has been done before and the free energy can be given by [74]

$$F = -2k_BT \sum_i \ln\left(\cosh\frac{E_i(\varphi)}{2k_BT}\right), \tag{2.101}$$

where we need to sum over all the eigenvalues $E_i(\varphi)$ for a given relative phase φ between the superconductors. The Josephson current then becomes

$$I(\varphi) = 2e\frac{\partial\langle H\rangle}{\partial\varphi} = 2e\frac{\partial F}{\partial\varphi} = -2\frac{e}{\hbar}\sum_i \frac{\partial E_i(\varphi)}{\partial\varphi}\tanh\left(\frac{E_i}{2k_BT}\right), \tag{2.102}$$

where the differentiation with respect to φ obviously needs to be performed numerically. The Josephson current agrees well with previously published results, with a prefactor 2 difference arising from including the compensation 1/2 to avoid double counting in our construction of the BdG Hamiltonian [13, 75]. Note that we have opted to briefly reintroduce the constants $\hbar$ and k_B in order to emphasize the units of the resulting current and make it more easily comparable with previously published results.
The zero temperature limit $T \to 0$ of the Josephson current becomes

$$I(\varphi) = -2\frac{e}{\hbar}\sum_i \frac{\partial E_i(\varphi)}{\partial\varphi}. \tag{2.103}$$

This zero temperature limit is drastically simplified from the temperature dependent Josephson current (2.102) and thus speeds up calculations by not having to repeatedly numerically evaluate exponential functions. Though we would like to point out that the bulk of the numerical effort still remains diagonalizing the matrices in (2.96).
With this we have introduced the complete model of the Dirac semimetal Josephson junction and can proceed with calculating the Josephson current for different parameters such as gap width between the superconductors and also different Dirac semimetals.

3 Results

Having introduced the models for both the topological insulator–superconductor heterostructure and the Dirac semimetal Josephson junction, we will now present the results of our analysis. Just as before we will start by discussing our results for the topological insulator–superconductor system first and will then finish with discussing our findings in the Dirac semimetal Josephson junction system.

3.1 Induced Topological Superconductor

In the following we will present our findings of the topological insulator–superconductor heterostructure using the model which we have introduced in section 2.2. The main parameters which we will vary are the superconductor thickness N_{SC}, the chemical potential of the superconductor μ_{SC} and the coupling constant t.
Before we can investigate the relation between the Fu-Kane model of induced topological superconductors and the experiment, we need to be able to reproduce the experimental observations in our calculations. To this end we analyze the system with a thin superconductor of only $N_{\mathrm{SC}} = 4$ layers on top of the topological insulator. This is sufficiently thick for superconductivity to develop, which in extreme cases has been reported to have been observed even in single layer atomic thin films [76]. ARPES on the other hand could be able to resolve features even 4 layers deep, depending on the incident light and the specific properties of the superconductor. However, we make the simplifying assumption that ARPES measurements will only be sensitive to the top two layers of the superconductor. Thus, in order to observe the Dirac cone of the topological insulator at the free surface of the superconductor, its wave function $\psi(z)$ needs to have a significant probability density $|\psi(z)|^2$ at the outer two layers of the superconductor. In Figure 3.1 we have plotted the relevant part of the bandstructure around the Dirac cone and the localization of the center of the Dirac cone within the topological insulator–superconductor heterostructure for the two cases of no coupling $t = 0$ and strong coupling $t = 0.5\mathrm{eV}$. The chemical potential of the topological insulator (given in Table 2.1, alongside all other parameters) is chosen such that the lower Dirac cone is made from

electronic bands whereas the upper Dirac cone is made up from hole bands. As expected, in the case of no coupling, the Dirac cone is strongly localized at the outer most layer of the topological insulator, see Figure 3.1e. When turning on a comparatively strong coupling between topological insulator and superconductor, the Dirac cone moves down in energy and its localization is changed in a way that it penetrates into the superconductor all the way to the free surface, see Figure 3.1f. In this case the Dirac cone can surely be captured via ARPES measurements.

To highlight the predicted observability in ARPES measurements, we calculate the probability density in the two surface layers of the superconductor for all states, corresponding to the probability in the red boxes in Figure 3.1e and Figure 3.1f. We then plot a color coded version of the band structure using those probability densities for the shading, see Figure 3.1c and Figure 3.1d. Those graphs also correspond to what we predict to be observed in ARPES measurements, with dark regions showing very strongly, light gray regions weakly and white regions creating no signal. Comparing Figure 3.1c and Figure 3.1d we can clearly see that in the uncoupled system ARPES will not detect any Dirac node originating from the topological insulator, whereas in the strongly coupled system the Dirac node should clearly show. It shall be pointed out that the Dirac node does not penetrate any further into the topological insulator than before. This is expected, as the bulk gap of the topological insulator is rather large.

Having shown that our model is in general suited to observe the migration of the Dirac node from the surface of the topological insulator into the superconductor, we next qualitatively compare our results to the ARPES observations in experiments on a topological insulator–normal metal [10] and a topological insulator–superconductor [11]. The good qualitative agreement is explained alongside the color coded band structures in Figure 3.2. We would like to emphasize that we do not tune any parameters besides the coupling strength t and, in case of the topological insulator–normal metal system, the strength of the superconducting order parameter Δ. Nonetheless, our simple model does not only reproduce the relevant features, but also gives roughly the same energies for the Dirac nodes. Note that further improving the agreement by tuning all other model parameters seems feasible but not worth while, as the time and effort would be better spent implementing a more accurate model to begin with. Though this is outside the scope of this work.

Having confirmed that our model can reproduce experimental observations, we investigated how thickness and other parameters would affect the migration of the Dirac cones into the superconductor. Doubling the thickness of the superconductor to $N_{\mathrm{SC}} = 8$ layers requires tuning of the chemical potential of the superconductor to $\mu_{\mathrm{SC}} = 2.83\mathrm{eV}$ in order to observe the same spreading of the Dirac cone into the superconductor as for the thinner system. The

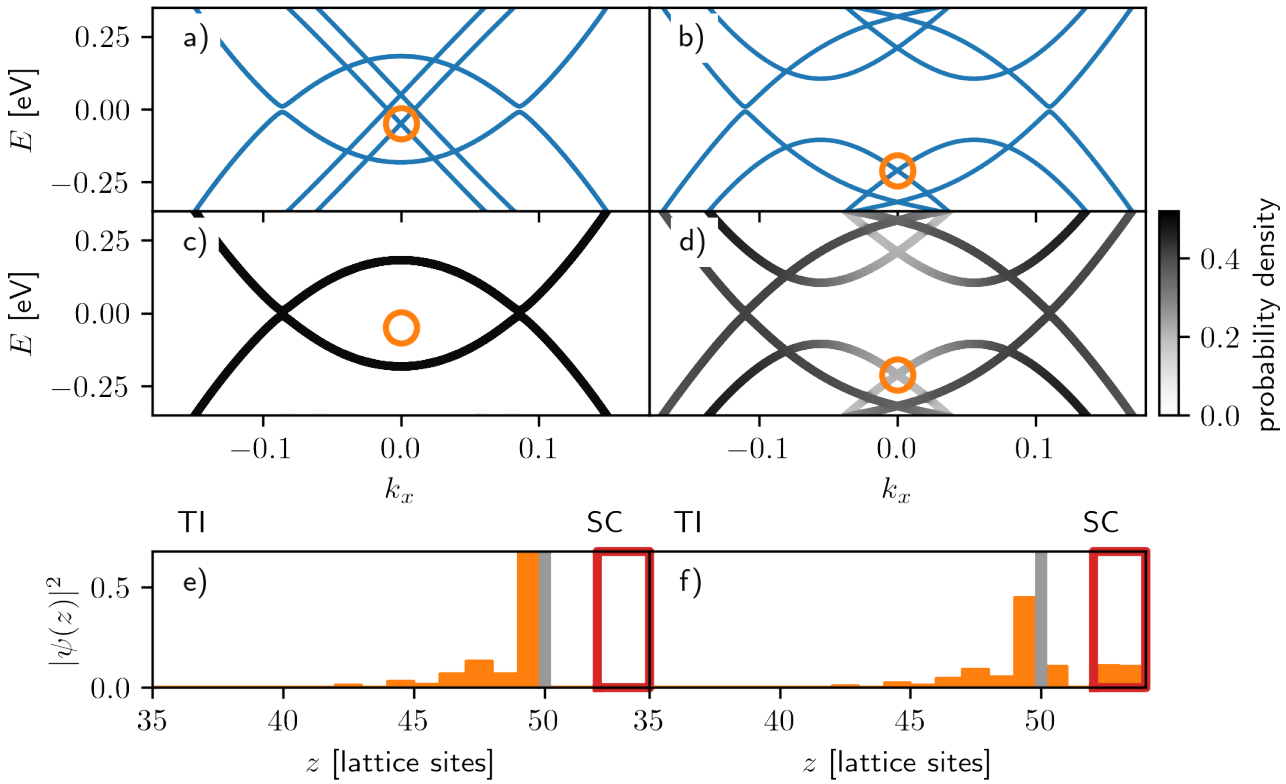

Figure 3.1: Band structure and localization of Dirac cone of the topological insulator–superconductor heterostructure with SC thickness of $N_{SC} = 4$ layers for momentum $k_y = 0$. (a), (c), (e) correspond to the uncoupled topological insulator–superconductor system with $t = 0$, whereas (b), (d), (f) correspond to a strongly coupled system with $t = 0.5$eV. (a), (b) show the band structure of the system with the orange circle highlighting the position of the electronic Dirac node. With coupling the system is now completely gapped. (c), (d) show the band structure as it would be observed in ARPES measurements. In the uncoupled system the Dirac node remains localized at the surface of the topological insulator and is thus invisible, whereas for strong coupling the Dirac node can be observed in ARPES experiments. (e) and (f) Localization of the electronic Dirac node at $k_x = k_y = 0$. Indicated by the thick gray line is the boundary between topological insulator (TI, left) and superconductor (SC, right). The red bounding box demarks the top two layers of the free surface of the superconductor, which would be observable by ARPES measurements. (e) Strong localization of Dirac node at TI interface in case of no coupling. The Dirac node would not be observed in ARPES measurements. (f) Dirac cone has significant probability density in the superconductor in case of strong coupling $t = 0.5$eV. It has significant probability density within the red bounding box, indicating that the Dirac node would be observed in ARPES measurements.

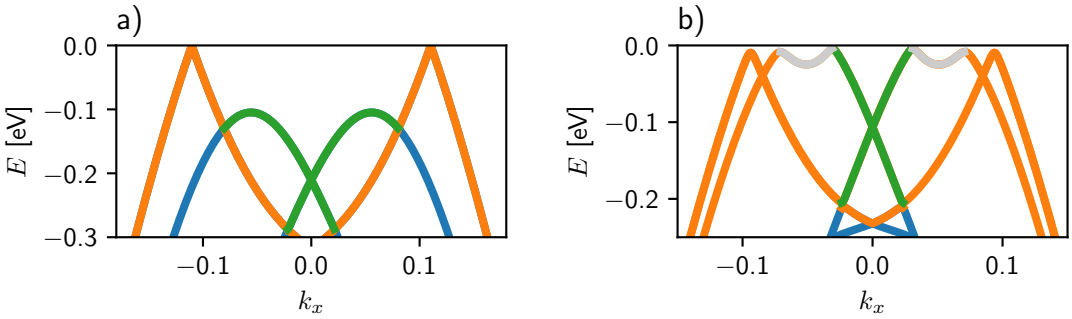

Figure 3.2: Colored band structure of a topological insulator–normal metal system (a) and a topological insulator–superconductor system (b). (a) shows the Dirac cone in green and the gapless metallic bands in orange. Note that the Dirac cone is bent over in a very similar fashion as shown in Figure 3 of Ref. [10]. Coupling strength is $t = 0.5$eV and the Cooper pair pairing potential is $\Delta = 0$. (b) shows the superconducting bands in orange and the open ended Dirac cone in green. This corresponds very well to the ARPES results shown in Figure 2 in Ref. [11]. Note that the gray bands on top are originating from the parts of the topological insulator which arise due to the introduction of particle-hole symmetry (see equation (2.55)) and thus correspond to hole bands which would not show up in ARPES experiments. Note that the system is fully gapped. The coupling strength is intermediately strong with $t = 0.25$eV.

overall bandstructure then looks comparable, as can be seen when comparing Figure 3.1b with Figure 3.3a. The Dirac cone itself also has a similar spatial distribution being spread across the entire superconductor and having some leftover localization at the interface of the topological insulator, see Figure 3.3e. Consequently, the Dirac node should be clearly visible in ARPES experiments, as shown in Figure 3.3c.

The situation drastically changes when tuning only the chemical potential of the superconductor to $\mu_{\mathrm{SC}} = 1.94\mathrm{eV}$. In this case the band structure around Fermi level looks virtually indistinguishable in the absence of coupling between topological insulator and superconductor, but the band structure and especially the state localization drastically differs when the coupling is turned to $t_1 = t_2 = 0.5\mathrm{eV}$. In this case now the Dirac node is pushed to far lower energy and it remains very strongly localized at the interface of the topological insulator, with only a very small part penetrating very weakly into the superconductor, as can be seen in Figure 3.3b and Figure 3.3f. Consequently, the Dirac cone cannot be observed in ARPES experiments, as becomes clear in Figure 3.3d.

While this might be startling and seemingly random at first sight, this situation can teach us important lessons about the conditions and the mechanism with which the Dirac cone can spread from the interface of the topological insulator into the superconductor. When we turn off the coupling ($t_1 = t_2 = 0$) and observe the states of the superconductor at $k_x = k_y = 0$ which are closest in energy, we will notice that their nature strongly changes with the chemical potential μ_{SC}. For $\mu_{\mathrm{SC}} = 2.83\mathrm{eV}$ the state is spread out across the entire superconductor, whereas for $\mu_{\mathrm{SC}} = 1.94\mathrm{eV}$ the state is strongly localized towards the center of the superconductor, as can be seen in Figure 3.3g and Figure 3.3h, respectively. This indicates that the mechanism for the Dirac cone to move into the superconductor is due to a hybridization of the surface state of the topological insulator with the confinement subband of the superconductor, which is obviously easier when the two states are spatially closer together. We furthermore learn that the spreading of the Dirac cones will not automatically happen in any system where a thin film of a superconductor is placed on top of a topological insulator. Rather, it is necessary that the right states of the superconductor are available to hybridize with the Dirac cone of the topological insulator. Luckily the right states can be tuned by only changing the chemical potential of the superconductor μ_{SC} and leaving all other system parameters identical. This observation should hopefully lead to more experimental realizations of a spreading Dirac cone in more diverse material combinations in the future.

When testing the limit of thickness of the superconductor which could be used while still observing the Dirac cones on the free surface of the superconductor, we could not determine any hard limit. In principle it should be possible to move the Dirac cones in a system with more than $N_{\mathrm{SC}} = 50$ layers of superconductor, but in this case there will be so many con-

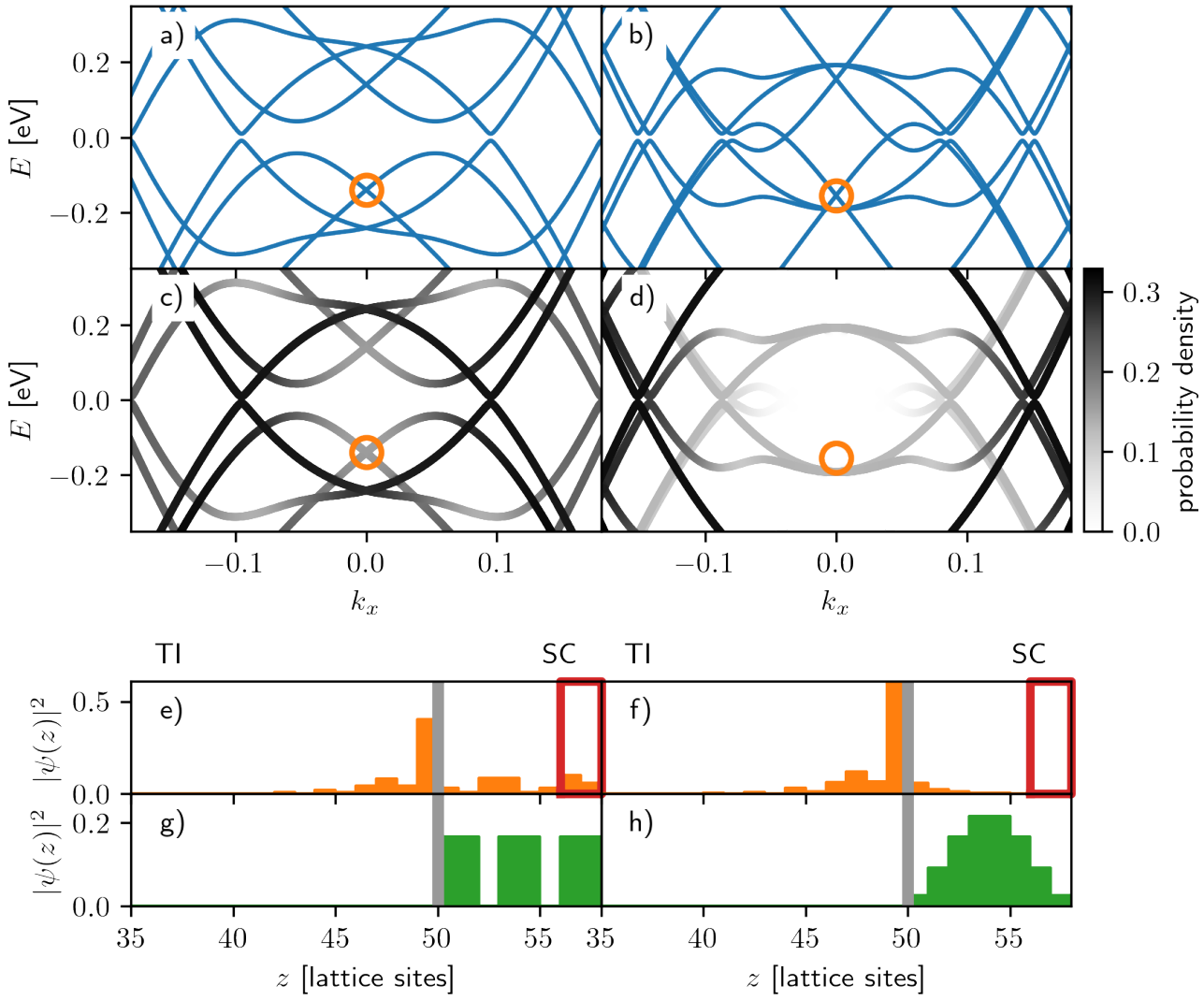

Figure 3.3: Band structure and localization of states of the topological insulator–superconductor heterostructure with superconductor thickness of 8 layers for momentum $k_y = 0$. (a), (c), (e), (g) use chemical potential for the superconductor of $\mu_{SC} = 2.83$eV, (b), (d), (f), (h) use chemical potential for the superconductor of $\mu_{SC} = 1.94$eV. (a), (b) Show the bandstructure for strong coupling $t = 0.5$eV. Indicated by the orange circle is the electronic Dirac node. In (a) the Dirac cone has perceptibly moved into the superconductor and can be observed at the free surface, as shown in the APRES-like plot (c) and as shown explicitly for the Dirac node in (e). In (b) the Dirac cone stays strongly localized at the interface of the topological insulator. Consequently, it is absent in the ARPES-like plot (d) and the Dirac node stays strongly localized at the surface of the topological insulator, as shown in (f). (g),(h) show the localization of the superconducting band in the absence of coupling ($t = 0$) at $k_x = k_y = 0$ and which is closest in energy to the Dirac cone of the topological insulator. One can clearly observe that the wave function for $\mu_{SC} = 2.83$eV spreads across the whole SC, whereas the wave function for $\mu_{SC} = 1.94$eV is localized at the center of the superconductor.

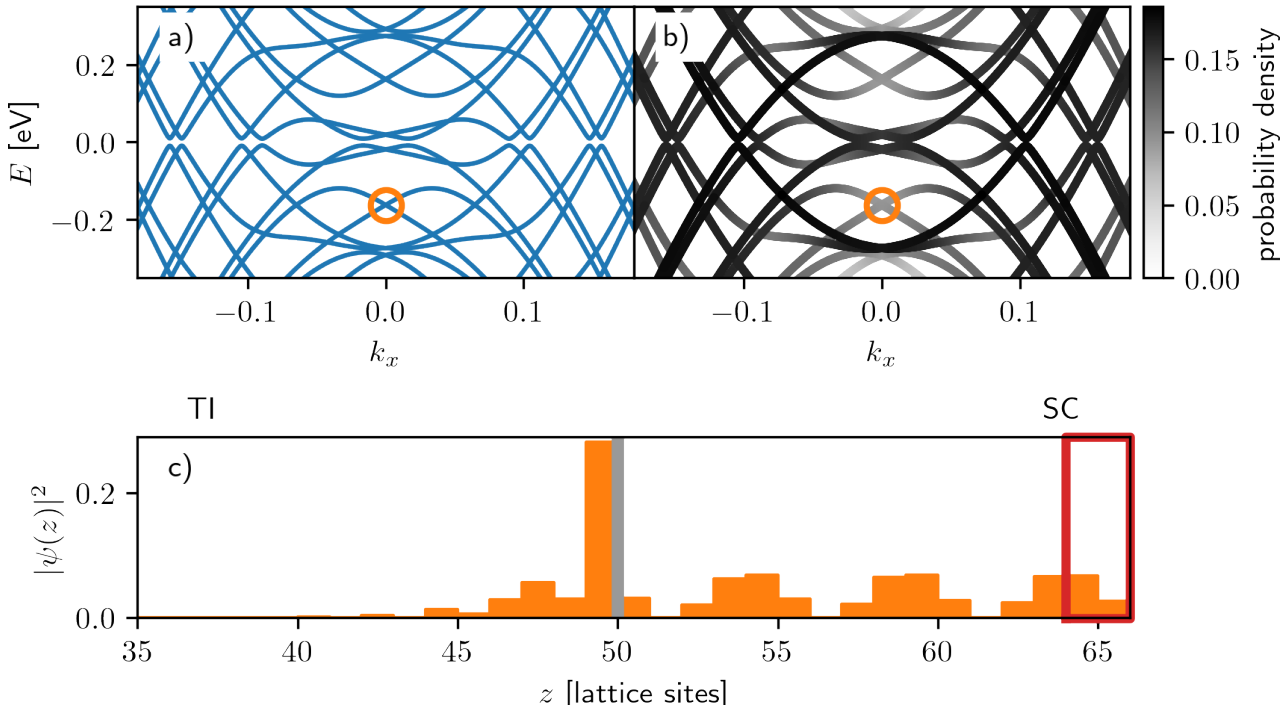

Figure 3.4: Band structure and localization of states of the topological insulator–superconductor heterostructure with a superconductor thickness of 16 layers, a chemical potential of $\mu_{SC} = 2.55$eV, coupling strength $t = 0.5$eV and momentum $k_y = 0$. (a) shows the entire band structure, (b) the band structure as it would be expected in ARPES experiments, and (c) the localization of the electronic Dirac node. One can clearly see the Dirac node extending well throughout the superconductor, but the proliferation of confinement subbands originating from the superconductor starts obscuring the view.

finement subbands that it will be difficult to distinguish the Dirac cone from all the other bands present. However, we did manage to clearly observe and distinguish the Dirac cone when using up to $N_{SC} = 16$ layers of superconductor, when tuning the chemical potential to $\mu_{SC} = 2.55$eV, as shown in Figure 3.4. Extending this to the 17 layers used in the topological insulator–superconductor experiment [11] is straight forward but has been omitted here, as no fundamental changes and new insight are expected.

A major drawback of increasing the thickness of the superconductor is a decrease of the probability density $|\psi(z)|^2$ of the Dirac cone at the free surface of the superconductor, approximately proportional to $\propto 1/z$. This is to be expected, as the Dirac cone almost evenly spreads inside the superconductor. Together with the proliferation of the confinement subbands, this sets a practical limit on the thickness of the superconductor for which reasonable experimental results can be expected. Though this strongly depends not only on the experimental method

itself, but also on the specific equipment and its capabilities, so no general statement about this practical limit can be made besides the remark that a superconductor of 17 layer thickness seems to be just fine for ARPES.

Additionally we would like to point out that the migration of the Dirac cones into a thick superconductor by itself is interesting as well. The Fu-Kane model itself only concerns itself with the two dimensional surface of the topological insulator. When the Dirac cones spread considerably into a superconductor of finite thickness one might argue that the induced superconductor itself is no longer confined to two dimensions. The implications of such a finite thickness induced topological superconductor though remain unclear for now.

Further investigations into the importance of the different system parameters did not uncover anything out of the ordinary. Changing the coupling strengths t_1 and t_2 individually hardly affects the system behavior, as can be seen in Figure 3.5. This can indeed be expected when closely analyzing the system's Hamiltonian, given in equation (2.80). The coupling term H_c couples both orbitals of the topological insulator to the same single orbital of the superconductor via t_1 and t_2, respectively. On the side of the topological insulator both orbitals are also coupled, as is evident from equation (2.41). Looking closely at multiple band structures plotted for different coupling strengths t_1 and t_2, we find that for our system there approximately exists an effective coupling strength $t_{\text{eff}} \approx \sqrt{t_1^2 + t_2^2}$. This will of course no longer hold when different materials with potentially vastly different couplings t_1 and t_2 are involved, as explained in section 2.2. Though it still gives a good justification to focus on $t = t_1 = t_2$ with our model.

Having fully understood the experimental observations and having identified the important parameters to tune in order to repeat the experiment with different materials, we will now turn our attention to bridging the gap between the theory of the induced topological superconductor and the experiment.

The important building block in the theoretical predictions of the induced topological superconductor at the interface between a topological insulator and a regular s-wave superconductor was the superconducting proximity effect. For the experiment however, and for our calculations so far, superconductivity has not played an outstanding role for the migration and observation of the Dirac cone of the topological insulator. As far as we are concerned for now, everything could have been accomplished in pretty much the same manner if we would have chosen a normal metal instead of a superconductor. Indeed, in this situation, too, the migration of the Dirac cone has been observed in experiment [10].

So in order to reveal the importance of superconductivity, we repeat our calculations for the topological insulator–normal metal system by simply turning off the superconducting pairing potential Δ. When using strong coupling of $t = 0.5$eV between the topological insula-

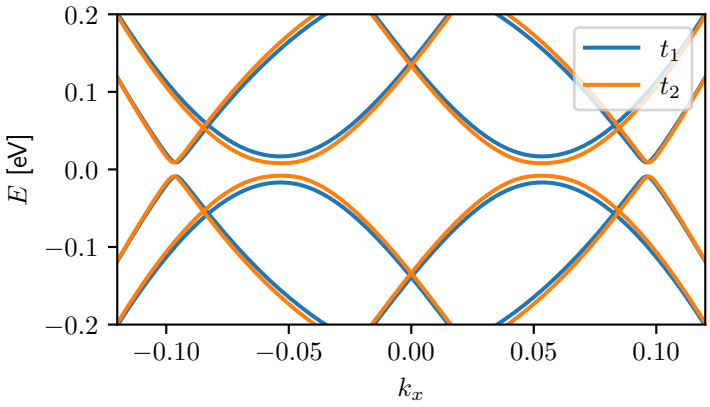

Figure 3.5: Band structure of a topological insulator–superconductor heterostructure with inequivalent coupling strengths t_1 and t_2. The blue curve (labeled t_1) is made with $t_1 = 0.46\text{eV}$ and $t_2 = 0$, the orange curve (t_2) has $t_1 = 0$ and $t_2 = 0.46\text{eV}$. Both band structure look very similar and are also very similar to a band structure with $t = t_1 = t_2 = 0.32\text{eV}$ (not shown).

tor and the normal metal the results are so strikingly similar to the topological insulator–superconductor system that we could hardly distinguish the bandstructure, except for the small superconducting gap in the superconductors' states, which is of course absent in the normal metal setup. Besides, the spreading of the Dirac cone, the dependence on the chemical potential of the normal metal μ_{NM} (as opposed to μ_{SC} for the superconductor) and the decrease of the probability amplitude $|\psi(z)|^2$ of the Dirac cone at the surface of the normal metal when increasing the metal thickness look almost identical.

The situation changes when looking at the weak coupling regime, where the coupling t is significantly smaller. In this regime, we find that the topological insulator–superconductor system slowly gaps the Dirac cone, whereas the topological insulator–normal metal system leaves the Dirac cone gapless, see Figure 3.6. It is even more interesting to slowly vary the coupling strength and see how the gap of the Dirac cone evolves, as done in Figure 3.6c. Here we can see that for small coupling the Dirac cones of the topological insulator–normal metal systems stay gapless, whereas the Dirac cones in the topological insulator–superconductor system already obtain a small gap. The Dirac cone stays mostly localized at the surface of the topological insulator in the weak coupling regime for both systems. For strong coupling the gap of the Dirac cones of both systems becomes approximately the same the gaps are opening a lot faster when increasing the coupling strength. It is also this regime when the Dirac cone moves and obtains appreciable probability density in the superconductor/the normal metal. This indicates that the gap opening mechanisms for the weak coupling regime is different than

the gap opening mechanism for the strong coupling regime. In the weak coupling regime the gap is opened in the topological insulator–superconductor system due to the superconducting gap. In the strong coupling regime however the gap is opened due to the hybridization of the Dirac cones to the confinement subbands of the superconductor/the normal metal. It is important to note that the gap of the topological insulator–superconductor system does not close when changing from the weak coupling regime to the strong coupling regime, indicating that they belong to the same topological phase.

With these results at hand, we can now bridge the gap between Fu-Kane model [9] and experiments [10, 11]. In the Fu-Kane model it has been proposed that the surface states of the topological insulator will be gapped via superconducting proximity effect of an attached superconductor, creating an induced topological superconductor. This would mean a small gap is incurred, comparable to the magnitude of the superconducting order parameter Δ. It was also predicted that the induced topological superconductor would be confined to the two dimensional region at the interface between topological insulator and superconductor. Both these predictions correspond well to the weak coupling regime of our system, where the gap of the Dirac cones is due to superconductivity, is of comparable size to the superconducting order parameter and the Dirac cone is strongly localized at the interface between topological insulator and superconductor.

The experiment on the other hand corresponds to the strong coupling regime, with the Dirac cones being observable at the free surface in both the topological insulator–superconductor case and the topological insulator–normal metal case. Our numerical simulations now show that both the weak coupling regime and the strong coupling regime of the topological insulator–superconductor heterostructure belong to the same topological phase, as there is no gap closing in between.

However, this is not conclusive proof that our model is indeed an induced topological superconductor, despite the striking similarity of the weak coupling regime with the Fu-Kane model. For conclusively showing that we have a topological superconductor we would have to calculate a relevant topological invariant. While it is not impossible to do so numerically, it does not seem very useful to do so, as it would still not allow for experimental verification of our findings. In experiments it is impossible to get access to the complete wave functions of any system, but those wave functions are required for calculating topological invariants.

Instead, we focus on properties which are experimentally accessible and investigate the arguably most interesting property of a topological insulator–superconductor heterostructure; The Majorana zero modes at the boundary to a ferromagnet.

As explained in subsection 2.2.4, we add ferromagnetic exchange interaction to our system by uniformly doping the surface of the topological insulator. By changing the strength of the fer-

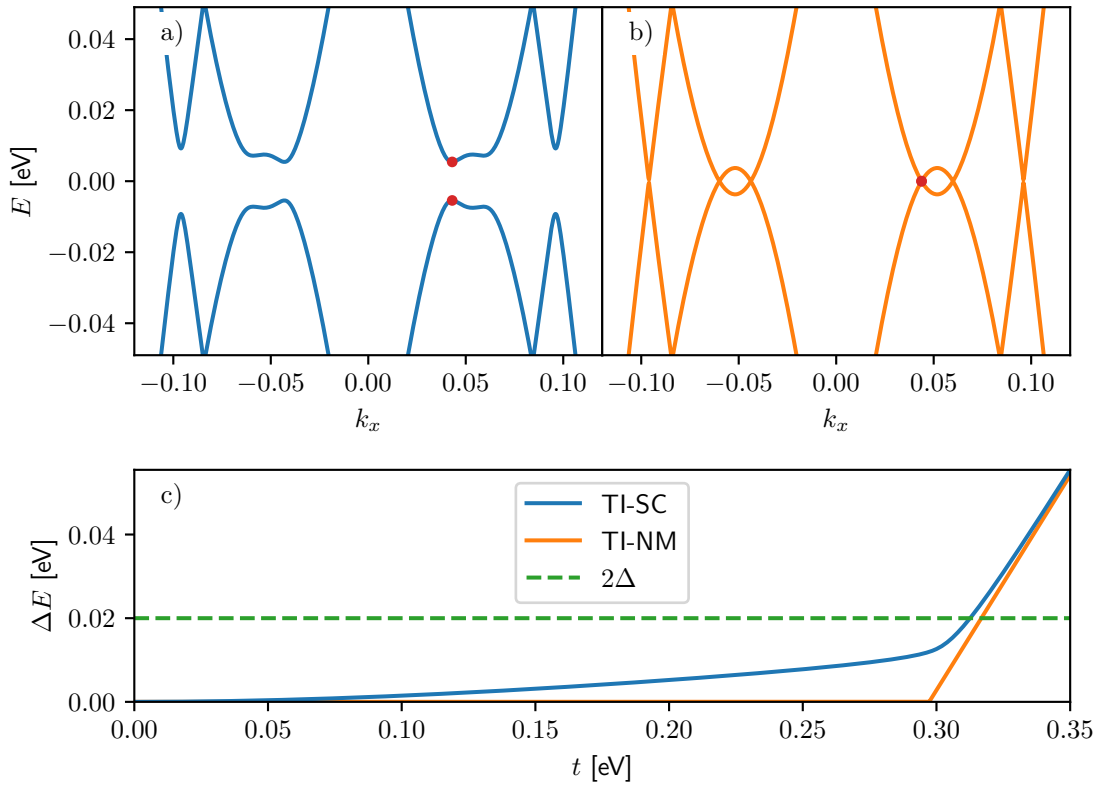

Figure 3.6: (a) Band structure of a topological insulator–superconductor heterostructure with intermediate coupling strength of $t = 0.29$eV. The Dirac cones are gapped, making the entire system gapless. The red circles indicate the momentum k_x where the gap of the Dirac cones ΔE is minimal. (b) Band structure of a topological insulator–normal metal heterostructure with intermediate coupling strength of $t = 0.29$eV. Unlike the superconducting case in (a) the Dirac cones are completely gapless, as is the entire system. The Dirac cones will gap upon increasing the coupling strength t, but the other metallic subbands will ensure that the system remains gapless. The red circles indicate the momentum k_x where the gap of the Dirac cones ΔE is minimal. (c) Gap of the Dirac cones ΔE for varying coupling strengths t for the topological insulator–superconductor system (TI-SC, blue) and the topological insulator–normal metal system (TI-NM, orange). The superconducting gap 2Δ is given by the green dashed line, for comparison. We see that the Dirac cones of the topological insulator–superconductor system are gapped for any arbitrarily small coupling strength t, whereas the Dirac cones of the topological insulator–normal metal system remain gapless until about $t \approx 0.3$eV. After this the gaps of the Dirac cones of both systems have approximately the same magnitude.

romagnetic doping and thus the strength J of the ferromagnetic exchange interaction we can switch from a system dominated by superconductivity to a system dominated by ferromagnetism. We plot the band structure of such a topological insulator–superconductor system with a fixed coupling strength of $t = 0.2\text{eV}$ for various ferromagnetic exchange interaction strengths J in Figure 3.7. In the case of vanishing exchange interaction the system behaves like before and is fully gapped with the gap of the Dirac cones being due to the superconducting proximity effect. When increasing the exchange interaction the system becomes gapless at a critical exchange interaction strength $J_c = 0.159\text{eV}$. Upon further increasing of the exchange interaction the system immediately becomes gapless again. This time however the gap of the Dirac cones is due to the ferromagnetic exchange interaction.

Repeating the process many times for different coupling strengths t allows us to trace out a phase diagram, Figure 3.7d. Here we can easily see how the regions with a superconducting dominated gap and the region with a ferromagnetically dominated gap are separated by a single phase transition line where the system becomes gapless. Stronger coupling t leads to an increased gap opening of the Dirac cones. Consequently, a stronger ferromagnetic exchange interaction is required to close the gap.

The phase diagram closely resembles what would be expected in the Fu-Kane model. In the Fu-Kane model the region with the superconducting dominated gap and the region with the ferromagnetically dominated gap are two topologically distinct gapped phases. The phase transition line is where Majorana zero modes are located in this model.

By analogy, the phase transition line in our calculations should also host Majorana zero modes. The existence of Majorana zero modes has not been calculated explicitly, as it would be of limited insight to experimental setups. Instead, the focus should be on calculating signatures of Majorana zero modes which are experimentally accessible. As explained before, potential signature to be calculated include a zero-bias tunneling conductance peak, a fractional Josephson current as well as a half-integer thermal conductance. Out of these only the thermal conductance is still considered a conclusive proof for the existence of Majorana zero modes, while the others are necessary but not sufficient signatures. Though calculating any of these signatures is outside the scope of the present work, meaning that we only have a strong indication for Majorana zero modes due to the relation to the Fu-Kane model, but not conclusive proof.

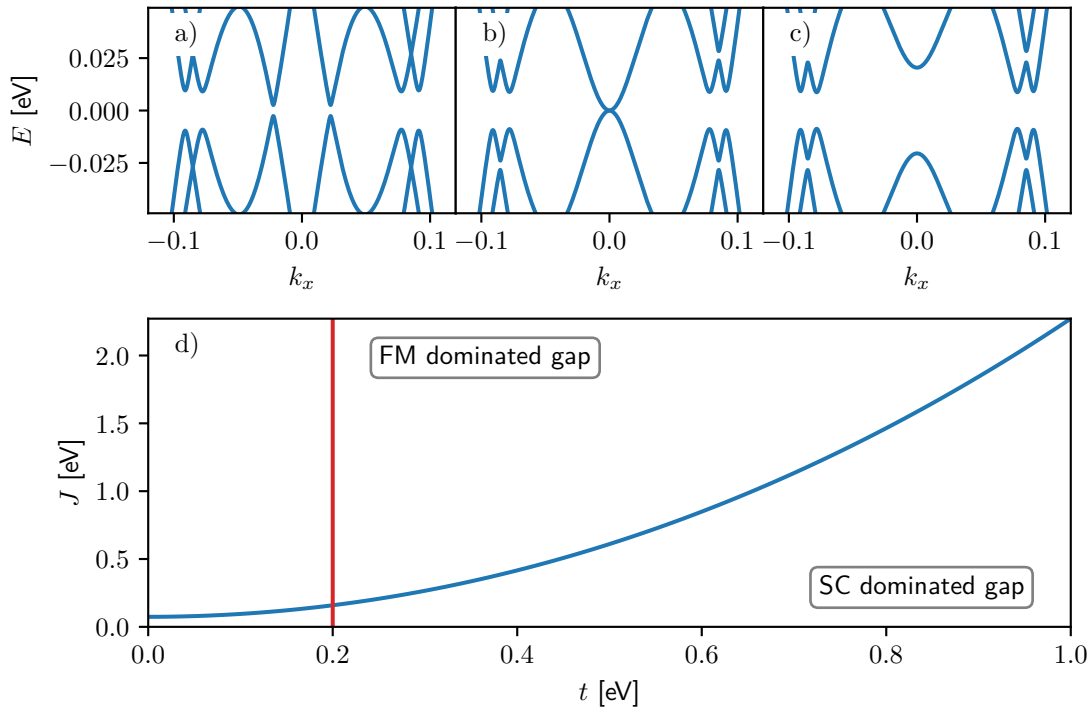

Figure 3.7: (a), (b), (c) Band structure of a topological insulator–superconductor heterostructure with coupling strength $t = 0.2$eV and various amounts of magnetic doping. (a) has no doping ($J = 0$) and the gap is due to superconductivity. (c) has strong doping and thus a ferromagnetic exchange interaction strength of $J = 0.2$eV. Here the gap of the Dirac cones is due to the ferromagnetic exchange interaction. (b) has carefully tuned ferromagnetic exchange interaction strength of $J_c = 0.159$eV. The competition between superconductivity and ferromagnetism renders the system gapless only for exactly this exchange interaction strength, as expected for a topological phase transition. (d) Phase diagram showing the region with the superconductor dominated gap well separated from the region where the gap is dominated by ferromagnetic exchange interaction. For any coupling strength t the corresponding exchange interaction strength J has been calculated for which the system becomes gapless, the phase transition line (blue line). Indicated in red is the coupling strength $t = 0.2$eV used in (a)-(c).

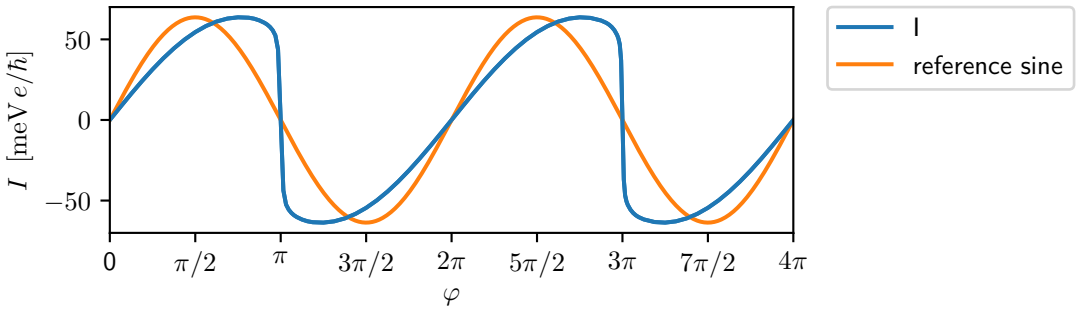

Figure 3.8: Josephson current for a Dirac semimetal Josephson junction (blue). A rather strong change in current is seen at $\varphi = \pi$, 3π, indicating the presence of Majorana zero modes. Plotted in orange is a reference sine wave which would be expected in a regular Josephson junction.

3.2 Observations in Dirac Semimetal Josephson Junctions

Having defined the complete model and setup of the Dirac semimetal Josephson junction in section 2.3, we can now calculate the Josephson current for various situations. All calculations of the Josephson currents will be performed at zero temperature using equation (2.103), unless stated otherwise. In order to check that our implementation has been implemented correctly, we will first reproduce earlier results using exactly the same parameters, which notably means that we assume our lattice to be cubic and have lattice constants of $a = c = 20$Å [13], no gaps between the superconductors and periodic boundary conditions in both z- and y-directions. The resulting Josephson current, depicted in Figure 3.8, is 2π periodic, but exhibits rather sharp jumps around $\varphi = \pi$ and $\varphi = 3\pi$. It also deviates rather strongly from a perfect sine wave as would be expected for a normal Josephson junction without Dirac semimetal and matches previously published calculations very well [13].

Having performed the calculation over an entire 4π interval for the relative phase of the superconducting order parameter φ and having seen that the Josephson current is indeed 2π periodic, albeit heavily skewed, we can restrict ourselves to a 2π interval for all subsequent calculations.

Next, we will check the influence of temperature on the Josephson current. For this we repeat the calculations of the eigenvalues of the Dirac semimetal, but this time we will use equation (2.102) to calculate the temperature dependent Josephson current. Again our results agree well with previous work, indicating the correctness of our numerical implementation [13]. As can be seen in Figure 3.9, increased temperature will smear out the pronounced jump of the Josephson current around $\varphi = \pi$, making it hard to distinguish from a regular Josephson

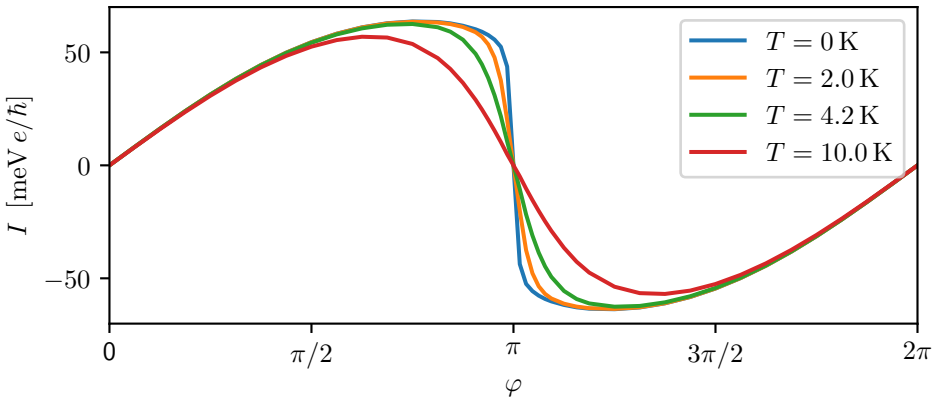

Figure 3.9: Dirac semimetal Josephson current at finite temperature. Increasing temperature smoothens the jump at $\varphi = \pi$ and makes the current look similar to a regular Josephson current.

current. However, even at the $T = 4.2\mathrm{K}$, the boiling temperature of liquid helium, a strong skewedness of the Josephson current can be observed, making it experimentally accessible.

Now that we have successfully reproduced earlier work, it is time to extend upon this and address some shortcomings. Two immediate obstacles for experimental realization come to mind: First are the immediately adjacent superconductors without any spacing in between. The second difficulty are the periodic boundary conditions in y-direction, which effectively transforms the system into an infinite superlattice.

We will start by addressing the latter issue. Removing the the periodic boundary conditions in y-direction introduces new surfaces to the Dirac semimetal and allows for an additional contributions to the Josephson current. Also, there is a bulk contribution from the bottom superconductor through the Dirac semimetal to the top superconductor, which has so far been neglected. The entirety of all contributions of the Josephson current are depicted in Figure 3.10.

The magnitude and thus importance of the additional surface contribution and the bulk contribution can be calculated when removing parts of the superconductor on top of the Dirac semimetal, as shown in Figure 3.11. In that setup, imposing periodic boundary conditions in y-direction causes only the bulk current to contribute to the Josephson current, whereas open boundary conditions add surface contributions on top. The current for both situations is shown in Figure 3.12. The bulk Josephson current closely resembles a regular sine wave, indicating that no Majorana zero modes are involved, as expected, since the bulk of the Dirac semimetal is mostly an insulator. When the periodic boundary conditions are removed and an additional surface current appears, then the Josephson current strongly increases and is

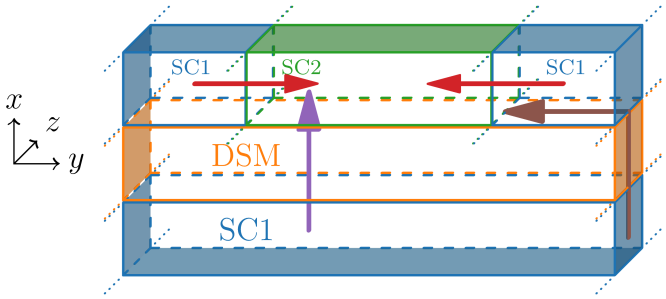

Figure 3.10: Dirac semimetal Josephson junction with periodic boundary conditions only in z-direction. Shown with red arrows is the anomalous Josephson current predicted to be caused by Majorana zero modes arising from the surface states of the Dirac semimetal. The purple arrow indicates bulk contribution through the Dirac semimetal, whereas the brown arrow introduces additional surface contribution over the x-z-side of the Dirac semimetal.

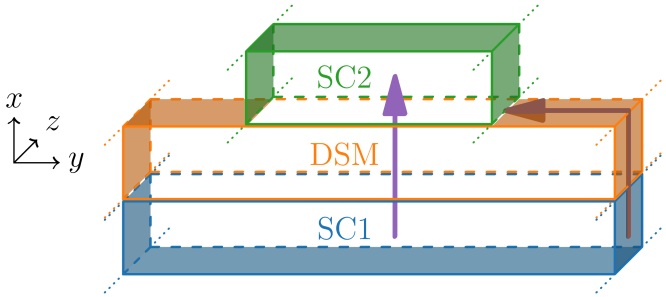

Figure 3.11: Dirac semimetal Josephson junction with only bulk current contributions (purple) if periodic boundary conditions are imposed in y-direction, and with additional surface contributions along the x-z-surface of the Dirac semimetal (brown) if not.

highly skewed. This indicates that in this case indeed Majorana zero modes are contributing to the Josephson current. This is in line with the earlier assertion in section 1.5 that the superconductors do not need to be immediately adjacent and the Majorana zero modes will simply be spread out between them. In any case, comparing with Figure 3.8 we see that both contributions are rather small and can thus be neglected to first order.

Having shown that periodic boundary conditions in y-directions are not necessary, we can simplify the setup to include only a single Josephson junction and also start investigating what happens when the superconductors on top of the Dirac semimetal get separated by an increasing insulating gap, as indicated Figure 3.13. When the gap width is increased, so is the whole system width in y-direction. This ensures that the superconductors stay a fixed size and there is no maximum limit for the gap width, besides numerical complexity.

Shown in Figure 3.14 is the Josephson current for different gap widths. Increasing the gap width reduces the Josephson current, as can be expected in any Josephson junction. The decay

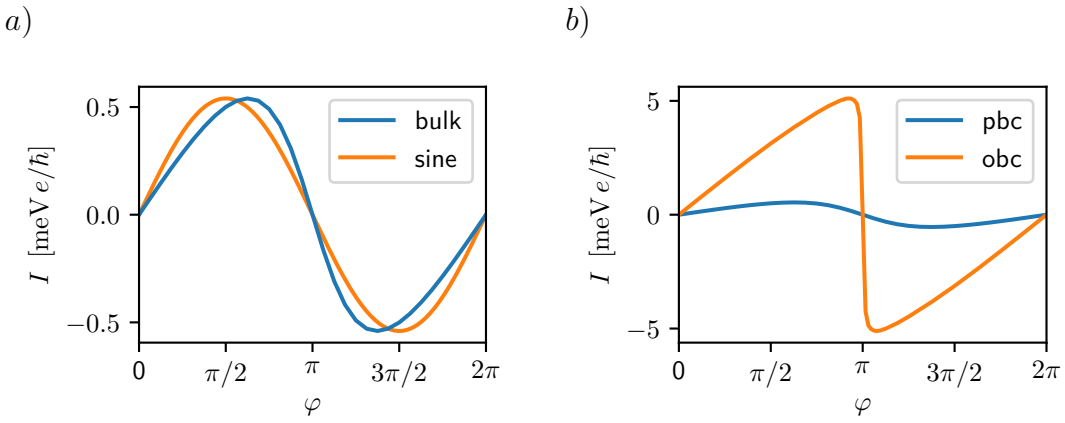

Figure 3.12: Josephson current from Dirac semimetal Josephson junction as depicted in Figure 3.11. (a) shows only the bulk contribution (blue), due to periodic boundary conditions in y-direction. It is barely deviating from a reference sine curve (orange). (b) Again shows the bulk contribution (blue) and the combined bulk and outer surface contribution (orange). The surface contribution significantly increases the Josephson current and strongly skews it, showing a strong jump at $\varphi = \pi$.

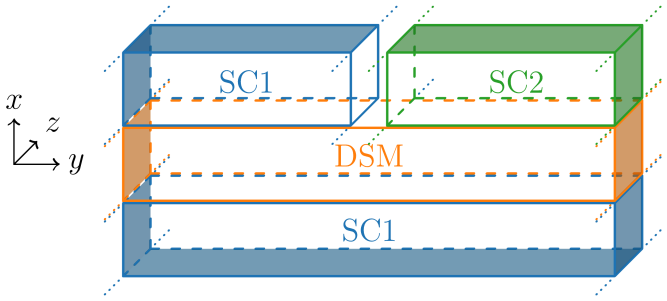

Figure 3.13: Single Dirac semimetal Josephson junction with gap of variable width between the superconductors.

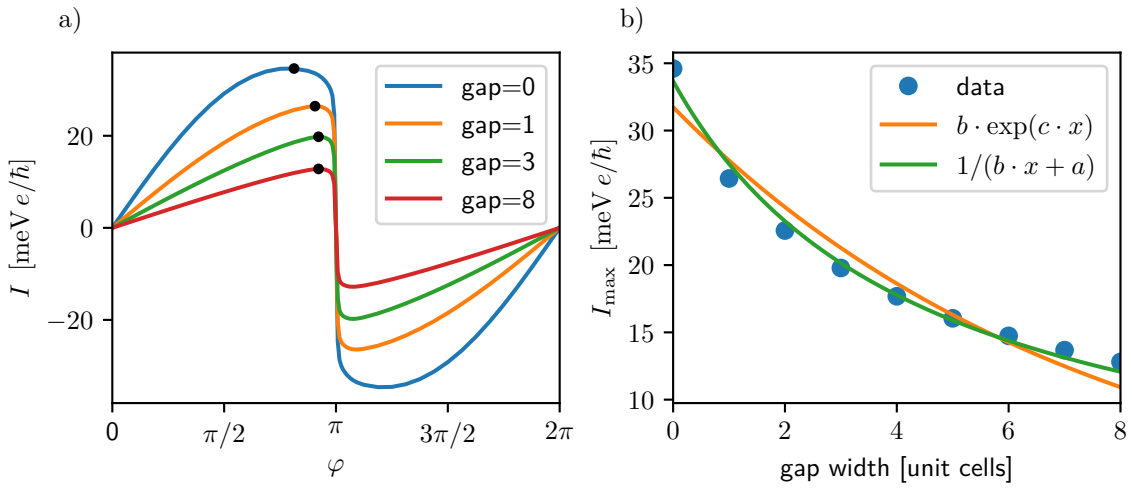

Figure 3.14: Dirac semimetal Josephson junction as shown in Figure 3.13. (a) Josephson current for different gap widths between the superconductors, in unit cells. Indicated by the black dots is the phase at which the current is maximal. (b) Evolution of the maximal Josephson current with increasing gap width. In blue are shown the actual results from the numerical calculations, whereas the orange and green curves are numerical fits to the data.

of the maximal Josephson current was investigated with different models fitted to the data, see Figure 3.14b. Models were an exponential decay be^{cx} and various non-linear approaches of the form $\frac{1}{cx^2+bx+a}$ and higher orders, where x is the gap width. It turns out that in the higher order non-linear models all coefficients in front of x^n with $n > 1$ would vanish and the best fit for the maximal Josephson current is

$$I_{\max} = \frac{1}{bx + a}. \tag{3.1}$$

This is not surprising, given the fact that the maximal current in a regular Josephson junction is defined by the critical current I_c and is proportional to $1/x$. The slight deviation from this formula as seen by the constant a in (3.1) could be due to the form of the Josephson current changing with the gap width. Alongside with the gap between the superconductors changes the relative phase φ at which the current is maximal, whereas for a regular Josephson current this maximum is always achieved at $\varphi = \pi/2$. However, more interesting seems the observation that the current actually becomes more skewed if the gap width is increased, until it resembles a sawtooth more than a skewed sine wave. This might aid in experimental observation, even though the magnitude is reduced.

Having confirmed earlier calculations and extended them towards easier experimental realization by limiting the system to a single Josephson junction and separating the superconductors with differing superconducting phase, it is now time to investigate the Josephson current in

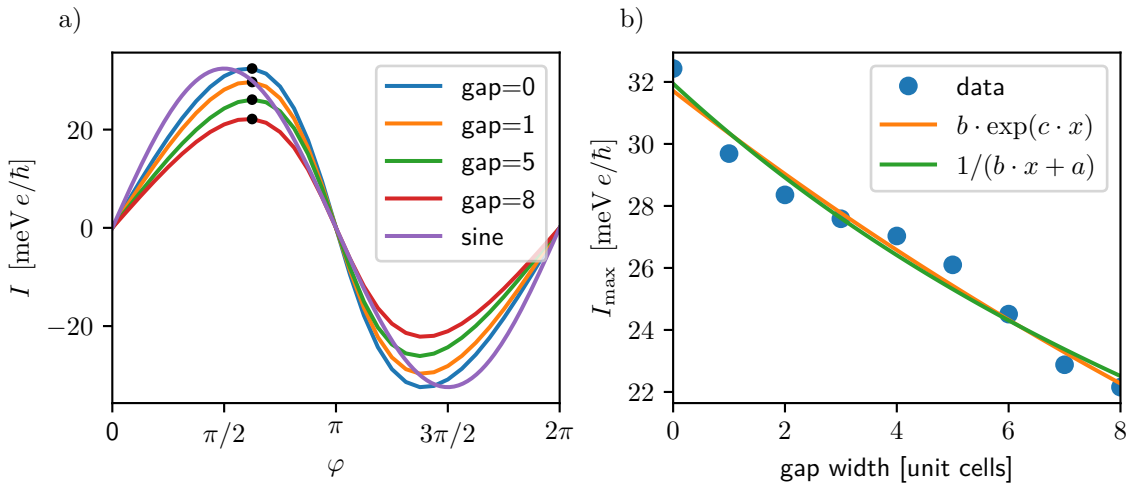

Figure 3.15: Dirac semimetal Josephson junction using Na_3Bi as Dirac semimetal. In stark contrast to the Cd_3As_2 based junction in Figure 3.14 the Josephson current here is very close to an ideal sine wave, see (a). The evolution of the maximal current with increasing gap width, as shown in (b), is very unusual and no reasonable function modeling the decay has been found.

other Dirac semimetal materials, namely Na_3Bi.

At first sight changing Cd_3As_2 to Na_3Bi seems like no big change. After all, they share the same effective Hamiltonian model, so no surprises are expected. The only thing needed to change for the calculations is to swap the parameters, as given in Table 2.3. However, the result is rather unexpected. Looking at the Josephson current in Figure 3.15a we find a current closely resembling a reference sine curve, indicating a trivial Josephson junction. Moreover, when checking how the maximum Josephson current decays (Figure 3.15), we see no clear $1/x$ decay as before.

Intrigued, we turn back to the originally proposed Cd_3As_2, however this time using realistic lattice constants of $a = 3$Å and $c = 5$Å. The result, as seen in Figure 3.16, is vastly different from what was observed before. The Josephson current now looks exactly like a regular sine wave, is vastly reduced in magnitude and the decay with increasing gap width between superconductors is highly irregular. Some reduction in the Josephson current was expected, because a smaller lattice constant c will move the Dirac nodes closer together and thus reduce the length of the Fermi arcs. In turn this leads to a reduction of the number of created Majorana zero modes, reducing the Josephson current. However, the magnitude of the reduction of the current and the irregular behavior with an increasing gap width between the superconductors is not expected. Both observations indicate that the model has reached some limitations of applicability. At this point we would like to stress that exactly the same code was used for both Figure 3.14 and Figure 3.16, with the only difference being the lattice

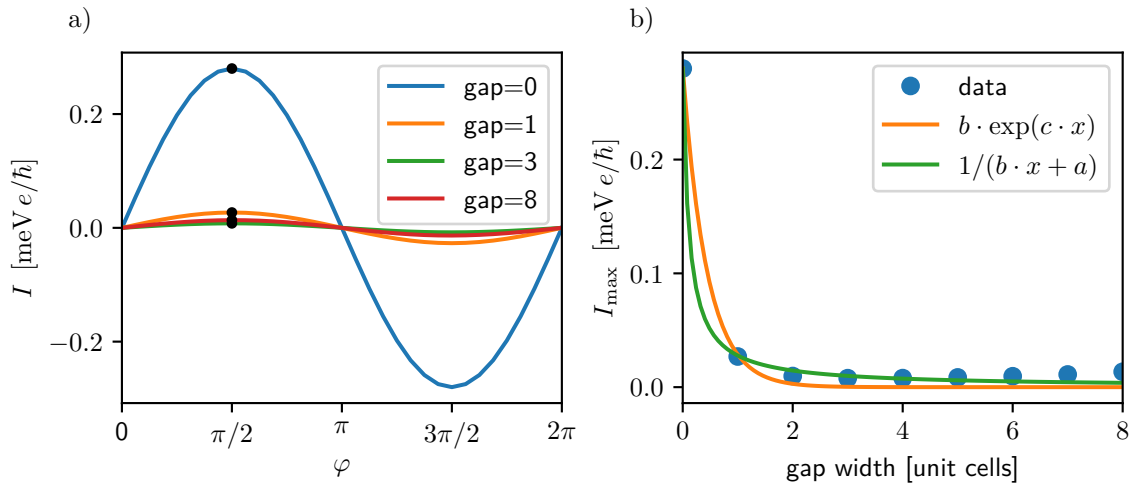

Figure 3.16: Dirac semimetal Josephson junction with Cd_3As_2 using realistic lattice constants of $a = 3$Å and $c = 5$Å. The Josephson current is very sine wave like and strongly reduced compared to the case with large lattice constants, Figure 3.14. The evolution of the maximal current with increasing gap width is also rather unusual.

constants and consequently the parameters, which are derived from the effective low energy Hamiltonian with the lattice constants.

Further investigation revealed that this strong change in behavior is dependent only on the lattice constant a, but not on c. A known issue in these kind of calculations can be that changing the physical size of the sample can introduce some changes such as hybridization. The physical size of the sample changes when the number of unit cells is kept constant while the lattice constant is modified. The sample size in x-direction for example is given by $L_x = N_x \cdot a$, with N_x the number of unit cells in x-direction and a the corresponding lattice constant. We have thus calculated the Josephson current for constant physical size but differing lattice constants and number of unit cells and have come to the conclusion that the physical sample size is not the root cause of the issue, but rather the lattice constant a itself. This is very surprising, as the lattice constant a does not affect the position of the Dirac nodes, unlike lattice constant c. Therefore it seems unlikely that the Majorana zero modes would be affected by a change in a.

As final investigation into whether Majorana zero modes are at the origin of the irregular Josephson current, or whether there are other, so far overlooked mechanisms at play, we have decided to investigate the system outside of the validity range of the prediction. As explained in section 1.5, the entire assumption of having an effective two dimensional Hamiltonian describing solely the surface states of the Dirac semimetal holds only sufficiently far away from the Dirac nodes and when the induced superconducting pairing potential is sufficiently weak,

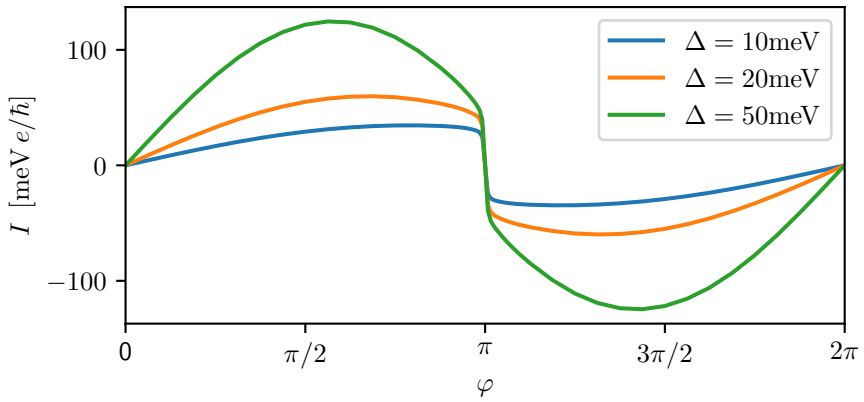

Figure 3.17: Increased pairing potential Δ in a Dirac semimetal Josephson junction leads to a higher and more sine wave like Josephson current, but a strong jump around $\varphi = \pi$ persists.

see equation (1.47). Calculating the Fermi velocity in z-direction at the Dirac nodes is straight forward and yields

$$v = \left| \frac{\partial}{\partial k_z} \mathcal{H}(\mathbf{k}) \Big|_{\mathbf{k}=\mathbf{k}_D} \right| = \left| 2(\tilde{c}_1 - \tau_z \tilde{m}_1) \sqrt{-\frac{c^2}{4} \frac{\tilde{m}_0^2}{\tilde{m}_1^2} - \frac{\tilde{m}_0}{\tilde{m}_1}} \right| . \tag{3.2}$$

Using the large lattice constants $a = c = 20$Å where a strongly skewed Josephson current has been observed, we get Fermi velocities of

$$v_+ = 1.83\text{eV Å} \tag{3.3}$$
$$v_- = 0.51\text{eV Å}, \tag{3.4}$$

for the two orbitals, respectively. Making use of the fact that there are only Fermi arcs between the projections of the Dirac cones $-k_D < k_z < k_D$ we can approximate the condition (1.47) to

$$v|k_D - |k_z|| \leq v_z k_D = 17.2\text{meV}. \tag{3.5}$$

Thus choosing an induced pairing potential Δ of larger than 17.2meV the original condition under which Majorana zero modes were predicted to exist is never fulfilled for any k_z. Nonetheless, we find that even for significantly increased pairing amplitude there remains a steep jump of the Josephson current close to a relative phase $\varphi = \pi$, see Figure 3.17. The height of the jump stays largely unchanged, but the maximum of the Josephson current shifts towards the regular value of $\varphi = \pi/2$ for an increased pairing amplitude.

All these findings indicate that Majorana zero modes are not the main driver of the highly skewed Josephson current which has been observed. However, we would like to point out that it is entirely possible that Majorana zero modes and other mechanisms causing a highly skewed Josephson current could coexist. Also, it cannot be ruled out that the simplifications made in the model interfere with the Majorana zero modes, which were predicted by using only analytical means.

4 Conclusion

In this last chapter we will briefly recall what we have learned and discovered in both, the topological insulator–superconductor system as well as the Dirac semimetal Josephson junction. We will discuss the implications of our results for the ongoing quest of observing Majorana zero modes in experiments. Finally we will give suggestions for further investigations to eventually realize irrefutable experimental evidence of Majorana zero modes.

4.1 Topological Insulator–Superconductor Heterostructure

We start our conclusion by discussing our findings in the topological insulator–superconductor heterostructure. While there has been ample theoretical research on topological material–superconductor systems, most of that research includes the superconductor only via superconducting proximity effect, often only considering the interface layer to begin with [2, 9, 12, 13, 72, 73, 77, 78]. Though we should point out that notable exceptions exist, when analytical calculations are feasible and the wave matching approach can be employed [79]. Using a full tight-binding Hamiltonian including both topological material and superconductor to investigate topological effects however seems significantly less common.
In our work we have successfully used a full effective tight-binding Hamiltonian including both topological insulator and superconductor to achieve two goals.
For one we have been able to determine the conditions under which the Dirac cone from the topological insulator becomes observable at the free surface of the superconductor, as shown previously in experiment [11]. It turns out that there are two important ingredients to make this happen. First, we need sufficiently strong coupling between topological insulator and superconductor. Otherwise the Dirac cone will stay strongly localized at the interface of the topological insulator. Second, we need to tune the chemical potential of the superconductor. With this we were able to ensure that the correct states from the superconductor are available at the topological insulator interface for the Dirac cone to hybridize with. With these two ingredients experimentalists should find it easier to prepare other systems where the surface states of a topological material will spread into the superconductor, opening them up for direct

experimental observation.

Our second achievement was to gap the bridge between theory and experiment. Theoretical investigations predicted an induced topological superconductor at the interface between a topological insulator and a superconductor, the so-called Fu-Kane model [9]. This is predicted to be caused by the superconducting proximity effect. Calculations in our model show that this situation corresponds to the weak coupling regime. In this regime the driving force behind the gap opening of the surface states of the topological insulator is the superconducting order. Just as assumed by the Fu-Kane model, the surface states of the topological insulator stays strongly localized in this weak coupling regime. Experimental observations of the Dirac cone from the topological insulator at the free surface of the superconductor however correspond to the strong coupling regime. In this regime the gap opening of the surface states of the topological insulator is driven by hybridization with the confinement subbands of the superconductor, as we have seen from the comparison with the topological insulator–normal metal system. Our calculations show that the weak coupling regime and the strong coupling regime correspond to the same topological phase, as there is no gap closing when smoothly changing between these two. This indicates that the induced topological insulator does not need to be confined to the two dimensional interface between topological insulator and superconductor, but can well extend into the third dimension, turning the entire superconducting film into a topological superconductor. Our results further indicate that the Dirac cones observed in experiment indeed belonged to a topological superconductor.

While those findings match well with both the Fu-Kane model and the experimental results and indicate that we have a finite thickness induced topological superconductor, we would like to point out that this is not yet conclusive proof that there is indeed a topological superconductor phase. In order to substantiate our results, we investigated whether we would get a gap closing when adding ferromagnetic doping, as would be expected from the Fu-Kane model. Indeed, adding variable strength ferromagnetic exchange interaction via doping of the surface of the topological insulator allowed us to create a phase where the gap of the Dirac cone is due to the ferromagnetic exchange interaction. This phase is separated from the original phase with a superconducting dominated gap by a single gap closing, indicating that we have two different topological phases.

Predicted by the Fu-Kane model is the existence of Majorana zero modes at the phase transition between the superconducting dominated region and the ferromagnetically dominated region. While we have not performed any explicit calculations to confirm the existence of Majorana zero modes in our model, the striking similarity with the Fu-Kane model is a good indicator that Majorana zero modes are also present in our case. Tough for a conclusive and experimentally accessible proof we would have to calculate the thermal conductance of our

system. Finding a half integer quantized thermal conductance would then unambiguously confirm the existence of Majorana zero modes in our simple topological insulator–superconductor model.
Another even more direct verification of Majorana zero modes would be to explicitly show their non-Abelian behavior by creating multiple such modes and moving them around each other. This could be achieved by using locally controllable ferromagnetic insulators, external magnetic fields or even by locally heating the superconductor in order to lower its superconducting order parameter. The latter approach would even be compatible with the ferromagnetic doping of the topological insulator, as used in our model. If the ferromagnetic doping is chosen such that the exchange interaction is weak enough for the system to be in the superconducting dominated phase when at zero temperature, but strong enough that we transition to the ferromagnetically dominated phase when heating just below the superconducting phase transition temperature where the superconducting order parameter is significantly reduced, then we could create arbitrary geometries of superconducting dominated and ferromagnetically dominated phases and thus manipulate the Majorana zero modes. Tough it should be pointed out that all these approaches will need a full three dimensional simulation entirely in real space, making it computationally very expensive. Even more so when a more realistic model for the topological insulator–superconductor heterostructure is used, taking into account effects such as lattice mismatch and temperature.
Despite all this, it is remarkable how our very simple tight-binding model can qualitatively reproduce experimental observations and at the same time allows to establish the connection between these experiments and the influential Fu-Kane model.

4.2 Dirac Semimetal Josephson Junction

After having introduced and investigated the Dirac semimetal Josephson junction in detail, it is time to highlight our findings and comment on the applicability of such system for realizing Majorana zero modes. Earlier works have given good theoretical arguments why Weyl semimetal and Dirac semimetal Josephson junctions should host Majorana zero modes [12]. Subsequent numerical investigations were quite promising and showed a clear signature of a fractional Josephson effect, as would be expected from for example Majorana zero modes [13]. The simplifications made to lower the numerical burden were justified and in general do not turn out to be problematic. Within these simplifications we have been able to closely reproduce earlier results and extend upon them in order to improve experimental feasibility. To this end we were able to show that it is not necessary to construct a superlattice by imposing

periodic boundary conditions, explicitly showed that additional bulk or surface contributions are negligible and most importantly that separating the superconductors by insulating regions does not adversely affect observability of the fractional Josephson current.
However, what was thought to be an easy extension to another Dirac semimetal and the change to more realistic material parameters turned out to drastically change the results. While we have not been able to pinpoint the origin of this unexpected behavior, the results do indicate that something else is happening and it may well be that the observed fractional Josephson current is due to a different mechanism. Other mechanisms leading to a fractional Josephson current such as quantum point contacts are known to exist and may occur simultaneously with the fractional Josephson current induced by Majorana zero modes. Thus while Majorana zero modes make a very compelling case for being responsible for the observed fractional Josephson current for some parameter range it should be investigated which other mechanism could yield the same or at least similar effect.
Despite these findings, especially with the difficulties encountered when using more realistic material parameters, we would like to point out that a highly skewed Josephson current is nonetheless a very useful feature of Majorana zero modes. While it has since been shown that Majorana zero modes are not the only way to create a 4π periodic Josephson current, let alone a skewed 2π periodic Josephson current, it is still an important experimental feature of Majorana zero modes. If one can exclude other mechanisms being responsible for the skewed Josephson in Dirac semimetal Josephson junctions, or find a different way to prove the existence of Majorana zero modes in these systems, then the skewed Josephson current can still be an additional tool for verifying both numerical calculations and experimental observations. Though as it stands for now, Dirac semimetal Josephson junctions are not a prime candidate for experimentally proving the existence of Majorana zero modes in an irrefutable way.

5 Bibliography

[1] X.-L. Qi, Y.-S. Wu, and S.-C. Zhang, Physical Review B **74**, 085308 (2006).

[2] X.-L. Qi, T. L. Hughes, and S.-C. Zhang, Physical Review B **82**, 184516 (2010).

[3] K.-Y. Yang, Y.-M. Lu, and Y. Ran, Physical Review B **84**, 075129 (2011).

[4] C. Nayak, S. H. Simon, A. Stern, M. Freedman, and S. D. Sarma, Reviews of Modern Physics **80**, 1083 (2008).

[5] A. R. Akhmerov, J. Nilsson, and C. W. J. Beenakker, Physical Review Letters **102**, 216404 (2009).

[6] J. Alicea, Y. Oreg, G. Refael, F. von Oppen, and M. P. A. Fisher, Nature Physics **7**, 412 (2011).

[7] A. Y. Kitaev, Physics-Uspekhi **44**, 131 (2001).

[8] J. Alicea, Reports on Progress in Physics **75**, 076501 (2012).

[9] L. Fu and C. L. Kane, Physical Review Letters **100**, 096407 (2008).

[10] T. Shoman, A. Takayama, T. Sato, S. Souma, T. Takahashi, T. Oguchi, K. Segawa, and Y. Ando, Nature Communications **6**, 10.1038/ncomms7547 (2015).

[11] C. X. Trang, N. Shimamura, K. Nakayama, S. Souma, K. Sugawara, I. Watanabe, K. Yamauchi, T. Oguchi, K. Segawa, T. Takahashi, Y. Ando, and T. Sato, Nature Communications **11**, 159 (2020).

[12] A. Chen and M. Franz, Physical Review B **93**, 201105 (2016).

[13] A. Chen, D. I. Pikulin, and M. Franz, Physical Review B **95**, 174505 (2017).

[14] Z. Wang, Y. Sun, X.-Q. Chen, C. Franchini, G. Xu, H. Weng, X. Dai, and Z. Fang, Physical Review B **85**, 195320 (2012).

[15] Z. Wang, H. Weng, Q. Wu, X. Dai, and Z. Fang, Physical Review B **88**, 125427 (2013).

[16] M. Neupane, S.-Y. Xu, R. Sankar, N. Alidoust, G. Bian, C. Liu, I. Belopolski, T.-R. Chang, H.-T. Jeng, H. Lin, A. Bansil, F. Chou, and M. Z. Hasan, Nature Communications **5**, 3786 (2014).

[17] S. Borisenko, Q. Gibson, D. Evtushinsky, V. Zabolotnyy, B. Büchner, and R. J. Cava, Physical Review Letters **113**, 027603 (2014).

[18] Z. K. Liu, B. Zhou, Y. Zhang, Z. J. Wang, H. M. Weng, D. Prabhakaran, S.-K. Mo, Z. X. Shen, Z. Fang, X. Dai, Z. Hussain, and Y. L. Chen, Science **343**, 864 (2014).

[19] T. Morimoto and A. Furusaki, Physical Review B **89**, 235127 (2014).

[20] M. Kargarian, M. Randeria, and Y.-M. Lu, Proceedings of the National Academy of Sciences **113**, 8648 (2016).

[21] C. Zhang, A. Narayan, S. Lu, J. Zhang, H. Zhang, Z. Ni, X. Yuan, Y. Liu, J.-H. Park, E. Zhang, W. Wang, S. Liu, L. Cheng, L. Pi, Z. Sheng, S. Sanvito, and F. Xiu, Nature Communications **8**, 1272 (2017).

[22] M. Uchida, Y. Nakazawa, S. Nishihaya, K. Akiba, M. Kriener, Y. Kozuka, A. Miyake, Y. Taguchi, M. Tokunaga, N. Nagaosa, Y. Tokura, and M. Kawasaki, Nature Communications **8**, 10.1038/s41467-017-02423-1 (2017).

[23] C. Huang, B. T. Zhou, H. Zhang, B. Yang, R. Liu, H. Wang, Y. Wan, K. Huang, Z. Liao, E. Zhang, S. Liu, Q. Deng, Y. Chen, X. Han, J. Zou, X. Lin, Z. Han, Y. Wang, K. T. Law, and F. Xiu, Nature Communications **10**, 10.1038/s41467-019-10233-w (2019).

[24] D.-H.-M. Nguyen, K. Kobayashi, J.-E. R. Wichmann, and K. Nomura, Physical Review B **104**, 045302 (2021).

[25] G. Kells, D. Meidan, and P. W. Brouwer, Physical Review B **86**, 100503 (2012).

[26] E. J. H. Lee, X. Jiang, R. Aguado, G. Katsaros, C. M. Lieber, and S. D. Franceschi, Physical Review Letters **109**, 186802 (2012).

[27] K. Laubscher and J. Klinovaja, Journal of Applied Physics **130**, 081101 (2021).

[28] C.-K. Chiu and S. D. Sarma, Physical Review B **99**, 035312 (2019).

[29] K. Nomura, S. Ryu, A. Furusaki, and N. Nagaosa, Physical Review Letters **108**, 026802 (2012).

[30] H. Sumiyoshi and S. Fujimoto, Journal of the Physical Society of Japan **82**, 023602 (2013).

[31] Y. Huang, F. Setiawan, and J. D. Sau, Physical Review B **97**, 100501 (2018).

[32] J. Bardeen, L. N. Cooper, and J. R. Schrieffer, Physical Review **106**, 162 (1957).

[33] J. Bardeen, L. N. Cooper, and J. R. Schrieffer, Physical Review **108**, 1175 (1957).

[34] H. Bruus and K. Flensberg, *Many-body quantum theory in condensed matter physics - an introduction*, English (Oxford University Press, United States, 2004).

[35] Y. Asano, *Andreev reflection in superconducting junctions* (Springer Singapore, 2021).

[36] A. Altland and B. D. Simons, *Condensed matter field theory* (Cambridge University Press, 2009).

[37] J. R. Schrieffer, *Theory of superconductivity* (1999).

[38] J. Bardeen, Physical Review Letters **9**, 147 (1962).

[39] G. E. Blonder, M. Tinkham, and T. M. Klapwijk, Physical Review B **25**, 4515 (1982).

[40] B. Pannetier and H. Courtois, Journal of Low Temperature Physics **118**, 599 (2000).

[41] J. C. Cuevas, A. Martín-Rodero, and A. L. Yeyati, Physical Review B **54**, 7366 (1996).

[42] S. Lee, V. Stanev, X. Zhang, D. Stasak, J. Flowers, J. S. Higgins, S. Dai, T. Blum, X. Pan, V. M. Yakovenko, J. Paglione, R. L. Greene, V. Galitski, and I. Takeuchi, Nature **570**, 344 (2019).

[43] W. Belzig, F. K. Wilhelm, C. Bruder, G. Schön, and A. D. Zaikin, Superlattices and Microstructures **25**, 1251 (1999).

[44] M. Tinkham, *Introduction to superconductivity*, Second edition, Dover Books on Physics Series (Dover Publications, 2004).

[45] A. Zagoskin, *Quantum theory of many-body systems* (Springer International Publishing, 2014).

[46] P. Szabó, T. Samuely, V. Hašková, J. Kačmarčík, M. Žemlička, M. Grajcar, J. G. Rodrigo, and P. Samuely, Physical Review B **93**, 014505 (2016).

[47] F. š. Herman and R. Hlubina, Physical Review B **94**, 144508 (2016).

[48] M. H. Cohen, L. M. Falicov, and J. C. Phillips, Physical Review Letters **8**, 316 (1962).

[49] S. M. Tabatabaei, D. Sánchez, A. L. Yeyati, and R. Sánchez, Physical Review Letters **125**, 247701 (2020).

[50] H. Nakano and H. Takayanagi, Physical Review B **50**, 3139 (1994).

[51] L. Fu, C. L. Kane, and E. J. Mele, Physical Review Letters **98**, 106803 (2007).

[52] Y. V. Nazarov and Y. M. Blanter, *Quantum transport: introduction to nanoscience* (Cambridge University Press, 2009).

[53] A. A. Burkov and L. Balents, Physical Review Letters **107**, 127205 (2011).

[54] H. Weng, C. Fang, Z. Fang, B. A. Bernevig, and X. Dai, Physical Review X **5**, 011029 (2015).

[55] Z. Wang, D. Gresch, A. A. Soluyanov, W. Xie, S. Kushwaha, X. Dai, M. Troyer, R. J. Cava, and B. A. Bernevig, Physical Review Letters **117**, 056805 (2016).

[56] L. Fu and C. L. Kane, Physical Review B **79**, 161408 (2009).

[57] R. Jackiw and P. Rossi, Nuclear Physics B **190**, 681 (1981).

[58] S. Uchida, T. Habe, and Y. Asano, Journal of the Physical Society of Japan **83**, 064711 (2014).

[59] R. J. Soulen, J. M. Byers, M. S. Osofsky, B. Nadgorny, T. Ambrose, S. F. Cheng, P. R. Broussard, C. T. Tanaka, J. Nowak, J. S. Moodera, A. Barry, and J. M. D. Coey, Science **282**, 85 (1998).

[60] C. Timm, "Theory of superconductivity", Feb. 3, 2021.

[61] S. Chakravarty, R. B. Laughlin, D. K. Morr, and C. Nayak, Physical Review B **63**, 094503 (2001).

[62] H. Zhang, C.-X. Liu, X.-L. Qi, X. Dai, Z. Fang, and S.-C. Zhang, Nature Physics **5**, 438 (2009).

[63] M. R. Zirnbauer, Journal of Mathematical Physics **37**, 4986 (1996).

[64] A. Altland and M. R. Zirnbauer, Physical Review B **55**, 1142 (1997).

[65] S. Ryu, A. P. Schnyder, A. Furusaki, and A. W. W. Ludwig, New Journal of Physics **12**, 065010 (2010).

[66] S.-Q. Shen, *Topological insulators* (Springer Berlin Heidelberg, 2012), 216 pp.

[67] L. Fu and E. Berg, Physical Review Letters **105**, 097001 (2010).

[68] A. P. Schnyder, P. M. R. Brydon, D. Manske, and C. Timm, Physical Review B **82**, 184508 (2010).

[69] A. A. Vargas-Paredes, A. A. Shanenko, A. Vagov, M. V. Milošević, and A. Perali, Physical Review B **101**, 094516 (2020).

[70] J. Cano, B. Bradlyn, Z. Wang, M. Hirschberger, N. P. Ong, and B. A. Bernevig, Physical Review B **95**, 161306 (2017).

[71] Y. Ominato, S. Tatsumi, and K. Nomura, Physical Review B **99**, 085205 (2019).

[72] J. D. Sau, R. M. Lutchyn, S. Tewari, and S. Das Sarma, Physical Review Letters **104**, 040502 (2010).

[73] T. Meng and L. Balents, Physical Review B **86**, 054504 (2012).

[74] J. Bardeen, R. Kümmel, A. E. Jacobs, and L. Tewordt, Physical Review **187**, 556 (1969).

[75] C. W. J. Beenakker, Physical Review Letters **67**, 3836 (1991).

[76] T. Zhang, P. Cheng, W.-J. Li, Y.-J. Sun, G. Wang, X.-G. Zhu, K. He, L. Wang, X. Ma, X. Chen, Y. Wang, Y. Liu, H.-Q. Lin, J.-F. Jia, and Q.-K. Xue, Nature Physics **6**, 104 (2010).

[77] J. D. Sau, S. Tewari, R. M. Lutchyn, T. D. Stanescu, and S. Das Sarma, Physical Review B **82**, 214509 (2010).

[78] N. F. Q. Yuan and L. Fu, Physical Review B **97**, 115139 (2018).

[79] R. Nakai and K. Nomura, Physical Review B **101**, 094510 (2020).